

## EVOLUTION OF THE STELLAR MASS-METALLICITY RELATION SINCE $z = 0.75$

JOHN MOUSTAKAS<sup>1</sup>, DENNIS ZARITSKY<sup>2</sup>, MICHAEL BROWN<sup>3</sup>, RICHARD J. COOL<sup>4,5</sup>, ARJUN DEY<sup>6</sup>, DANIEL J. EISENSTEIN<sup>7</sup>,  
ANTHONY H. GONZALEZ<sup>8</sup>, BUELL JANNUZI<sup>6</sup>, CHRISTINE JONES<sup>7</sup>, CHRIS S. KOCHANEK<sup>9</sup>,  
STEPHEN S. MURRAY<sup>7,10</sup>, AND VIVIENNE WILD<sup>11</sup>

SUBMITTED TO APJ

### ABSTRACT

We measure the gas-phase oxygen abundances of  $\sim 3000$  star-forming galaxies at  $z = 0.05 - 0.75$  using optical spectrophotometry from the AGN and Galaxy Evolution Survey (AGES), a spectroscopic survey of  $I_{AB} < 20.45$  galaxies over  $7.9 \text{ deg}^2$  in the NOAO Deep Wide Field Survey (NDWFS) Boötes field. We use state-of-the-art techniques to measure the nebular emission lines and stellar masses, and explore and quantify several potential sources of systematic error, including the choice of metallicity diagnostic, aperture bias, and contamination from unidentified active galactic nuclei (AGN). Combining volume-limited AGES samples in six independent redshift bins and  $\sim 75,000$  star-forming galaxies with  $r_{AB} < 17.6$  at  $z = 0.05 - 0.2$  selected from the Sloan Digital Sky Survey (SDSS) that we analyze in the identical manner, we measure the evolution of the stellar mass-metallicity ( $\mathcal{M} - Z$ ) between  $z = 0.05$  and  $z = 0.75$ . We find that at fixed stellar mass galaxies at  $z \sim 0.7$  have just 30%–60% the metal content of galaxies at the present epoch, where the uncertainty is dominated by the strong-line method used to measure the metallicity. Moreover, we find no statistically significant evidence that the  $\mathcal{M} - Z$  relation evolves in a mass-dependent way for  $\mathcal{M} \simeq 10^{9.8} - 10^{11} \mathcal{M}_{\odot}$  star-forming galaxies. Thus, for this range of redshifts and stellar masses the  $\mathcal{M} - Z$  relation simply shifts toward lower metallicity with increasing redshift without changing its shape.

*Subject headings:* galaxies: abundances — galaxies: evolution — galaxies: fundamental parameters

### 1. INTRODUCTION

Like stellar mass, the gas-phase metallicity of a galaxy is a sensitive observational diagnostic of its past star formation history and present-day evolutionary state for the simple reason that in a closed system metallicity increases monotonically with each successive generation of massive stars.<sup>12</sup> In detail, however, galaxies are not closed systems: infall of cold, metal-poor gas from the intergalactic medium, rapid gas accretion via minor and

major mergers, and supernova-driven winds of gas and metals can modulate the metallicity of individual galaxies according to their large-scale environment, gas supply, and assembly history. Therefore, accurate abundance measurements provide valuable insight into the interplay between many fundamental processes in galaxy evolution, including star formation, gas accretion, and supernova-driven feedback across cosmic time (Tinsley 1980; Pagel 1997; Pettini 2004).

Nebular emission lines—ubiquitous in the rest-frame optical spectra of star-forming galaxies—provide a particularly powerful way to study the chemical abundances of both nearby and distant galaxies. Among the most commonly observed lines are the Balmer  $H\alpha$   $\lambda 6563$ ,  $H\beta$   $\lambda 4861$ , and  $H\gamma$   $\lambda 4340$  hydrogen recombination lines, and the collisionally excited [O II]  $\lambda\lambda 3726, 3729$ , [Ne III]  $\lambda 3869$ , [O III]  $\lambda\lambda 4959, 5007$ , [N II]  $\lambda\lambda 6548, 6584$ , and [S II]  $\lambda\lambda 6716, 6731$  forbidden lines. Because these lines originate principally in star-forming (H II) regions, they trace the physical conditions in the gas from which the current generation of massive stars is forming. The metal lines in particular are the principal coolants in H II regions, making them sensitive to the total abundance of oxygen and other heavy elements in the interstellar medium. Moreover, the relative line-strengths can be used to infer the interstellar pressure, density, temperature, ionizing radiation field strength, dust reddening, and the presence of an active galactic nucleus (AGN). Finally, from an observational standpoint, many of the nebular lines are intrinsically strong, making them measurable in even relatively low signal-to-noise spectra over a broad range of redshifts.

Following the discovery of the correlation between dynamical mass and oxygen abundance in dwarf irregular

<sup>1</sup> Center for Astrophysics and Space Sciences, University of California, San Diego, 9500 Gilman Drive, La Jolla, California, 92093, USA; jmoustakas@ucsd.com

<sup>2</sup> Steward Observatory, University of Arizona, 933 North Cherry Avenue, Tucson, AZ 85721, USA

<sup>3</sup> School of Physics, Monash University, Clayton, Victoria 3800, Australia

<sup>4</sup> Carnegie-Princeton Fellow; The Observatories of the Carnegie Institution of Washington, 813 Santa Barbara Street, Pasadena, CA 91101, USA

<sup>5</sup> Department of Astrophysical Sciences, Princeton University, Peyton Hall, Princeton, NJ 08544

<sup>6</sup> National Optical Astronomy Observatory, 950 North Cherry Avenue, Tucson, AZ 85719, USA

<sup>7</sup> Harvard-Smithsonian Center for Astrophysics, 60 Garden Street, Cambridge MA 02138, USA

<sup>8</sup> Department of Astronomy, Bryant Space Science Center, University of Florida, Gainesville, FL 32611, USA

<sup>9</sup> Department of Astronomy, The Ohio State University, 140 West 18th Avenue, Columbus, OH 43210, USA

<sup>10</sup> Department of Physics and Astronomy, Johns Hopkins University, Baltimore, MD 21218, USA

<sup>11</sup> Institute for Astronomy, University of Edinburgh, Royal Observatory, Blackford Hill, Edinburgh EH9 3HJ, UK

<sup>12</sup> Throughout this paper we use the terms *metallicity* and *abundance* interchangeably to mean the heavy-element content of the warm ( $T \approx 10^4$  K) interstellar medium of galaxies. In particular, we make the reasonable assumption that the nebular oxygen abundance, historically written as  $12 + \log(O/H)$ , traces the total gas-phase metallicity,  $Z_{\text{gas}}$ .

galaxies (Lequeux et al. 1979; see also Garnett & Shields 1987; Oey & Kennicutt 1993), numerous subsequent studies demonstrated that star-forming galaxies ranging from the lowest-luminosity dwarfs to massive disk galaxies obey a well-defined luminosity-metallicity ( $L - Z$ ) correlation spanning several orders of magnitude in  $B$ -band luminosity (Garnett & Shields 1987; Skillman et al. 1989; Zaritsky et al. 1994; Pilyugin et al. 2004; Lamareille et al. 2004; Salzer et al. 2005; Lee et al. 2006; Moustakas et al. 2010). Metallicity was also found to correlate with morphological type (Edmunds & Pagel 1984), surface mass density (McCall 1982; Ryder 1995; Garnett et al. 1997), and maximum rotational velocity (Zaritsky et al. 1994; Garnett 2002; Dalcanton 2007). However, because these global properties all correlate with one another, the underlying physical driver of the  $L - Z$  relation remained elusive.

Tremonti et al. (2004) was the first to leverage the tremendous statistical power of the Sloan Digital Sky Survey (SDSS; York et al. 2000) spectroscopic database to show that the gas-phase metallicity of a galaxy correlates best with stellar mass,  $\mathcal{M}$ , now known as the stellar mass-metallicity ( $\mathcal{M} - Z$ ) relation. The  $\mathcal{M} - Z$  relation reveals that the gas-phase metallicity of star-forming galaxies increases monotonically with stellar mass and then remains relatively constant above  $\mathcal{M} \approx 3 \times 10^{10} M_{\odot}$ . Although subsequent studies have found weak residual correlations from the  $\mathcal{M} - Z$  relation with stellar mass density (Tremonti et al. 2004; Liang et al. 2010), size (Ellison et al. 2008a), large- and small-scale environment (Mouhcine et al. 2007; Cooper et al. 2008; Ellison et al. 2008b, 2009; Peeples et al. 2009), star formation rate (SFR; Mannucci et al. 2010; Lara-López et al. 2010b; Yates et al. 2011; Cresci et al. 2011), and the existence of bars (Ellison et al. 2011), the intrinsic dispersion in the  $\mathcal{M} - Z$  relation is  $\lesssim 0.1$  dex, making it among the tightest empirical correlations known.

The physical origin of the  $\mathcal{M} - Z$  relation remains under debate. One possibility is that low-mass galaxies started forming stars later than massive galaxies (i.e., they are “younger”; Noeske et al. 2007a; Leitner 2011) and have been less efficient at synthesizing metals via star formation (Brooks et al. 2007; Mouhcine et al. 2008; Calura et al. 2009). This interpretation is qualitatively consistent with the measured low gas fractions in massive galaxies relative to lower-mass galaxies (McGaugh & de Blok 1997; Geha et al. 2006; Garcia-Appadoo et al. 2009), and with the observed correlation between stellar mass and SFR (the *star formation sequence*; Brinchmann et al. 2004; Salim et al. 2007; Elbaz et al. 2007; Noeske et al. 2007b). Another popular interpretation is that supernova-driven galactic winds preferentially expel metals from low-mass galaxies (Larson 1974; Garnett 2002; Tremonti et al. 2004; Dalcanton 2007). Indeed, state-of-the-art hydrodynamic and semianalytic theoretical models *require* metal-enriched outflows to match many observed galaxy properties, including the  $\mathcal{M} - Z$  relation (Kobayashi et al. 2007; Finlator & Davé 2008; Dutton & van den Bosch 2009; Peeples & Shankar 2011; Davé et al. 2011b). A related outstanding question is whether gas and metals ejected in previous star formation episodes are re-accreted onto galaxies (De Lucia et al. 2004;

Oppenheimer et al. 2010), or whether galaxies are predominantly fed by infall of cold, metal-poor gas from the intergalactic medium (Köppen & Edmunds 1999; Faucher-Giguère et al. 2011). Alternatively, Köppen et al. (2007) show that a SFR-dependent, and therefore mass-dependent, stellar initial mass function (IMF) naturally explains the observed  $\mathcal{M} - Z$  relation without needing to invoke metal-enriched outflows from galaxies.

One way of gaining insight into the complex and multifaceted interrelationship between chemical abundance measurements, star formation, gas accretion, and the role of supernova feedback during galaxy growth is to measure the evolution of the  $\mathcal{M} - Z$  relation. The time since  $z = 1$ , spanning  $\sim 60\%$  of the age of the Universe, is important for many reasons. Measurements of the star formation sequence (Noeske et al. 2007b; Wuyts et al. 2011) suggest that star-forming galaxies over this redshift range evolve smoothly as a population, driven by continuous, secular processes like gas consumption and *in situ* star formation (Bell et al. 2005; Noeske 2009; Leitner 2011). Bolstered by measurements of their morphological distribution (Bell et al. 2005; Konishi et al. 2011) and clustering properties (Coil et al. 2008; Zehavi et al. 2011), these results suggest that we can draw direct evolutionary connections linking star-forming galaxies across this redshift range. In addition, the metallicity-sensitive  $R_{23}$  parameter (defined in §5) can be measured from ground-based optical spectroscopy of galaxies at least to  $z \sim 0.8$ , ensuring that metallicities can be derived using a single consistent abundance calibration.

Unfortunately, previous studies have reported widely varying results on the evolution of both the shape and normalization of the  $\mathcal{M} - Z$  relation since  $z = 1$ . Savaglio et al. (2005) and Zahid et al. (2011) find that the mean metallicity of galaxies at  $z \sim 0.8$  with  $\mathcal{M} \sim 10^{10.3} M_{\odot}$  differs by just  $\sim 0.05$  dex (factor of  $\sim 1.12$ ) relative to similarly massive star-forming galaxies at  $z \sim 0.1$ , whereas they find that galaxies with  $\mathcal{M} \sim 10^{9.5} M_{\odot}$  undergo a factor of 2 – 3 more chemical evolution over the same redshift interval. On the other hand, Liang et al. (2006a) and Cowie & Barger (2008) report 0.2 – 0.3 dex (factor of 1.6 – 2) of chemical evolution for galaxies with  $\mathcal{M} \sim 10^{10.3} M_{\odot}$  since  $z \sim 0.7$  and no statistically significant evidence for evolution in the shape of the  $\mathcal{M} - Z$  relation (see also Rodrigues et al. 2008). Lamareille et al. (2009) and Pérez-Montero et al. (2009) find an even greater amount of metallicity evolution,  $\sim 0.35$  dex (factor of 2.2) since  $z = 0.6 - 1$ , and a *flattening* of the  $\mathcal{M} - Z$  relation at intermediate redshift. Other studies based on the evolution of the  $B$ -band  $L - Z$  relation report that at fixed luminosity star-forming galaxies at  $z = 0.5 - 1$  are 0.1 – 0.7 dex (factor of 1.25 – 5) more metal-poor than local star-forming galaxies (Kobulnicky & Zaritsky 1999; Carollo & Lilly 2001; Lilly et al. 2003; Kobulnicky & Phillips 2003; Kobulnicky & Kewley 2004; Maier et al. 2004, 2005, 2006; Lamareille et al. 2009). However, the significant amount of luminosity evolution experienced by blue, star-forming galaxies since  $z = 1$  (Blanton 2006; Faber et al. 2007; Cool et al. 2011) renders the interpretation of the  $L - Z$  relation less straightforward.

The origin of these widely varying results on the evo-

lution of the  $\mathcal{M} - Z$  relation can be attributed to various issues, including cosmic variance, small sample size, heterogenous selection criteria, systematic differences in the methods used to infer nebular abundances, an inconsistent analysis of the local  $\mathcal{M} - Z$  relation, spectroscopy with insufficient spectral coverage, signal-to-noise ( $S/N$ ) ratio, or instrumental resolution, and uncertain stellar mass estimates due to limited broadband photometric coverage. Consequently, the efficacy of existing observational metallicity constraints on state-of-the-art theoretical models of galaxy formation (De Lucia et al. 2004; Brooks et al. 2007; Dutton & van den Bosch 2009; Davé et al. 2011b) has been fairly limited. From an observational standpoint, there exists a clear need for a large, homogeneously selected sample of galaxies with high-quality spectroscopy and reliable stellar mass estimates to better constrain the evolution of the  $\mathcal{M} - Z$  relation at intermediate redshift.

To address this need, we measure the evolution of the  $\mathcal{M} - Z$  and  $B$ -band  $L - Z$  relations at intermediate redshift using oxygen abundances of  $\sim 3000$  star-forming galaxies at  $z = 0.05 - 0.75$  observed as part of the AGN and Galaxy Evolution Survey (AGES; Kochanek et al. 2011), and  $\sim 75,000$  galaxies at  $z = 0.05 - 0.2$  selected from the SDSS. The AGES main galaxy survey consists of optical spectrophotometry for  $\sim 12,000$  galaxies in the  $\sim 9 \text{ deg}^2$  NOAO Deep Wide Field Survey (NDWFS; Jannuzi & Dey 1999; Brown et al. 2003, 2007, 2008) Boötes field at a median redshift of  $z \sim 0.3$ . This sample is statistically complete over  $7.9 \text{ deg}^2$  for galaxies with  $I_{AB} < 20.45$  (Kochanek et al. 2011), reaching  $\sim 2 \text{ mag}$  deeper than the SDSS main galaxy sample (Strauss et al. 2002) over a considerably larger area than other recent or ongoing surveys of intermediate-redshift galaxies such as DEEP2 (Davis et al. 2003), AEGIS (Davis et al. 2007), VVDS (Le Fèvre et al. 2004, 2005; Garilli et al. 2008), and zCOSMOS (Lilly et al. 2009).<sup>13</sup> The statistical completeness, large sample size, and availability of high-quality optical spectroscopy and deep optical and near-infrared photometry enables us to investigate the evolution of both the  $\mathcal{M} - Z$  and optical  $L - Z$  relations of star-forming galaxies at  $z = 0.05 - 0.75$  using a single, self-consistent abundance diagnostic over the entire redshift range.

The plan of the paper is as follows. In §2 we present the ground-based optical and near-infrared imaging we use, summarize the AGES observations, and describe how we measure the nebular emission lines for the galaxies in our sample. In §3 we describe the methodology used to derive rest-frame luminosities, colors, and stellar masses, and in §4 we select a subset of the AGES galaxies for chemical abundance analysis. We present the methods we use to derive oxygen abundances in §5, and our principal results in §6, where we quantify the mass-dependent evolution of the  $\mathcal{M} - Z$  relation for star-forming galaxies since  $z = 0.75$ . In §7 we address the effect of various potential sources of systematic uncertainty on our results, and in §8 we discuss recent theoretical work on the origin and evolution of the  $\mathcal{M} - Z$  relation. Finally, we summarize

our principal conclusions in §9.

We adopt a concordance cosmology with  $\Omega_m = 0.3$ ,  $\Omega_\Lambda = 0.7$ , and  $h_{70} \equiv H_0/100 = 0.7$ , the AB magnitude system (Oke & Gunn 1983), and the Chabrier (2003) initial mass function (IMF) from  $0.1 - 100 M_\odot$  unless otherwise indicated. For reference, the conversion from Vega to AB for the  $I$ -band filter used to select AGES targets is  $+0.45 \text{ mag}$ , that is  $I_{AB} = I_{Vega} + 0.45$ .

## 2. OBSERVATIONS

In the following sections we present the multiwavelength imaging of the Boötes field that we use (§2.1), describe the AGES optical spectroscopy and emission-line measurements (§2.2), and construct a comparison sample of local galaxies from the SDSS (§2.3).

### 2.1. Multiwavelength Photometry

#### 2.1.1. Optical and Near-infrared Imaging

Our baseline optical observations consist of deep  $B_WRI$  imaging available as part of the NDWFS third public data release.<sup>14</sup> The imaging was carried out using the MOSAIC-I camera at the KPNO/Mayall 4 m telescope, reaching a  $5\sigma$  depth of  $\sim 26.5$ ,  $\sim 25.5$ , and  $\sim 25.3 \text{ mag}$  in a  $2''$  diameter circular aperture in  $B_W$ ,  $R$ , and  $I$ , respectively. Note that although  $K$ -band imaging from the NDWFS is also available for  $\sim 60\%$  of the Boötes survey region, we do not use these older data in favor of the more recent near-infrared (near-IR) observations described below.

We supplement the NDWFS photometry with  $U$ - and  $z$ -band observations obtained as part of two other imaging campaigns. F. Bian et al. (2012, in prep.) have obtained deep  $U$ -band imaging of the Boötes field using the Large Binocular Camera (LBC; Giallongo et al. 2008) mounted at the primary focus of the 8.4 m Large Binocular Telescope (LBT); these observations reach a  $5\sigma$  depth of  $\sim 25.2 \text{ mag}$  for point sources. Second, the zBoötes<sup>15</sup> survey (Cool 2007) imaged  $7.62 \text{ deg}^2$  of the Boötes field to a  $3\sigma$  depth of  $22.4 \text{ mag}$  in a  $3''$  diameter aperture using the 90PRIME prime-focus wide-field imager mounted at the Bok 2.3 m telescope (Williams et al. 2004).

Finally, we utilize deep  $JHK_s$  near-IR imaging of the entire Boötes field obtained using the NOAO Extremely Wide-Field Infrared Mosaic (NEWFIRM; Autry et al. 2003) instrument at the KPNO/Mayall 4 m telescope. The NEWFIRM observations achieved a  $5\sigma$  depth of  $\sim 22.9$ ,  $\sim 22.1$ , and  $\sim 21.4 \text{ mag}$  in a  $3''$  diameter aperture in  $J$ ,  $H$ , and  $K_s$ , respectively. More details regarding the NEWFIRM observations and reductions will be described in an upcoming paper (A. Gonzalez, 2011, private communication).

#### 2.1.2. Ancillary X-ray, Mid-Infrared, and Radio Imaging

We use observations of the Boötes field in the X-ray from the *Chandra X-ray Observatory*, at  $3.6 - 8 \mu\text{m}$  from the *Spitzer Space Telescope* (Werner et al. 2004), and at  $1.4 \text{ GHz}$  from the Westerbork Synthesis Radio telescope

<sup>13</sup> For galaxies at  $z \lesssim 0.5$ , the Galaxy and Mass Assembly (GAMA) survey will ultimately supplant all these surveys by obtaining optical spectroscopy for several hundred thousand galaxies brighter than  $r_{AB} \approx 19.8$  over  $360 \text{ deg}^2$  (Driver et al. 2011).

<sup>14</sup> The  $B_W$  filter is a “wide” filter with a bluer effective wavelength ( $\lambda_{\text{eff}} \approx 4200 \text{ \AA}$ ) than the standard Johnson-Morgan  $B$ -band filter (Bessell 1990).

<sup>15</sup> <http://archive.noao.edu/nsa/zbootes.html>



to help identify and remove AGN from our sample (see §4.2). Here, we briefly describe these ancillary data.

The 5 ks X-ray observations were obtained with the *Chandra* Advanced CCD Imaging Spectrometer (ACIS) instrument as part of the XBoötes<sup>16</sup> survey (Murray et al. 2005b; Kenter et al. 2005). XBoötes covered  $\sim 8.5$  deg<sup>2</sup> of the Boötes field to an on-axis limiting flux of  $\sim 7.8 \times 10^{-15}$  erg s<sup>-1</sup> cm<sup>-2</sup> Å<sup>-1</sup> in the 0.5 – 7 keV band. We use the publically available catalog of 3213 X-ray point-sources with four or more X-ray counts matched to the NDWFS optical catalog by Brand et al. (2006) using a Bayesian matching algorithm.

In the infrared, the *Spitzer* Deep Wide-Field Survey (SDWFS; Ashby et al. 2009) obtained deep, multi-epoch mid-IR imaging of the Boötes field with the *Spitzer* Infrared Array Camera (IRAC; Fazio et al. 2004). These observations reach aperture-corrected  $5\sigma$  depths of  $\sim 22.6$ ,  $\sim 22.1$ ,  $\sim 20.2$ , and  $\sim 20.2$  mag in a 4'' diameter aperture at 3.6, 4.5, 5.8, and 8  $\mu$ m, respectively. In our analysis we use the 3.6  $\mu$ m-detected, aperture-corrected 4'' diameter 3.6 – 8  $\mu$ m aperture magnitudes available at the NASA/IPAC Infrared Science Archive<sup>17</sup>, as described by Ashby et al. (2009).

Finally, radio observations from the WSRT 1.4 GHz radio survey covered  $\sim 7$  deg<sup>2</sup> of the Boötes field to a  $5\sigma$  limiting flux of 140  $\mu$ Jy (de Vries et al. 2002). When matching to the AGES catalog we use a 3'' diameter search radius (Hickox et al. 2009).

## 2.2. AGES Optical Spectroscopy

The AGES main galaxy survey targeted galaxies brighter than  $I_{AB} = 20.45$  and covered 7.9 deg<sup>2</sup> of the NDWFS Boötes field, making it among the largest wide-area spectroscopic surveys of intermediate-redshift galaxies conducted to date. We briefly summarize the AGES observations in §2.2.1, and in §2.2.2 we describe the procedure used to measure the nebular emission-line strengths from these data. A more thorough description of the AGES experimental design, observations, and redshift measurements can be found in Kochanek et al. (2011) and Cool et al. (2011).

### 2.2.1. Observations, Reductions, and Spectroscopic Completeness

The MMT/Hectospec multi-fiber optical spectrograph is fed by 300 robotically controlled 1''5 diameter fibers, enabling efficient data acquisition over a 1° diameter field-of-view (Roll et al. 1998; Fabricant et al. 1998, 2005). The 270 line mm<sup>-1</sup> grating used by AGES provides 3700 – 9200 Å spectra with 1.2 Å pixels at  $\sim 6$  Å FWHM resolution. An atmospheric dispersion corrector (ADC) built into the MMT f/5 wide-field lens eliminates wavelength-dependent light-loss due to atmospheric refraction, while relative spectrophotometric calibration is facilitated by observing F sub-dwarf standard stars selected from the SDSS (Abazajian et al. 2004; Fabricant et al. 2008).

We reduce the AGES spectra using standard procedures implemented in HSRED<sup>18</sup>, a customized Hec-

tospec data reduction package based on the SDSS spectroscopic data reduction pipeline.<sup>19</sup> Briefly, we bias- and overscan-subtract the data, and then extract, wavelength-calibrate, flat-field, and sky-subtract each galaxy spectrum. We combine multiple exposures using inverse variance weights, and robustly reject cosmic rays (van Dokkum 2001). We then flux-calibrate each spectrum, divide by a suitably scaled telluric absorption spectrum, and correct for foreground Galactic reddening ( $R_V \equiv A_V/E(B - V) = 3.1$ ; O'Donnell 1994; Schlegel et al. 1998). Note that five of the Hectospec configurations<sup>20</sup> obtained in 2004 could not be flux-calibrated, and have been excluded from the present analysis. Finally, we determine redshifts using two independent codes and cross-validate the results by visual inspection (see Kochanek et al. 2011 for details).

Because we are interested in faint emission lines at intermediate redshift, accurate sky subtraction is crucial. Therefore we implemented an automated principal component analysis technique originally developed for the SDSS to suppress the amplitude of the sky-subtraction residuals redward of  $\sim 6700$  Å, which are dominated by a “forest” of atmospheric OH sky lines (Wild & Hewett 2005). Briefly, the method reconstructs a model of the night-sky spectrum for each configuration of the Hectospec fibers by exploiting the fact that the OH sky lines are highly correlated both in wavelength and between all the fibers. On average, we obtain a factor of two improvement in the S/N ratio of affected pixels.

The AGES spectra suffer from two additional data-reduction issues that do not affect the redshift measurements, but which are relevant to our emission-line analysis. First, the ADC was operated incorrectly during some of the observations that took place in 2004, leading to systematic errors in the spectrophotometry blueward of  $\sim 5000$  Å for these early observations (Fabricant et al. 2008). And second, the spectra are occasionally contaminated by the featureless continuum of one or both of the light-emitting diodes (LEDs) located on the Hectospec fiber-positioners. In most cases this extra light appears as a rapidly rising continuum redward of 8500 Å, although it can also bias the average sky spectrum, resulting in an oversubtraction of the sky flux in the 8500 – 9200 Å wavelength range. We address these issues in §2.2.2.

We conclude this section with a brief discussion of the AGES spectroscopic completeness (for details see Kochanek et al. 2011 and Cool et al. 2011). AGES covered 7.9 deg<sup>2</sup> of the Boötes field with 15 slightly overlapping pointings, each with three configurations. Within each field, AGES targeted 100% of galaxies with  $I_{AB} < 18.95$  and employed a variety of sparse-sampling criteria to observe a subset of galaxies with  $18.95 < I_{AB} < 20.45$  that were also bright at other wavelengths. Because these sampling fractions are known exactly, it is easy to recover a sample that is statistically complete to  $I_{AB} < 20.45$  by simply weighting by the inverse of the sampling rate. The other sources of incompleteness in AGES are relatively small. Approximately 5% of objects in the parent

<sup>16</sup> <http://www.noao.edu/noao/noadeep/XBootesPublic>

<sup>17</sup> <http://irsa.ipac.caltech.edu/data/SPITZER/SDWFS>

<sup>18</sup> [http://www.astro.princeton.edu/~sim\\$rcool/hsred](http://www.astro.princeton.edu/~sim$rcool/hsred)

<sup>19</sup> <http://spectro.princeton.edu>

<sup>20</sup> A configuration refers to a given geometrical layout of the 300 Hectospec fibers.

sample failed to be assigned a spectroscopic fiber (*fiber incompleteness*). Among the objects that were observed, AGES failed to measure a redshift for  $\sim 2\%$  (*redshift incompleteness*), which is a weak function of surface brightness. Finally, we estimate that roughly 4% of objects are missing from the targeting catalog (*photometric incompleteness*) due to proximity to a bright star or problems with the photometry itself. To correct for these effects, we weight every object in AGES by the product of these terms, resulting in a sample that is statistically complete to  $I_{AB} = 20.45$ .

### 2.2.2. Emission-line Measurements

High-resolution population synthesis models have become an indispensable tool for investigating the integrated optical spectra of galaxies (Bruzual & Charlot 2003; Vázquez & Leitherer 2005; Grillo et al. 2009; Conroy et al. 2009; Percival et al. 2009; Vazdekis et al. 2010). By modeling and subtracting the stellar continuum from the observed spectrum, these models have made it possible to study the optical emission lines free from the systematic effects of Balmer and metal-line absorption (e.g., Panter et al. 2003; Tremonti et al. 2004; Cid Fernandes et al. 2005; Moustakas & Kennicutt 2006; Sarzi et al. 2006; Ocvirk et al. 2006; Tojeiro et al. 2007; Oh et al. 2011). Neglecting the effects of stellar absorption, particularly under the Balmer emission lines, can lead to severe biases in the nebular abundances, SFRs, and dust reddenings inferred from the optical emission lines (e.g., Kennicutt 1992; Kobulnicky et al. 1999; Rosa-González et al. 2002; Moustakas et al. 2006, 2010; Asari et al. 2007).

Our basic strategy is to model the observed spectrum of each galaxy as a non-negative linear combination of simple (i.e., instantaneous-burst) population synthesis models of varying ages, making some simplifying assumptions regarding the stellar metallicity of the galaxy and the effects of dust attenuation. We then subtract the best-fitting continuum model from the data, and fit the residual emission-line spectrum assuming Gaussian line-profiles. We emphasize that our principal goal is to obtain an emission-line spectrum that has been corrected self-consistently for stellar absorption, not to constrain the star formation and chemical evolution history of the galaxy from its integrated stellar spectrum. The multi-dimensional parameter space of star formation history, age, metallicity, and dust attenuation is highly degenerate (i.e., there are many local minima), and our simple approach is ill-suited for finding the global solution (but see Walcher et al. 2010, and references therein, for more advanced techniques that tackle this issue). Fortunately, the emission-line strengths we measure do not depend sensitively on the simplifying assumptions underlying our technique.

We construct our template set using the Bruzual & Charlot (2003, hereafter BC03) population synthesis models, based on the Padova 1994 stellar evolutionary tracks (Girardi et al. 1996, and references therein) and the empirical STELIB stellar library (Le Borgne et al. 2003). We choose 10 instantaneous-burst, solar-metallicity ( $Z = 0.02$ ) models with ages spaced quasi-logarithmically in time between 5 Myr and 13 Gyr, assuming the Chabrier (2003) initial mass function (IMF) from  $0.1 - 100 \mathcal{M}_{\odot}$ . We treat dust reddening

as a free parameter, and adopt the Calzetti et al. (2000) dust attenuation law. Finally, we find the best-fitting, non-negative linear combination of the templates using a modified version of the pPXF<sup>21</sup> continuum-fitting code (Cappellari & Emsellem 2004; Moustakas et al. 2010).

We verified that adopting different model parameters does not have a significant effect on the derived emission-line strengths. Specifically, we experimented with a wider range of stellar metallicities, varied the number of templates (i.e., instantaneous-burst ages), tried several different extinction curves, and assumed a different initial mass function. These results indicate that it is not necessary to find the *global* solution to the continuum fitting problem in order to be able to study the emission-line properties of galaxies free from the systematic effects of stellar absorption.

We fit the observed stellar continuum of each galaxy iteratively. First, we isolate the rest-frame  $\sim 3600 - 4400 \text{ \AA}$  spectral range to derive a more precise measurement of the absorption-line redshift,  $z_{\text{abs}}$ , and to obtain an estimate of the stellar velocity dispersion,  $\sigma_{\text{disp}}$ , accounting for the instrumental resolution of our spectra ( $\sim 6 \text{ \AA}$  FWHM) and the resolution of the BC03 models ( $\sim 3 \text{ \AA}$  FWHM; BC03). Next, we fix  $z_{\text{abs}}$  and  $\sigma_{\text{disp}}$  at the derived values and model the full wavelength range, aggressively masking pixels that might be affected by emission lines, sky-subtraction residuals, telluric absorption, or the red leak (see §2.2.1). For approximately one-quarter of the observed Hectospec configurations (largely from 2004; see §2.2.1) there are non-negligible errors in the spectrophotometry shortward of  $\lambda_{\text{obs}} \sim 5000 \text{ \AA}$ . Therefore, for these configurations, we refit the spectra, masking out the affected blue observed-frame wavelengths, and then divide the observed spectrum by its best-fitting model, in effect constructing a sensitivity function correction for each galaxy. We then compute the median sensitivity function correction using all the spectra on a given configuration, and divide all the spectra by the median correction. Finally, we refit those galaxy spectra one last time, this time using the full wavelength range. We assess the effect of this correction on our abundance analysis below.

The last step before fitting the emission lines is to subtract the red leak and any remaining low-level residuals due to imperfect sky-subtraction, template mismatch, or imperfect flux-calibration. Given the best-fitting continuum model for each galaxy, we subtract it from the data and remove these residual differences (typically of order a few percent) using a sliding 151-pixel median filter. Finally, we subtract this median residual spectrum from the original data, and then refit and subtract the stellar continuum one last time, leaving a pure emission-line spectrum.

Following Moustakas et al. (2010), we fit the emission-line spectrum of each galaxy iteratively using a modified version of the GANDALF<sup>22</sup> emission-line fitting code, assuming Gaussian line-profiles (Sarzi et al. 2006; Schawinski et al. 2007; Oh et al. 2011). Specifically, we fit the [Ne v]  $\lambda 3426$ , [O II]  $\lambda 3727$ , [Ne III]  $\lambda 3869$ , [O III]  $\lambda \lambda 4959, 5007$ , [N II]  $\lambda \lambda 6548, 6584$ ,

<sup>21</sup> [http://www-astro.physics.ox.ac.uk/~sim\\$mc/id1](http://www-astro.physics.ox.ac.uk/~sim$mc/id1)

<sup>22</sup> <http://www.strw.leidenuniv.nl/sauron>

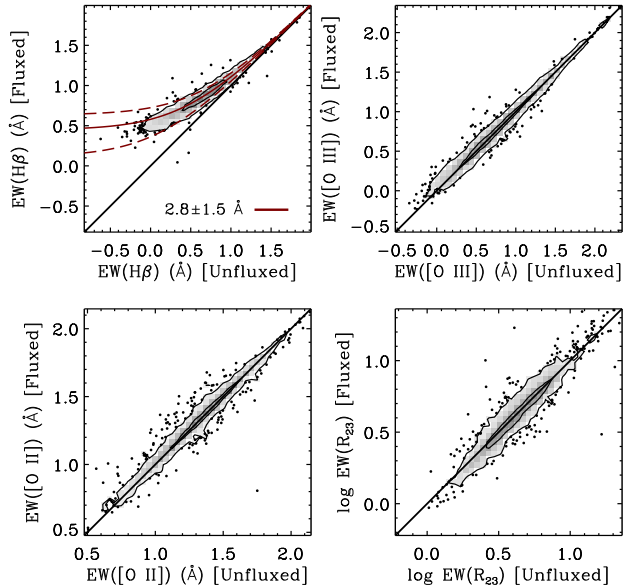


FIG. 1.— Comparison of EWs measured from the fluxed and unfluxed AGES spectra for  $H\beta$ ,  $[O\ III]\ \lambda 5007$ , and  $[O\ II]\ \lambda 3727$ . In each panel the solid line shows the one-to-one relation, and the contours enclose 50% and 95% of the points. We find excellent statistical agreement among the two emission-line measurements, assuming that  $EW(H\beta)$  measured from our unfluxed spectra is subject to  $2.8 \pm 1.5\ \text{\AA}$  of stellar absorption (solid and dashed red lines in the upper-left panel). In the lower-right panel we compare the metallicity-sensitive  $EW(R_{23}) \equiv (EW([O\ II]) + EW([O\ III]))/EW(H\beta)$  parameters measured from the fluxed and unfluxed spectra, after statistically correcting  $EW(H\beta)$  measured from the unfluxed spectra for an average  $2.8\ \text{\AA}$  of stellar absorption. These comparisons indicate that in spite of the spectrophotometric errors in AGES, our oxygen abundance estimates are not adversely affected.

and  $[S\ II]\ \lambda\lambda 6716, 6731$  forbidden lines, and the first five lines in the Balmer series:  $H\alpha\ \lambda 6563$ ,  $H\beta\ \lambda 4861$ ,  $H\gamma\ \lambda 4340$ ,  $H\delta\ \lambda 4101$ , and  $H5\ \lambda 3889$ . On the first iteration we tie the redshifts and intrinsic velocity widths (accounting for the instrumental resolution) of all the lines together to aid in the detection and deblending of weak lines. In addition, to reduce the number of free parameters, we constrain the  $[O\ III]\ \lambda 5007/[O\ III]\ \lambda 4959$  and  $[N\ II]\ \lambda 6584/[N\ II]\ \lambda 6548$  doublet ratios to be 3:1 (Osterbrock & Ferland 2006). On the second iteration we relax most of these constraints and use the best-fitting parameters from the first iteration as initial guesses. This second step is necessary because of our imperfect knowledge of the wavelength-dependent instrumental resolution, and to account for the fact that  $[O\ II]\ \lambda 3727$  is a doublet which is better represented at the spectral resolution of our data as a single, slightly broader Gaussian line than two closely-spaced Gaussian line-profiles. Note that even on the second iteration, however, we (separately) constrain the redshifts and velocity widths of the  $[O\ III]$ ,  $[N\ II]$ , and  $[S\ II]$  doublets to have the same values.

We evaluate the significance of each emission line by comparing the amplitude of the best-fitting Gaussian model,  $A_l$ , against the standard deviation of the residual (continuum-subtracted) spectrum,  $\sigma_c$ , around the line; we define a significant line as having  $A_l > 3\sigma_c$ . For each undetected emission line we estimate the  $1\sigma$  upper limit

on the total line-flux assuming a Gaussian line-profile using

$$F = \sqrt{2\pi} \sigma_c \delta_v, \quad (1)$$

where  $\delta_v$  is the mean velocity width of all the detected emission lines. Finally, we estimate the equivalent width (EW) of each emission line by dividing the integrated flux of the Gaussian model by the mean flux of the stellar continuum immediately blueward and redward of the given line.

We conclude this section by evaluating the effect of spectrophotometric errors on our line-measurements by measuring the  $[O\ II]$ ,  $H\beta$ , and  $[O\ III]\ \lambda 5007$  emission-line EWs from the *unfluxed* AGES spectra. For these spectra we model the stellar continuum as a low-order B-spline with iterative outlier rejection, subtract it from the data, and measure the EW of each emission line as described above. In Figure 1 we compare the  $[O\ II]$ ,  $H\beta$ , and  $[O\ III]$  emission-line EWs measured from the fluxed and unfluxed spectra, as well as the metallicity-sensitive  $EW(R_{23}) \equiv (EW([O\ II]) + EW([O\ III]))/EW(H\beta)$  parameter (see §5.2). We render the data in greyscale with the contours enclosing 50% and 95% of the points, and plot the one-to-one relation as a solid line. Overall we find good statistical agreement among the EWs measured from the two sets of spectra, although  $H\beta$  is clearly affected by stellar absorption. However, applying a mean  $2.8 \pm 1.5\ \text{\AA}$  correction to the  $EW(H\beta)$  values measured from the unfluxed spectra, shown as solid and dashed red lines in the upper-left panel of Figure 1, would bring the two EW measurements into good agreement. Meanwhile, the statistical agreement for  $EW([O\ II])$  and  $EW([O\ III])$  is excellent. In the lower-right panel we compare the two  $EW(R_{23})$  estimates after correcting  $EW(H\beta)$  measured from the unfluxed spectra for an average  $2.8\ \text{\AA}$  of stellar absorption. These comparisons indicate that our oxygen abundance estimates are not adversely affected by the spectrophotometric errors in AGES.

### 2.3. SDSS Comparison Sample

At low redshift ( $z \sim 0.1$ ) AGES is significantly affected by variations in large-scale structure (i.e., cosmic variance) because of the relatively small cosmological volume probed. Therefore, we use observations obtained as part of the SDSS as a local benchmark for studying the chemical abundance properties of the more distant galaxies observed by AGES.

The SDSS has obtained *ugriz* broadband photometry and high-precision optical (3800 – 9200 Å) spectrophotometry for roughly two million objects over nearly one-quarter of the sky (York et al. 2000; Stoughton et al. 2002).<sup>23</sup> We draw our SDSS comparison sample from the NYU Value-Added Galaxy Catalog<sup>24</sup> (NYU-VAGC; Blanton et al. 2005) corresponding to the SDSS Data Release 7 (DR7; Adelman-McCarthy et al. 2008). From this database we select 427,504 galaxies over  $6955\ \text{deg}^2$  that satisfy the main sample criteria defined by Strauss et al. (2002), and have Galactic extinction corrected (Schlegel et al. 1998) Petrosian magnitudes  $14.5 < r < 17.6$ , and redshifts  $0.05 < z < 0.2$ . We

<sup>23</sup> <http://www.sdss.org>

<sup>24</sup> <http://sdss.physics.nyu.edu/vagc>



choose the lower redshift limit to ensure that [O II]  $\lambda 3727$  lies within the SDSS spectral range (Stoughton et al. 2002), while the upper redshift limit rejects  $< 2\%$  of galaxies in the SDSS main sample. From the VAGC we retrieve for each object the spectroscopic redshift, the Galactic extinction-corrected *ugriz* Petrosian and *cmodel* (i.e., total; see Abazajian et al. 2004) magnitudes, integrated *JHK<sub>s</sub>* photometry (available for  $\sim 55\%$  of the sample) from the Two Micron All Sky Survey Extended Source Catalog (2MASS/XSC; Jarrett et al. 2000; Skrutskie et al. 2006), and the statistical weight for each galaxy that corrects for the  $\sim 8\%$  spectroscopic incompleteness of the survey (Blanton et al. 2005). Corrected for incompleteness the effective number of galaxies in our SDSS sample is 464,145.

We cross-match this sample against the public database of spectroscopic measurements for SDSS/DR7 galaxies available at the MPA-JHU team website.<sup>25</sup> The MPA-JHU database provides fluxes and EWs for all the optical emission lines of interest after carefully modeling and subtracting the stellar continuum of each galaxy using an updated, but as-yet unpublished version of the BC03 population synthesis models (Tremonti et al. 2004; Brinchmann et al. 2004; Bruzual 2007). A negligible number of objects, roughly 0.3% of galaxies in the parent VAGC sample, do not appear in the MPA-JHU database, and have been excluded. We post-process this database by adding a flag indicating the presence of a significant emission line based on the amplitude of the line relative to the variance of the continuum as described in §2.2.2, and by computing upper limits for each line using equation (1).

As a consistency check, we retrieved the SDSS spectra of a randomly selected sample of 500 galaxies from the SDSS data archive<sup>26</sup> and modeled them using the continuum and emission-line fitting code used to fit the AGES spectra in §2.2.2. In general the measured line-fluxes and EWs are consistent within the statistical uncertainties.

### 3. SPECTRAL ENERGY DISTRIBUTION MODELING

Accurate rest-frame colors, luminosities, and stellar masses require photometry that has been measured over the same physical aperture for each galaxy. In §3.1 we describe the procedure we use to build aperture-matched optical to near-IR SEDs of the galaxies in our sample, and in §3.2 and §3.3 we use these data in conjunction with the spectroscopic redshifts from AGES to derive *K*-corrections and stellar masses for the full sample, respectively.

#### 3.1. Aperture-Matched Photometry

Our general strategy is to determine the apparent colors of each galaxy using aperture photometry measured from PSF-matched images, and to use an estimate of the total magnitude in the *I*-band to set the overall normalization of the SED. This procedure is appealing because aperture colors in general have a higher S/N ratio than the total magnitude in each band, and it minimize contamination from neighboring sources.

To detect sources and to obtain an estimate of the total *I*-band magnitude of each galaxy we run SEXTRACTOR (Bertin & Arnouts 1996) in single-image mode on the unsmoothed *I*-band mosaics. We use the MAG\_AUTO (Kron-like) magnitude,  $I_{\text{AUTO}}$ , as an estimate of the integrated flux of each galaxy (Kron 1980). Note that although MAG\_AUTO may miss a significant amount of flux at faint apparent magnitudes, and for galaxies with very extended surface-brightness profiles (e.g., Graham & Driver 2005), by inserting artificial galaxies into the NDWFS *I*-band mosaics and re-running SEXTRACTOR, Brown et al. (2007) find that  $I_{\text{AUTO}}$  recovers the total (input) galaxy magnitude to within  $\sim 5\%$  for galaxies brighter than  $I_{\text{AB}} \approx 21$ , which is sufficient for our purposes.

Unfortunately,  $I_{\text{AUTO}}$  is occasionally biased toward bright magnitudes by the low surface-brightness tails of bright stars. Although AGES intentionally excluded regions around bright stars (Kochanek et al. 2011),  $I_{\text{AUTO}}$  appears to be affected for roughly 10% of the sample. Because these low surface-brightness halos are not present in the *R*-band mosaics, we re-run SEXTRACTOR on the *R*-band images and use the *R*-band MAG\_AUTO magnitude to obtain a second estimate of the total *I*-band magnitude,  $I_R$ , using the *R* – *I* color measured from the PSF-matched images in a 6'' diameter aperture (see below). These aperture colors are considerably less affected by this extended, low surface-brightness light. Following Cool et al. (2011), we obtain a new estimate of the total *I*-band magnitude,  $I'$ , using a statistic that chooses the fainter of  $I_R$  and  $I_{\text{AUTO}}$  if they differ significantly, and averages them otherwise. For  $\sim 7\%$  ( $\sim 3\%$ ) of the sample the magnitude correction computed this way exceeds 0.1 mag (0.5 mag). However, for the remainder of the sample there is a very tight correlation between  $I'$  and  $I_{\text{AUTO}}$ , with a median difference of  $< 0.01$  mag and a  $1\sigma$  scatter of  $\sim 2\%$ . To account for this small amount of scatter, in §4 we will restrict our statistical (flux-limited) galaxy sample to  $I'_{\text{AB}} < 20.4$ , which excludes  $\sim 2\%$  of the parent sample (Cool et al. 2011). Hereafter, we adopt  $I'$  as the total *I*-band magnitude of each galaxy and for clarity drop the prime superscript.

Next, we smooth the optical and near-IR mosaics to a common spatial resolution to ensure that the apparent colors are measured from the same physical area on each galaxy (Brown et al. 2007). The mosaics with the best spatial resolution (seeing) are the  $B_W$ -, *R*-, *I*-, *H*- and  $K_s$ -band mosaics, so we smooth these such that the resulting stellar PSF is a Moffat (1969) profile with  $1''.35$  FWHM and  $\beta = 2.5$ . The seeing of the *U*-, *z*-, and *J*-band mosaics is slightly worse, so we convolve these mosaics to an equivalent  $1''.6$  FWHM Moffat PSF. We then measure aperture photometry in fixed apertures ranging in diameter from 1'' to 20'' centered on the *I*-band position of each source using customized software. We use the SEXTRACTOR segmentation maps to account for pixels contaminated by neighboring objects and missing pixels, and estimate the photometric error in each aperture by computing the interval that encompasses 68% of the flux measured in 100 blank-sky apertures placed randomly within 2' of each source. Finally, we construct the SED of each galaxy using the 4'' diameter aperture magnitudes, and then scale everything by the difference between the *I*-band aperture magnitude and the total *I*-

<sup>25</sup> <http://www.mpa-garching.mpg.de/SDSS/DR7>

<sup>26</sup> <http://www.sdss.org/dr7>

band magnitude. We use  $4''$  aperture magnitudes as a compromise between choosing the largest possible aperture to maximize the S/N, while simultaneously minimizing contamination from neighboring objects. However, we did verify that using the  $6''$  diameter aperture magnitudes yields the same colors to within  $\lesssim \pm 4\%$  and with no statistically significant systematic differences.

### 3.2. $K$ -corrections

To estimate the rest-frame colors and luminosities of the galaxies in our sample, we compute  $K$ -corrections using the publically available code `kcorrect`<sup>27</sup> (v4.1.4; Blanton & Roweis 2007). For each galaxy `kcorrect` takes as input the redshift, the observed photometry, and the corresponding filter response curves, and fits the data with a non-negative linear combination of five basis templates representing a diversity of galaxy star formation histories. We have verified that the more detailed SED modeling performed in §3.3 yields the same rest-frame quantities, but adopt `kcorrect` here because of its ease-of-use and speed.

For our AGES sample we fit the aperture-matched  $UB_WRIzJHK_s$  photometry assembled in §3.1, and for our SDSS sample we fit the observed  $ugrizJHK_s$  photometry (see §2.3), all corrected for foreground Galactic extinction ( $R_V = 3.1$ ; O’Donnell 1994; Schlegel et al. 1998). We compute  $K$ -corrections for each galaxy on a case-by-case basis by selecting the bandpass that minimizes the transformation from the observed frame to the rest frame (Hogg et al. 2002; Blanton et al. 2003). For example, for our AGES sample we compute the absolute  $B$ -band magnitude (Bessell 1990) from the observed  $B_W$  magnitude at  $z \lesssim 0.2$ , from the  $R$ -band magnitude at  $0.2 \lesssim z \lesssim 0.65$ , and from the  $I$ -band magnitude at  $z \gtrsim 0.65$ . We use the best-available filter curve for each bandpass by taking into account the detector quantum efficiency, telescope throughput, and atmospheric transmission. Before fitting, we add a minimum photometric uncertainty of 0.02 mag in  $B_WRIHK_s$  in quadrature to the statistical error in each bandpass. To account for the slightly larger PSF of the  $U$ -,  $z$ -, and  $J$ -band mosaics (see §3.1), we assume a minimum error of 0.05 mag in these bands. For the SDSS we adopt minimum errors of 0.02 mag in  $gri$ , 0.05 mag in  $u$ , and 0.03 mag in  $z$  (Ivezić et al. 2004). Finally, we also adjust the SDSS  $ugriz$  magnitudes by  $-0.036$ ,  $0.012$ ,  $0.010$ ,  $0.028$ , and  $0.040$  mag, respectively, to place them on an absolute AB magnitude system (Blanton & Roweis 2007).

After fitting our AGES sample, we identified small residual, systematic offsets between the observed photometry and the magnitudes synthesized from the best-fitting models (e.g., Ilbert et al. 2005). These relative zeropoint differences can arise from errors in the photometric calibration, slightly mismatched physical apertures (e.g., due to imperfect PSF matching), imperfect filter response curves, and template mismatch. Therefore, we fit the sample iteratively, each time adjusting the observed photometry in each bandpass by the median zeropoint difference between the measured and synthesized magnitudes. The zeropoints converged to better than 0.5% in five iterations. The resulting zeropoint corrections we apply to the data, all relative to the  $I$ -band,

are:  $-0.073$ ,  $-0.032$ ,  $-0.016$ ,  $-0.037$ ,  $-0.108$ ,  $+0.042$ , and  $-0.053$  mag in  $U$ ,  $B_W$ ,  $R$ ,  $z$ ,  $J$ ,  $H$ , and  $K_s$ , respectively.

Finally, we tested the absolute photometric calibration of our AGES sample relative to the SDSS. We used the best-fitting `kcorrect` model to synthesize observed photometry in the SDSS filters for each galaxy in our AGES sample. We then queried the SDSS/DR7 database for  $ugriz$  Petrosian magnitudes of the sample, and compared the synthesized and observed magnitudes. We found a negligible ( $\lesssim 0.01$  mag) systematic difference to  $i \approx 18.5$ , and a median difference of  $0.01 - 0.02$  mag to  $i \approx 21$ , with a random scatter of  $\sim 0.05$  mag. Therefore, we conclude that the absolute photometric calibration of our AGES photometry is consistent with the SDSS to better than  $\sim 5\%$ .

### 3.3. Stellar Masses

We estimate stellar masses for the galaxies in our sample using `iSEDfit`, a Bayesian SED-fitting code that uses population synthesis models to infer the physical properties of a galaxy given its observed broadband SED (see J. Moustakas et al. 2012, in prep., for additional details). As in §2.2.2, we adopt the BC03 population synthesis models based on the Padova isochrones, the STELIB stellar library, and the Chabrier (2003) IMF. Given the broadband fluxes  $F_i$  of a galaxy at redshift  $z$  in  $i = 1, N$  filters, `iSEDfit` uses Bayes’ theorem to compute the posterior probability distribution function (PDF)

$$p(\mathbf{Q}|F_i, z) = p(\mathbf{Q}) \times p(F_i, z|\mathbf{Q}) \quad (2)$$

for a given set of model parameters  $\mathbf{Q}$  (stellar mass, age, metallicity, etc.). Here,  $p(\mathbf{Q})$  is the prior probability of the model parameters,  $p(F_i, z|\mathbf{Q})$  is the likelihood  $\mathcal{L} \propto \exp[-\chi^2(F_i, z, \mathbf{Q})/2]$  of the data given the model, and  $\chi^2$  is the usual goodness-of-fit statistic appropriate for normally distributed photometric uncertainties. We draw each model parameter from a specified prior probability distribution using a Monte Carlo technique, which is equivalent to multiplying the likelihood by the prior probability (Walcher et al. 2010). Once  $\chi^2$  has been computed for every model, the marginalized posterior PDF of the parameter of interest, for example  $p(\mathcal{M})$  for the stellar mass, follows from equation (2) after integrating over the other “nuisance” parameters (Kauffmann et al. 2003a; Salim et al. 2007; Auger et al. 2009; Taylor et al. 2011). The advantage of this approach over traditional best-fitting (maximum likelihood) techniques is that it accounts for both photometric uncertainties and physical degeneracies among different models. We adopt the median of the posterior PDF as the best estimate of the stellar mass, and the uncertainty as 1/4 of the 2.3 – 97.7 percentile range of the  $p(\mathcal{M})$  distribution, which would be equivalent to  $1\sigma$  for a Gaussian distribution.

We assume exponentially declining star formation histories of the form  $\psi(t) \propto \exp(-t/\tau)$ , but allow each model galaxy to experience one or more stochastic bursts of star formation. We draw  $1/\tau$  from a uniform distribution in the range  $0.01 - 10 \text{ Gyr}^{-1}$ , corresponding to a characteristic timescale for star formation ranging from  $\tau = 0.1 \text{ Gyr}$  (similar to an instantaneous burst), to  $\tau = 100 \text{ Gyr}$  (continuous star formation). We al-

<sup>27</sup> <http://howdy.physics.nyu.edu/index.php/Kcorrect>



low the age  $t$  (time for the onset of star formation) of each model to range with equal probability between 0.1 – 13 Gyr, although we disallow ages older than the age of the Universe at the redshift of each galaxy. We assume a uniform prior on stellar metallicity in the range  $0.004 < Z < 0.04$ , and adopt the time-dependent attenuation curve of Charlot & Fall (2000), in which stellar populations older than 10 Myr are attenuated by a factor  $\mu$  times less than younger stellar populations. We draw  $\mu$  from an order four Gamma distribution that ranges from zero to unity centered on a typical value  $\langle \mu \rangle = 0.3$  (Charlot & Longhetti 2001; Wild et al. 2011), and the  $V$ -band optical depth from an order two Gamma distribution that peaks around  $A_V \approx 1.2$  mag, with a tail to  $A_V \approx 6$  mag. Finally, we allow each model galaxy to experience one or more random bursts of star formation at time  $t_b > t$  in each 2 Gyr time interval over the lifetime of the galaxy with a probability of 50%. We characterize each burst by a duration  $\Delta t_b$ , drawn from a logarithmic distribution in the range 30 – 300 Myr, and a fractional stellar mass formed  $F_b$ , which we draw from a logarithmic distribution from 0.01 – 4 (Salim et al. 2007; Wild et al. 2009). For simplicity, we assume that the stellar population that forms in the burst has the same stellar metallicity and is attenuated by the same amount of dust as the pre-burst stellar population.

The largest systematic uncertainty affecting our stellar mass estimates is likely due to our choice of IMF, although if the IMF is spatially and temporarily invariant (i.e., universal) as is commonly assumed, then adopting a different IMF should simply shift all our stellar masses by a fixed amount. For example, the Salpeter (1955) and Kroupa (2001) IMFs are 0.25 dex and 0.03 dex heavier than the Chabrier (2003) IMF, respectively, while the so-called “diet Salpeter” IMF of Bell & de Jong (2001) is 0.1 dex lighter. Although there are recent tantalizing suggestions of a Salpeter (or heavier) IMF in early-type galaxies (van Dokkum & Conroy 2010; Treu et al. 2010), current observations heavily favor a universal Chabrier- or Kroupa-like IMF in nearby star-forming disk galaxies, including the Milky Way (Bastian et al. 2010, and references therein).

Varying our prior distributions—for example, adopting different metallicity or attenuation priors, or assuming smooth, burst-free star-formation histories—changes our stellar masses by  $\lesssim 0.1$  dex in the mean, and by less than a factor of two for individual objects. We also test the effect of adopting different population synthesis models (Maraston 2005; Conroy & Gunn 2010) and find comparable systematic differences in the derived stellar masses for both our SDSS and AGES samples, i.e. typically  $\lesssim 0.1$  dex. We refer the interested reader to Kannappan & Gawiser (2007), Marchesini et al. (2009), and Muzzin et al. (2009) for recent detailed discussions of the uncertainties associated with deriving stellar masses from broadband photometry.

#### 4. SAMPLE SELECTION

The AGES main galaxy sample contains 12,473 galaxies brighter than  $I_{AB} = 20.45$  with well-measured redshifts over 7.9 deg<sup>2</sup> of the Boötes field (Kochanek et al. 2011). We exclude from this sample five Hectospec configurations that could not be flux-calibrated (see §2.2.1), and two additional configurations with very poor flux-

TABLE 1  
AGES AND SDSS GALAXY SAMPLES

Sample	$N_{\text{gal}}^{\text{a}}$	Section <sup>b</sup>
AGES		
Parent	10838	4
Emission-Line	4033	4.1
SF <sup>c</sup>	3205	4.2
AGN	828	4.2
Abundance <sup>d</sup>		
KK04	2975	5.3
T04	3191	5.3
M91	2969	5.3
SDSS		
Parent	427504	2.3
Emission-Line	108040	4.1
SF <sup>c</sup>	76411	4.2
AGN	31629	4.2
Abundance <sup>d</sup>		
KK04	75378	5.3
T04	75976	5.3
M91	75313	5.3

<sup>a</sup> Number of galaxies in each sample.

<sup>b</sup> Section containing details regarding how we select each sample.

<sup>c</sup> Star-forming galaxies.

<sup>d</sup> Number of galaxies with well-measured oxygen abundances based on the McGaugh (1991, M91), Tremonti et al. (2004, T04), and Kobulnicky & Kewley (2004, KK04) abundance calibrations.

ing. However, we preserve the statistical completeness of the sample by upweighting the remaining objects on a field-by-field basis to account for the missing configurations. Finally, we restrict our analysis to galaxies with  $15.45 < I_{AB} < 20.4$  and  $0.05 < z < 0.75$ , leaving 10,838 galaxies (Table 1), or an effective sample of 24,525 galaxies after correcting for sparse-sampling and other sources of incompleteness (see §2.2.1). In §4.1 we select a subset of these objects with the requisite nebular emission lines to estimate their oxygen abundances, and in §4.2 we apply a variety of multiwavelength criteria to identify and remove AGN from our sample. Finally, in §4.3 we present some of the basic properties of our final sample of star-forming emission-line galaxies, and define volume-limited subsamples.

##### 4.1. Selecting Emission-Line Galaxies

We select a sample of emission-line galaxies based on the strength of  $H\beta$ . The principal advantages of using  $H\beta$  are that its strength is proportional to the instantaneous SFR, and it is less sensitive to variations in dust attenuation, excitation, and metallicity than other strong optical emission lines (Kennicutt 1992; Moustakas et al. 2006; Gilbank et al. 2010). From a practical perspective,  $H\beta$  also has the advantage that it is observable in both AGES and the SDSS over the full redshift range of interest.

In the top panel of Figure 2 we plot the  $H\beta$  luminosity,  $L(H\beta)$ , versus redshift for all the galaxies in AGES with a significant  $H\beta$  emission line. For simplicity we ignore both relative and absolute aperture effects in our selection (see also §7.4). We select all objects (*small black points*) above the black curve, which corresponds to a flux limit of  $F(H\beta) > 3 \times 10^{-17}$  erg s<sup>-1</sup> cm<sup>-2</sup>. In the bottom

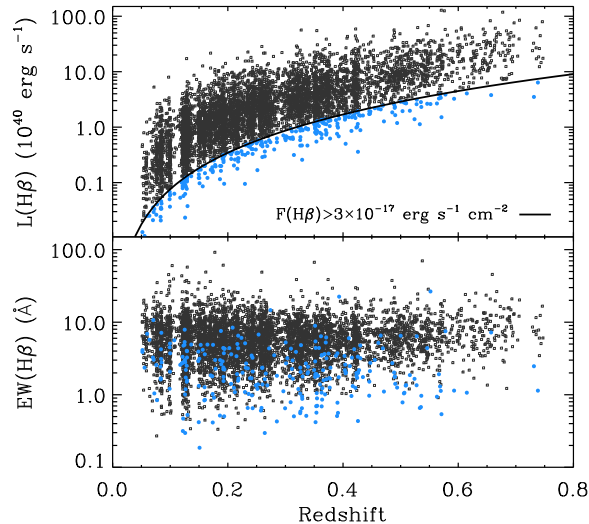


FIG. 2.— Selection of emission-line galaxies in AGES based on the  $H\beta$  line-strength. In the top panel we plot  $H\beta$  luminosity,  $L(H\beta)$ , vs. redshift, and select all galaxies (*small black points*) with an observed  $H\beta$  line-flux  $F(H\beta) > 3 \times 10^{-17} \text{ erg s}^{-1} \text{ cm}^{-2}$  (*solid black curve*). The bottom panel plots rest-frame  $EW(H\beta)$  vs. redshift for the resulting emission-line sample, where for comparison we also show the objects that fail our fiducial flux cut (*light blue points*). Our selection on  $H\beta$  luminosity is physically motivated because  $L(H\beta)$  is proportional to the instantaneous SFR.

panel we plot rest-frame  $EW(H\beta)$  against redshift for the resulting emission-line sample, where for comparison we also show the objects that fail our fiducial flux cut (*light blue points*). The  $EW(H\beta)$ -redshift plot shows that our sample spans a wide range of  $EW(H\beta)$  at all redshifts, although the distribution narrows at higher redshift due to the increasing limiting  $L(H\beta)$  luminosity.

In order to estimate the gas-phase oxygen abundances of the galaxies in our sample we require a measurement of the  $[O II]$  and  $[O III] \lambda 5007$  emission lines (see §5.2). In Figure 3 we plot  $[O II]/H\beta$  and  $[O III]/H\beta$  versus redshift for our  $H\beta$ -selected AGES sample. The small black points correspond to well-measured line-ratios, while the orange arrows represent upper limits. Focusing on  $[O II]$  first (Fig. 3, *top*), we find that the data exhibit a distinct lower envelope around  $\log([O II]/H\beta) = -0.3$  (*dashed line*), below which we find only  $\sim 6\%$  of our sample, including nearly all the upper limits. Visual inspection of the spectra with low  $[O II]/H\beta$  ratios reveals that many exhibit a highly reddened stellar continuum, i.e., they are dusty. However, because these objects constitute such a small fraction of the parent sample, and because their redshift distribution is consistent with the redshift distribution of the parent  $H\beta$  sample, we do not expect that excluding them will bias our results. Therefore, in addition to our  $H\beta$  flux cut, we further restrict our sample to have a well-measured  $[O II]$  emission line with  $\log([O II]/H\beta) > -0.3$ .

In contrast to  $[O II]/H\beta$ , the  $[O III]/H\beta$  ratios for approximately one-quarter of the  $H\beta$ -selected AGES galaxies are upper limits (Fig. 3, *bottom*). This result is not terribly surprising because  $[O III]$  is especially sensitive to variations in metallicity and excitation; in particular, the  $[O III]/H\beta$  ratio decreases precipitously with increasing

metallicity and decreasing excitation (Kewley & Dopita 2002). However, we show in §7.1 that the potential bias against metal-rich galaxies in an  $[O III]$ -limited sample does not significantly affect our measurement of the  $M - Z$  relation. Therefore, to significantly simplify the subsequent analysis, we proceed by requiring the galaxies in our emission-line sample to have a well-measured  $[O III]$  emission line (the black points in Fig. 3, *bottom*).

The final number of emission-line galaxies in AGES satisfying our  $H\beta$ ,  $[O II]$ , and  $[O III]$  selection criteria is 4033, or 37% of our parent sample. For our SDSS sample we apply the same selection criteria described above with the exception of a correspondingly brighter  $H\beta$  flux limit,  $F(H\beta) > 1 \times 10^{-16} \text{ erg s}^{-1} \text{ cm}^{-2}$ , leaving 108,040 galaxies, or 25% of the parent sample. For reference, not requiring our SDSS sample to have a well-measured  $[O III]$  line would increase the sample by approximately one-third. In Table 1 we summarize the total number of objects in these and all subsequent subsamples.

#### 4.2. Identifying and Removing AGN

The Balmer and collisionally excited forbidden lines present in the integrated optical spectra of galaxies can arise from photoionization by young, massive stars, or by the non-thermal photoionizing continuum of an AGN. Therefore, when deriving abundances from optical emission lines it is crucial that AGN be identified and removed from the sample. We leverage the tremendous multiwavelength coverage of the Boötes field to identify AGN using a variety of criteria based on optical, X-ray, mid-IR, and radio observations.

Beginning with our parent sample of emission-line galaxies (see §4.1), we identify type 1 (broad-line) AGN

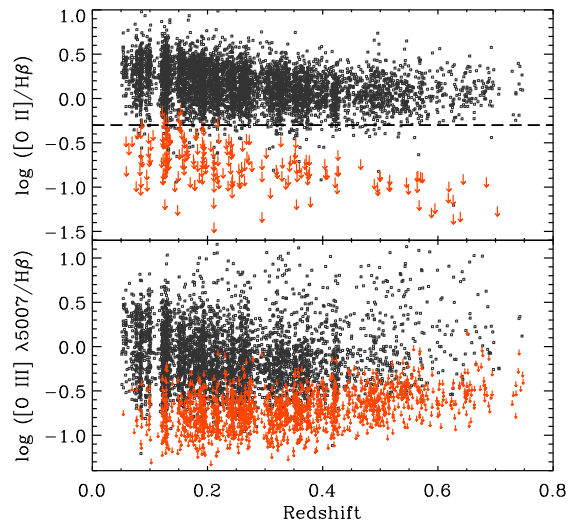


FIG. 3.— Metallicity-sensitive  $[O II]/H\beta$  and  $[O III] \lambda 5007/H\beta$  line-ratios vs. redshift for our  $H\beta$ -limited sample of galaxies (see Fig. 2). We represent galaxies with well-measured line-ratios using small black points and upper limits using orange arrows. In the upper panel the dashed line at  $\log([O II]/H\beta) = -0.3$  represents the criterion we use to select galaxies with significant  $[O II]$  emission, which eliminates just  $\sim 6\%$  of the  $H\beta$ -selected sample. By contrast, the bottom panel shows that the fraction of galaxies with only upper limits on  $[O III] \lambda 5007$  is not negligible due the greater sensitivity of  $[O III]$  to variations in metallicity and excitation.

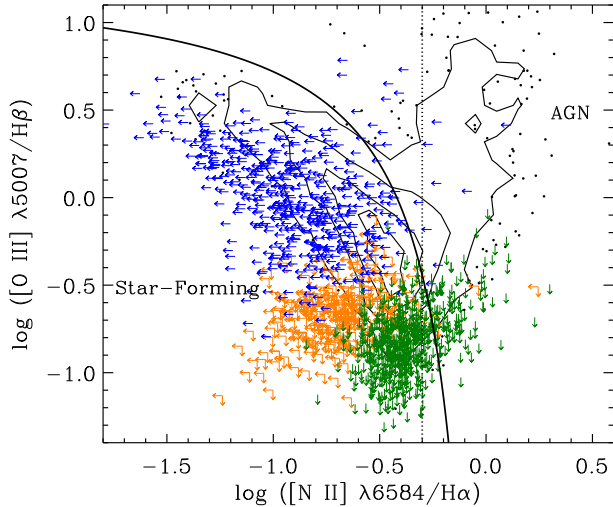


FIG. 4.— AGES emission-line diagnostic (BPT) diagram used to classify our sample into star-forming galaxies or AGN based on their position below or above the solid curve, respectively (Kauffmann et al. 2003c). The contours, enclosing 25%, 50%, 75%, and 95% of the sample, represent galaxies with well-measured  $[\text{N II}]/\text{H}\alpha$  and  $[\text{O III}]/\text{H}\beta$  ratios; the small black points are individual galaxies outside the 95% contour level. The arrows represent objects with  $1\sigma$  upper limits on either: (1)  $[\text{N II}]/\text{H}\alpha$  and  $[\text{O III}]/\text{H}\beta$  (orange left- and down-pointing arrows); (2) just  $[\text{N II}]/\text{H}\alpha$  (blue left-pointing arrows); or (3) just  $[\text{O III}]/\text{H}\beta$  (green down-pointing arrows). Objects with upper limits on any of these line-ratios can be classified as star-forming if they lie in the star-forming region of the BPT diagram; otherwise, their classification is ambiguous. However, objects with upper limits on  $[\text{O III}]/\text{H}\beta$  can be classified as AGN nearly unambiguously if they have  $\log([\text{N II}]/\text{H}\alpha) > -0.3$  (vertical dotted line).

as objects with broad (typically,  $\sigma > 800 \text{ km s}^{-1}$  FWHM)  $\text{H}\alpha$ ,  $\text{H}\beta$ , or  $\text{Mg II } \lambda 2800$  emission, depending on which lines are observable given the AGES spectral range. In our SDSS sample broad-line AGN have been removed already. In addition, we remove any object with significant  $[\text{Ne V}] \lambda 3426$  emission, which is a hallmark of AGN activity, or an enhanced  $[\text{Ne III}] \lambda 3869/\text{H}\beta$  ratio, which is also indicative of a non-thermal photoionizing radiation field (Rola et al. 1997; Dessauges-Zavadsky et al. 2000; Pérez-Montero et al. 2007).<sup>28</sup>

Next, we use the standard  $[\text{O III}] \lambda 5007/\text{H}\beta$  versus  $[\text{N II}] \lambda 6584/\text{H}\alpha$  emission-line diagnostic diagram (Fig. 4) to identify type 2 (narrow-line) AGN (Baldwin et al. 1981; Veilleux & Osterbrock 1987; Kewley et al. 2001; hereafter, the BPT diagram). We do not show the SDSS BPT diagram because it exhibits the same basic features (see, e.g., Kauffmann et al. 2003c). We identify objects located below and to the left of the empirical demarcation (solid curve) proposed by Kauffmann et al. (2003c) as star-forming galaxies, and the remaining objects as AGN. Stasińska et al. (2006) estimate that the maximum contribution to the integrated  $\text{H}\beta$  line-flux from an AGN for an object classified as star-forming using the Kauffmann et al. (2003c) criterion is  $\sim 3\%$ . For comparison, the “maximum starburst” curve proposed

by Kewley et al. (2001) allows up to a 20% – 30% contribution to  $\text{H}\beta$  from an AGN. We adopt the stricter Kauffmann et al. (2003c) demarcation to minimize the metallicity bias incurred from contamination to the nebular emission lines from AGN (see §7.3).

In Figure 4 we differentiate between four different scenarios: (1) galaxies with well-measured  $[\text{N II}]/\text{H}\alpha$  and  $[\text{O III}]/\text{H}\beta$  line-ratios (contours and greyscale); (2) objects with  $[\text{N II}]/\text{H}\alpha$  upper limits (blue arrows); (3) objects with  $[\text{O III}]/\text{H}\beta$  upper limits (green arrows); and (4) galaxies with both  $[\text{N II}]/\text{H}\alpha$  and  $[\text{O III}]/\text{H}\beta$  upper limits (orange arrows). An object with an upper limit on any of these line-ratios can be classified as star-forming if it lies in the star-forming region of the BPT diagram; otherwise, its classification is ambiguous, with one exception: a galaxy can be classified as an AGN if it has an upper limit on  $[\text{O III}]/\text{H}\beta$  but a well-measured  $[\text{N II}]/\text{H}\alpha$  ratio with  $\log([\text{N II}]/\text{H}\alpha) > -0.3$  (vertical dotted line).

In order to classify the rest of the AGES sample, including all the objects at  $z > 0.4$  (which lack  $[\text{N II}]/\text{H}\alpha$  measurements), we must rely on other diagnostics of AGN activity. Recognizing the difficulty of measuring the  $[\text{N II}]/\text{H}\alpha$  ratio of intermediate-redshift galaxies, Yan et al. (2011) have proposed a new BPT-like diagnostic diagram that replaces the  $[\text{N II}]/\text{H}\alpha$  ratio with the rest-frame  $U - B$  color (see Lamareille 2010, Lara-López et al. 2010a, and Juneau et al. 2011 for alternative empirical diagnostic diagrams). The physical motivation behind this classification scheme is that AGN are more likely to be found in galaxies dominated by evolved stellar populations (e.g., Kauffmann et al. 2003c); therefore, at fixed  $[\text{O III}]/\text{H}\beta$  ratio, galaxies whose integrated emission-line spectrum is dominated by star-formation are more likely to be blue in their  $U - B$  color.

In Figure 5 we plot  $U - B$  versus  $[\text{O III}]/\text{H}\beta$  for our (left) SDSS and (right) AGES galaxy samples. The light blue contours represent objects classified as star-forming galaxies using the BPT diagram, the grey contours represent objects classified as AGN, and the dark blue points indicate objects that cannot be classified using the BPT diagram. For clarity we do not include in this figure the small number of SDSS galaxies that could not be classified using the BPT diagram, although nearly all of them would be classified as AGN using the Yan et al. (2011) diagnostic diagram. Among our AGES galaxies, the tan squares represent objects identified as AGN using various other optical, X-ray, mid-IR, and radio criteria, as described below. Finally, the solid line is the empirical boundary proposed by Yan et al. (2011) to separate star-forming galaxies from AGN, which are located below and above the solid line, respectively.

Examining Figure 5, we find that the Yan et al. (2011) diagnostic diagram successfully classifies as star-forming more than 98% of the BPT-classified star-forming galaxies; however, it also identifies as star-forming roughly 50% of the objects classified as AGN using the BPT diagram. In other words, the diagram has high completeness for star-forming galaxies, but at the expense of a relatively high contamination rate (i.e., low purity). However, as emphasized by Yan et al. (2011), nearly all of these “misclassified” objects are, in fact, composite systems with an admixture of star-formation and AGN activity. Moreover, the contribution from the AGN to the integrated emission-line spectrum in composite sys-

<sup>28</sup> Strong  $[\text{Ne III}] \lambda 3869$  emission is also observed in metal-poor dwarf galaxies (e.g., Izotov & Thuan 1998); however, these types of objects are only present in our sample at low redshift and easily identified through visual inspection of their optical spectrum.



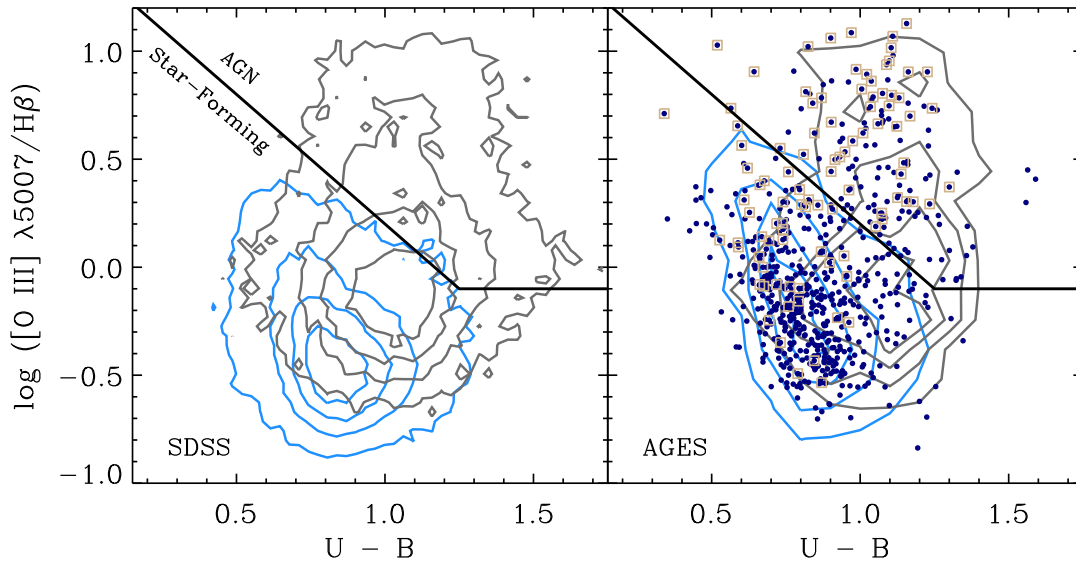


FIG. 5.— BPT-like diagnostic diagram for our (*left*) SDSS and (*right*) AGES galaxy samples. This diagram has been proposed by Yan et al. (2011) as an empirical means of segregating star-forming galaxies (*below the solid line*) from AGN (*above the solid line*) when the ionization-sensitive  $[\text{N II}]/\text{H}\alpha$  ratio cannot be measured. The blue contours enclose 25%, 50%, 75%, and 95% of the galaxies classified as star-forming using the BPT diagram (see Fig. 4 and §4.2), while the grey contours show the distribution of BPT-classified AGN. The dark blue points represent galaxies that cannot be classified using the BPT diagram. For clarity we do not plot the small number of unclassified SDSS galaxies, although nearly all of them lie in the AGN portion of this diagnostic diagram. Within the AGES sample, the tan squares represent galaxies classified as AGN using other multiwavelength (X-ray, mid-IR, and radio) criteria. With respect to objects classified as star-forming galaxies using the BPT diagram, we find that this technique has high *completeness*, but low *purity*. In other words, while  $> 98\%$  of BPT-classified star-forming galaxies are successfully classified as star-forming using this diagnostic diagram, more than 50% of AGN are *also* identified as star-forming. As noted by Yan et al. (2011), however, the bulk of these objects are *composite* systems, with an admixture of ongoing star-formation and AGN activity.

tems is always sub-dominant (5% – 30%; Stasińska et al. 2006).

To mitigate the tendency for the Yan et al. (2011) diagnostic diagram to classify composite systems as pure star-forming galaxies, we utilize a variety of complementary multiwavelength criteria to identify AGN in our AGES sample (see also Hickox et al. 2009; Rujopakarn et al. 2010; Assef et al. 2011). First, we classify as an AGN any object with more than a 50% probability of being an X-ray point source (Kenter et al. 2005; Brand et al. 2006). Although the X-ray emission in some of these objects may arise from processes associated with star formation (e.g., Watson et al. 2009), roughly 90% of them have total 0.5 – 7 keV X-ray luminosities  $L_X \gtrsim 10^{42}$  erg s $^{-1}$ , consistent with hosting an AGN (Georgakakis et al. 2006). We also isolate objects lying in the “Stern wedge” of the IRAC [3.6] – [4.5] versus [5.8] – [8.0] color-color diagram (Stern et al. 2005), which is effective at identifying AGN that are both obscured and unobscured in the X-ray (Hickox et al. 2007; Gorjian et al. 2008; Ashby et al. 2009). Finally, we compute the radio power at 1.4 GHz,  $P_{1.4}$ , of the radio sources in our sample (see §2.1.2),  $K$ -corrected assuming an intrinsic power-law spectrum  $S_\nu \propto \nu^{-\alpha}$  with  $\alpha = 0.5$  (Prandoni et al. 2006), and identify AGN as sources having  $\log P_{1.4} > 23.8$  W Hz $^{-1}$  (Kauffmann et al. 2008; Hickox et al. 2009).

One potential objection to the preceding analysis is that AGN identified at X-ray, mid-IR, and radio wavelengths should not necessarily be removed from an *optical* emission-line abundance study. For example, there exists

an interesting (albeit rare) class of objects with significant X-ray emission but with no discernable evidence of AGN activity in the optical, so-called X-ray Bright Optically Normal Galaxies (XBONGs; Comastri et al. 2002; Civano et al. 2007; Yan et al. 2011). Similarly, AGN identified based on their mid-IR colors may be so obscured at optical wavelengths as to not affect the optical emission lines in any important way. Nevertheless, we conservatively reject any object (not otherwise classified as star-forming using the BPT diagram) whose optical emission lines *might* be contaminated by an AGN. The reason for adopting this position is that the oxygen emission-line ratios of unidentified AGN are similar to those of metal-poor star-forming galaxies, and therefore could bias the amount of metallicity evolution that we infer, a point that we revisit in §7.3.

To summarize, our final SDSS and AGES star-forming galaxy samples contain 76, 411 and 3205 galaxies, respectively (see Table 1). However, 432 (14%) of the AGES emission-line galaxies, 85% of which are at  $z > 0.4$ , were classified as star-forming using the Yan et al. (2011) diagnostic diagram, which carries a potential  $\sim 50\%$  contamination rate from composite (i.e., low-level) AGN. On the other hand, by using additional multiwavelength AGN diagnostics it is likely that the contamination rate in our sample is much lower. Nevertheless, we conservatively estimate that  $\lesssim 10\%$  of the galaxies in our star-forming galaxy sample, or up to  $\sim 50\%$  of the objects at  $z > 0.4$ , may host weak (composite) AGN. We show in §7.3, however, that these unidentified optical AGN, if present, have a minimal effect on our conclusions.

## 4.3. Sample Properties

In Figure 6 we compare the distributions of redshift, absolute  $B$ -band magnitude,  $U - B$  color, and stellar mass for the star-forming galaxies in AGES (*filled light blue histograms*) against the full parent sample (*unfilled light grey histograms*), both corrected for the statistical incompleteness of the survey (see §2.2.1). We also show for comparison the distribution of properties for our SDSS star-forming galaxy sample (*unfilled dark red histograms*), where we have scaled the SDSS distributions down by a factor of 15 for visualization purposes. Not unexpectedly, our emission-line cuts preferentially remove massive, luminous galaxies with red optical colors, the majority of which are presumably old, early-type galaxies with little or no ongoing star formation (e.g., Kauffmann et al. 2003b; Zhu et al. 2010, but see the discussion in §7.1). Corrected for incompleteness, the median (mean) redshift of our SDSS sample is  $z_{\text{med}} = 0.087$  (0.094), compared to  $z_{\text{med}} = 0.27$  (0.30) for our AGES sample; otherwise, the distributions of luminosity, stellar mass, and color for the two samples are very similar.

In Figure 7 we examine the properties of the star-forming galaxies in AGES in more detail by plotting  $B$ -band absolute magnitude and stellar mass versus redshift. The distribution of points follows the characteristic shape of a flux-limited survey, in which intrinsically luminous, massive galaxies are observable over the full range of redshifts, unlike low-luminosity galaxies (i.e., Malmquist bias). This figure also reveals the relative dearth of luminous, massive star-forming galaxies

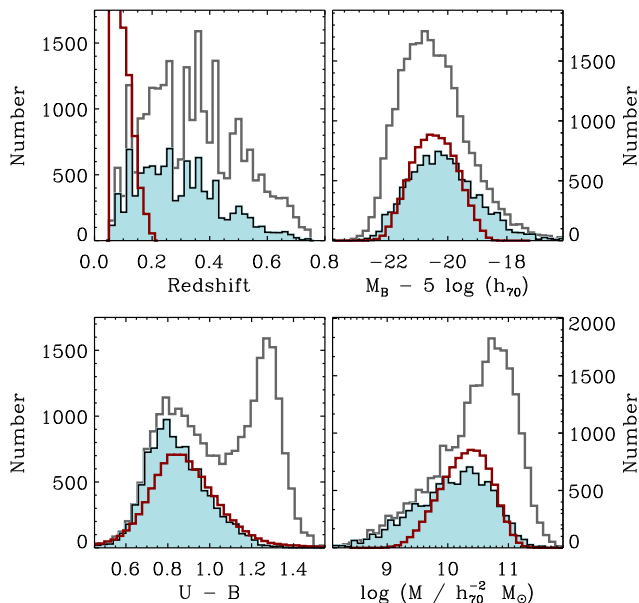


FIG. 6.— Distribution of redshift, absolute  $B$ -band magnitude, rest-frame  $U - B$  color, and stellar mass for the AGES parent sample (*unfilled light grey histograms*), and our sample of star-forming emission-line galaxies (*filled light blue histograms*), weighted to correct for the statistical incompleteness of the survey (see §2.2.1). The unfilled dark red histograms show for comparison the distributions of the same properties for our SDSS star-forming galaxy sample, where we have scaled the SDSS distributions down by a factor of 15 for comparison purposes. As expected, our emission-line selection criteria preferentially remove massive, luminous, optically red galaxies.

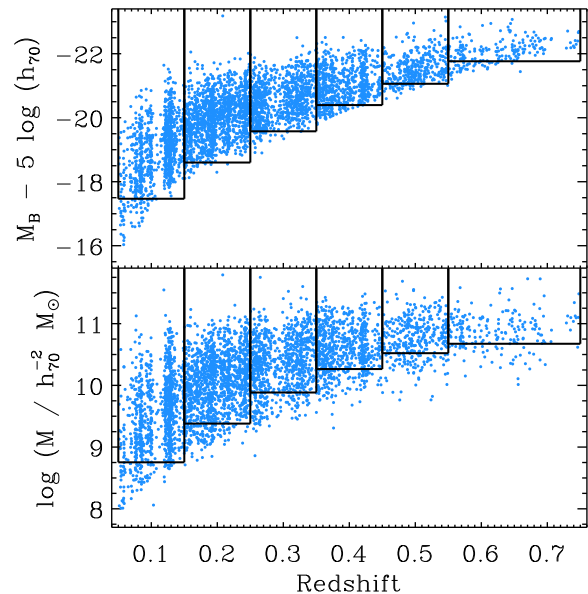


FIG. 7.— Absolute  $B$ -band magnitude and stellar mass vs. redshift for the star-forming galaxies in AGES. The black boundaries demarcate volume-limited subsamples in six redshift bins centered on  $z = 0.1, 0.2, 0.3, 0.4, 0.5,$  and  $0.65$  (see §4.3 and Table 2).

in AGES at low redshift due to the limited cosmological volume probed.

We use Figure 7 to calculate the minimum absolute magnitude and stellar mass above which our sample is volume-limited as a function of redshift. The limiting  $M_B$  is directly proportional to the survey flux limit, modulo small variations in  $K$ -corrections among different galaxy types. However, the limiting stellar mass has an additional dependence on the mass-to-light ratio (i.e., star-formation history) of each galaxy. At fixed stellar mass and redshift a galaxy with a large (small) mass-to-light ratio will lie preferentially below (above) the survey flux limit. Since observations suggest that galaxies of a given mass with high star formation rates tend to be metal-poor (Mannucci et al. 2010; Yates et al. 2011), properly accounting for the stellar mass limit ensures that we do not bias our measurement of the  $\mathcal{M} - Z$  relation toward lower metallicity.

To calculate the absolute magnitude and stellar mass limits we adopt an empirical approach (see, e.g., Lamareille et al. 2009). First, we divide AGES into six redshift bins centered on  $z = 0.1, 0.2, 0.3, 0.4, 0.5,$  and  $0.65$ , corresponding to approximately equal intervals of cosmic time ( $\sim 1$  Gyr). Next, we compute the absolute magnitude and stellar mass each galaxy would have if its apparent magnitude,  $I$ , equalled the magnitude limit of the survey,  $I_{\text{AB,lim}} = 20.4$ . Specifically, we calculate

$$M_{B,\text{min}} = M_B - (I - I_{\text{lim}}) \quad (3)$$

and

$$\log(\mathcal{M}_{\text{min}}/\mathcal{M}_{\odot}) = \log(\mathcal{M}/\mathcal{M}_{\odot}) + 0.4(I - I_{\text{lim}}) \quad (4)$$

for each galaxy. The distributions of  $M_{B,\text{min}}$  and

TABLE 2  
AGES LIMITING  $B$ -BAND MAGNITUDE &  
STELLAR MASS<sup>a</sup>

Redshift Range	$M_{B,\text{lim}}$	$\log(\mathcal{M}_{\text{lim}}/\mathcal{M}_{\odot})$
0.05 – 0.15	-17.47	8.75
0.15 – 0.25	-18.60	9.38
0.25 – 0.35	-19.58	9.88
0.35 – 0.45	-20.40	10.26
0.45 – 0.55	-21.06	10.52
0.55 – 0.75	-21.76	10.67

<sup>a</sup> Absolute  $B$ -band magnitude and stellar mass as a function of redshift above which the AGES star-forming galaxy sample is more than 50% complete, accounting for variations in  $K$ -corrections and mass-to-light ratio.

$\mathcal{M}_{\text{min}}$  in each redshift slice reflect the variations in  $K$ -corrections and mass-to-light ratio among different galaxies. We then define  $M_{B,\text{lim}}$  and  $\mathcal{M}_{\text{lim}}$  as the luminosity and stellar mass that includes more than 50% of the galaxies. In Figure 7 we show the boundaries that define our volume-limited samples in each redshift interval, and list the 50% completeness limits in Table 2. For reference, the 75% and 95% stellar mass completeness limits are roughly 0.15 dex and 0.4 dex higher, while the corresponding limiting  $M_B$  values are approximately 0.1 mag and 0.35 mag brighter, respectively.

## 5. DERIVING GAS-PHASE OXYGEN ABUNDANCES

### 5.1. Background on Strong-Line Metallicity Calibrations

The observational technique of using optical emission lines to derive the physical conditions (density, temperature, chemical composition) of the ionized gas in H II regions and star-forming galaxies has a long, rich history (Aller 1942; Shields 1990; Stasińska 2007). In particular, considerable effort has gone into using optical spectroscopy to infer the abundance of oxygen in star-forming regions. Oxygen is important because it is the most abundant element (by number) in the Universe after hydrogen and helium (Asplund et al. 2009), making it a crucial coolant in the interstellar medium; moreover, all the principal oxygen transitions are observable in the rest-frame optical.

The classical, so-called *direct* method of inferring the gas-phase oxygen abundance is to measure the electron temperature of the ionized gas from the strength of an auroral line, usually [O III]  $\lambda 4363$ , relative to a nebular line such as [O III]  $\lambda 5007$  (Dinerstein 1990; Garnett 2004; Osterbrock & Ferland 2006).<sup>29</sup> Unfortunately, [O III]  $\lambda 4363$  and other temperature-sensitive auroral lines (e.g., [N II]  $\lambda 5755$  [S III]  $\lambda 6312$ , [O II]  $\lambda 7325$ ) become vanishingly weak with increasing metallicity; therefore, they are rarely detected in the integrated spectra of galaxies observed as part of flux-limited surveys such as AGES and the SDSS, which typically include rel-

atively luminous, metal-rich galaxies. For example, electron temperatures have been measured for fewer than  $\sim 0.1\%$  of galaxies in the entire SDSS database, all of which are relatively nearby, metal-poor dwarfs (Kniazev et al. 2004; Izotov et al. 2006).

In light of the observational challenges confronting direct, electron-temperature abundance measurements, complementary methods have been developed that rely exclusively on the strongest emission lines in the rest-frame optical. These so-called *strong-line* methods are statistical correlations between various line-ratios and the gas-phase oxygen abundance,  $12 + \log(\text{O}/\text{H})$ . Unfortunately, different calibrations yield widely different oxygen abundances *based on the same input emission-line spectrum*. The magnitude of the systematic differences in metallicity depends on which calibrations are being compared, but they can be as large as  $\sim 0.7$  dex, or a factor of  $\sim 5$  (Kennicutt et al. 2003; Pérez-Montero & Díaz 2005; Liang et al. 2006b; Nagao et al. 2006; Bresolin et al. 2004, 2005; Bresolin 2007; Kewley & Ellison 2008; Lopez-Sanchez & Esteban 2010; Stasińska 2010; Moustakas et al. 2010). In particular, so-called *theoretical* strong-line methods, which are based on *ab initio* photoionization model calculations (e.g., McGaugh 1991; Charlot & Longhetti 2001; Kewley & Dopita 2002), yield oxygen abundances that are, on average, several times higher than abundances derived using either the direct method, or *empirical* strong-line methods, which are calibrated against H II regions with direct abundance estimates (e.g., Pilyugin 2000, 2001; Denicoló et al. 2002; Pettini & Pagel 2004; Pérez-Montero & Díaz 2005; Pilyugin & Thuan 2005; Stasińska 2006; Yin et al. 2007).

### 5.2. Deriving Metallicities Using the $R_{23}$ Parameter

Because of the poorly understood systematic uncertainties in the nebular abundance scale described in §5.1, it is important that the requisite emission lines we use to derive metallicities are observable over the full redshift range of interest,  $z = 0.05 - 0.75$ . The combination of nebular lines that satisfies this requirement for our SDSS and AGES samples is the  $R_{23}$  parameter (Pagel et al. 1979),

$$R_{23} \equiv \frac{[\text{O II}] \lambda 3727 + [\text{O III}] \lambda \lambda 4959, 5007}{\text{H}\beta \lambda 4861}. \quad (5)$$

The  $R_{23}$  parameter is a popular and widely used abundance diagnostic for several reasons. First, its strength is directly proportional to both principal ionization states of oxygen, and therefore does not require large, uncertain ionization corrections; the relative amount of neutral oxygen and  $\text{O}^{3+}$  is negligible in star-forming regions across a wide range of physical conditions. Second,  $R_{23}$  is explicitly related to the oxygen abundance, unlike other popular diagnostics that depend implicitly on the relative abundance of additional elements like nitrogen (see §7.2). Finally,  $R_{23}$  can be measured from the ground using a combination of optical and near-infrared spectroscopy from  $z = 0 - 4$ , which allows the chemical enrichment histories of galaxies to be studied using a consistent metallicity diagnostic over 90% of the age of the Universe (Kennicutt 1998a; Maiolino et al. 2008; Richard et al. 2011).

<sup>29</sup> The abundance of oxygen and other heavy elements can be inferred from the optical metal-recombination lines as well. However, because these lines are extraordinarily weak, they have been measured in only a relatively small number of Galactic and extragalactic H II regions and starburst dwarf galaxies (Esteban et al. 2009, and references therein).



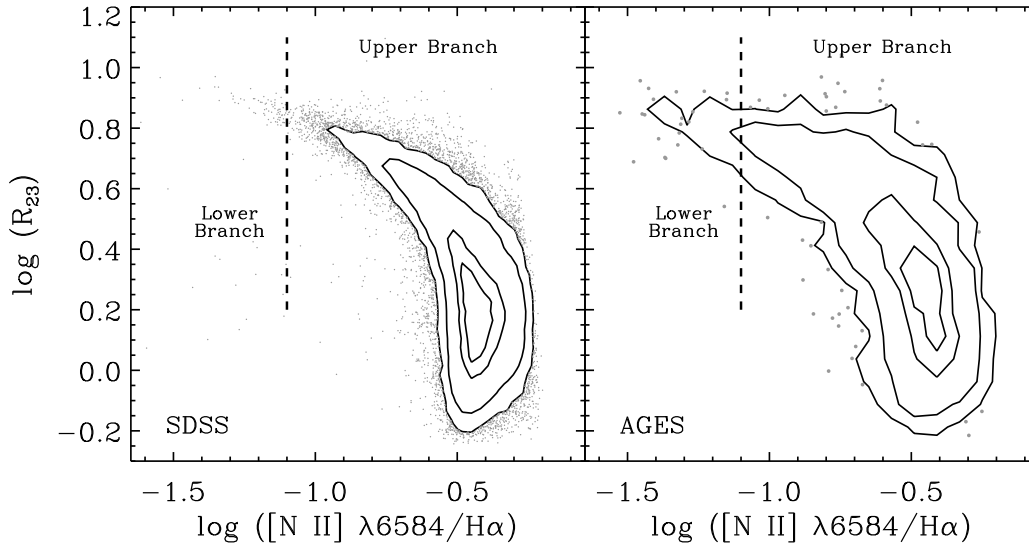


FIG. 8.— Emission-line diagnostic diagram used to assign galaxies to the *upper*,  $\log([\text{N II}]/\text{H}\alpha) > -1.1$ , and *lower*  $\log([\text{N II}]/\text{H}\alpha) < -1.1$ , branches of the  $R_{23}$ -O/H relation (see §5.2) for our (*left*) SDSS and (*right*) AGES star-forming galaxy samples with well-measured  $[\text{N II}]/\text{H}\alpha$  ratios. For reference, the contours enclose 25%, 50%, 90%, and 97.5% of the sample, and the small grey points represent galaxies that lie outside the 97.5% contour level. This diagram demonstrates that the galaxies in both samples overwhelmingly belong to the upper  $R_{23}$  branch.

To explore the effect on our conclusions of choosing a particular strong-line calibration, we carry out our analysis using three independent theoretical strong-line calibrations of  $R_{23}$ : McGaugh (1991), Kobulnicky & Kewley (2004), and Tremonti et al. (2004), hereafter referred to as the M91, KK04, and T04 abundance calibrations, respectively. At a fixed value of  $R_{23}$ , both observations and photoionization modeling show that there is a second-order dependence of O/H on the ionization parameter,  $U$ , or the hardness of the ionizing radiation field (Shields 1990; McGaugh 1991; Pilyugin 2001; Kewley & Dopita 2002). The M91 and KK04 calibrations constrain the ionization parameter using the  $O_{32}$  ratio, where

$$O_{32} \equiv \frac{[\text{O III}] \lambda\lambda 4959, 5007}{[\text{O II}] \lambda 3727}, \quad (6)$$

while the T04 calibration ignores this effect. All three calibrations are based on photoionization models, and therefore they yield metallicities that are considerably higher than those implied by the direct method or empirical strong-line calibrations (e.g., Pettini & Pagel 2004; Pilyugin & Thuan 2005; see Kewley & Ellison 2008). However, as Moustakas et al. (2010) argue, existing empirical strong-line calibrations should be applied to integrated galaxy spectra with great care because they are being extrapolated into a part of physical parameter space that is not well-constrained by current observations of H II regions. In Appendix A we compare the M91, KK04, and T04 calibrations in more detail.

Despite its popularity and wide-spread use,  $R_{23}$ -based abundances suffer from several potential systematic uncertainties. First, the relationship between  $R_{23}$  and O/H is famously double-valued (see, e.g., Fig. A1): a given value of  $R_{23}$  can correspond to a solution on the metal-rich *upper branch*, or on the metal-poor *lower branch*; the region where the two branches overlap is known as the

*turn-around region*. Fortunately, the bulk of the galaxies in our SDSS and AGES samples are relatively luminous and massive, and therefore overwhelmingly belong on the upper branch. We illustrate this point in Figure 8, where we plot  $[\text{N II}] \lambda 6584/\text{H}\alpha$  versus  $R_{23}$  for our (*left*) SDSS and (*right*) AGES star-forming galaxy samples. Objects that belong on the lower  $R_{23}$  branch generally have  $\log([\text{N II}]/\text{H}\alpha) < -1.1$ , while upper-branch galaxies have  $\log([\text{N II}]/\text{H}\alpha) > -1.1$  (McGaugh 1991; Contini et al. 2002; Kewley & Ellison 2008). We find that fewer than 1% of SDSS galaxies, and only  $\sim 3\%$  of AGES galaxies belong to the lower  $R_{23}$  branch. Of course, we do not have a measurement of  $[\text{N II}]/\text{H}\alpha$  for galaxies in AGES at  $z > 0.4$  because of the red wavelength cut-off of our spectra. However, we assume that all these galaxies lie on the upper  $R_{23}$  branch, which is not an unreasonable assumption given their luminosities and stellar masses (see Fig. 7). In particular, this assumption is conservative because it minimizes the amount of chemical evolution these objects would have to undergo to lie on the present-day  $\mathcal{M} - Z$  relation (see §6.1.1).

The second issue to consider is that both  $R_{23}$  and  $O_{32}$  are sensitive to dust attenuation. Unfortunately, we cannot correct for dust reddening because the Balmer decrement,  $\text{H}\alpha/\text{H}\beta$ , can be measured only for galaxies in AGES at  $z < 0.4$ , while the  $\text{H}\beta/\text{H}\gamma$  ratio is generally too noisy to give a reliable estimate of the reddening. Therefore, following Kobulnicky & Phillips (2003), we use EWs to estimate oxygen abundances. Besides being relatively insensitive to dust extinction as we show below, EWs have the added advantage of being impervious to flux-calibration issues (see §2.2.2).

With some simple assumptions it is easy to show that the EW-based  $R_{23}$  and  $O_{32}$  parameters are

$$\text{EW}(R_{23}) \equiv \frac{\alpha \text{EW}([\text{O II}]) + \text{EW}([\text{O III}])}{\text{EW}(\text{H}\beta)}, \quad (7)$$

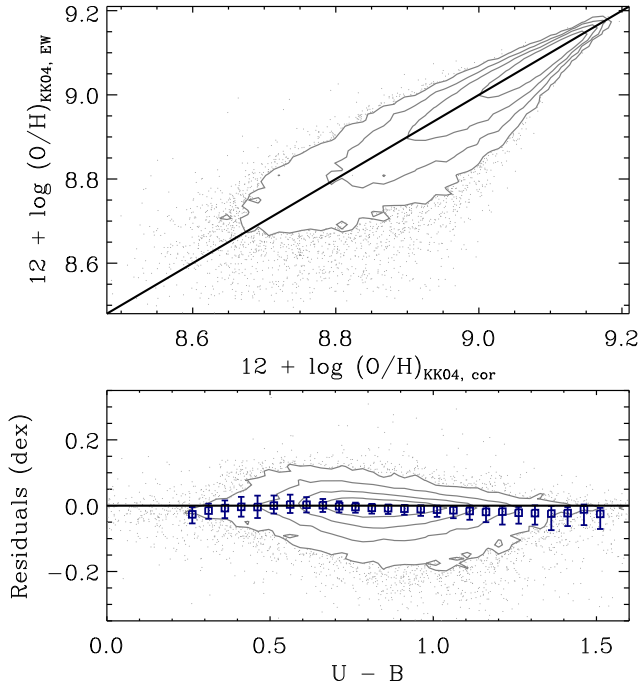


FIG. 9.— (*Top*) Correlation between oxygen abundances estimated using reddening-corrected fluxes and oxygen abundances derived using EWs and  $\alpha = 1.0$  (see §5.2). This comparison uses the KK04 abundance calibration, but the same conclusion holds if we use either the M91 or T04 calibrations. (*Bottom*) Abundance residuals vs. rest-frame  $U - B$  color. The open squares give the median residual metallicity in 0.05 mag wide bins of  $U - B$  color and the error bars indicate the interquartile range. The median residuals vary by  $< 0.05$  dex with a scatter of just 0.01–0.06 dex; therefore, abundances derived using EWs provide a reliable way of estimating the metallicity when reddening-corrected fluxes are unavailable. For reference, the contours in both panels enclose 50%, 75%, 90%, and 97.5% of the sample, and the solid line shows the one-to-one relation; the small grey points are individual galaxies lying outside the 97.5% contour level.

and

$$\text{EW}(O_{32}) \equiv \frac{\text{EW}([\text{O III}])}{\alpha \text{EW}([\text{O II}])}, \quad (8)$$

where

$$\alpha = \frac{I_c(4934)}{I_c(3727)} 10^{0.4\Delta E(B-V)[k(4934)-k(3727)]} \quad (9)$$

is a constant for each galaxy that depends on its recent star-formation history and level of dust attenuation. In equation (9),  $I_c(4934)$  and  $I_c(3727)$  are the intrinsic (unattenuated) flux of the stellar continuum at  $\lambda = 4934 \text{ \AA}$  (the wavelength midway between  $\text{H}\beta$  and  $[\text{O III}] \lambda 5007$ ) and  $3727 \text{ \AA}$ , respectively;  $\Delta E(B - V)$  is the reddening difference between the ionized gas and the continuum (in general,  $\Delta E(B - V) \geq 0$ ; Calzetti et al. 1994; Calzetti 2001); and  $k(4934)$  and  $k(3727)$  is the value of the assumed attenuation law at  $4934 \text{ \AA}$  and  $3727 \text{ \AA}$ , respectively (Kobulnicky & Phillips 2003). Using population synthesis models and some basic assumptions about  $\Delta E(B - V)$  and  $k(\lambda)$ , Kobulnicky & Phillips (2003) estimate  $\alpha = 0.84 \pm 0.3$ .

We obtain an independent, empirical estimate of  $\alpha$  by correlating the reddening-corrected  $O_{32}$  ratio,  $(O_{32})_{\text{cor}}$ , and  $\text{EW}(O_{32})$  using our SDSS sample. First, we estimate the nebular reddening for each galaxy using the observed Balmer decrement and assume an intrinsic  $\text{H}\alpha/\text{H}\beta$  ratio of 2.86. Next, we derive  $(O_{32})_{\text{cor}}$  using the O’Donnell (1994) Milky Way extinction curve and  $R_V = 3.1$  (Moustakas et al. 2006; Kennicutt et al. 2009). Equating  $\text{EW}(O_{32})$  and  $(O_{32})_{\text{cor}}$ , we find, on average,  $\alpha = 1.0 \pm 0.16$ . To a very good approximation, in other words, equations (7) and (8) with  $\alpha \approx 1$  reduce to equations (5) and (6) but with EWs in place of reddening-corrected fluxes.

In Figure 9 we compare the EW-based abundances against the abundances derived using reddening-corrected fluxes. For this comparison we use the KK04 calibration, although we reach identical conclusions using either the T04 or M91 calibration. In the bottom panel of Figure 9 we correlate the abundance residuals against the rest-frame  $U - B$  color. We find an excellent correlation between the two abundances, with a negligible systematic difference ( $< 0.05$  dex) and a  $1\sigma$  scatter that ranges from 0.01–0.03 dex at high metallicity, to 0.04–0.06 dex for more metal-poor galaxies, independent of the adopted abundance calibration. Therefore, we conclude that EWs (assuming  $\alpha = 1$ ) provide an effective means of estimating the gas-phase abundances of galaxies in the absence of a measurement of the Balmer decrement (but for an alternative conclusion see Liang et al. 2007). In §6.1.3 we further show that using EWs in place of reddening-corrected fluxes has a negligible effect on the inferred shape and normalization of the  $\mathcal{M} - Z$  and  $L - Z$  relations.

### 5.3. From Equivalent Widths to Metallicity

Given the measured values of  $\text{EW}(R_{23})$  and  $\text{EW}(O_{32})$ , and the inferred or assumed  $R_{23}$  branch, we derive the gas-phase oxygen abundances of all the star-forming galaxies in our SDSS and AGES samples using the M91, KK04, and T04 strong-line calibrations (see Appendix A). To derive the uncertainty in  $12 + \log(\text{O}/\text{H})$ , we apply the Monte Carlo-based method developed by Moustakas et al. (2010), which uses the statistical uncertainties on  $\text{EW}([\text{O II}])$ ,  $\text{EW}([\text{O III}])$  and  $\text{EW}(\text{H}\beta)$  to obtain a realistic estimate of the abundance error for each object. This algorithm also relies on quantitative criteria to identify galaxies that lie *off* the adopted abundance calibration, typically because they have  $R_{23} \gtrsim 10$  (see Fig A1). The final number of AGES and SDSS galaxies with well-measured oxygen abundances is  $\sim 3000$  and  $\sim 75,000$ , respectively, where the exact number depends on which strong-line calibration is being used (see Table 1).

## 6. ANALYSIS

Armed with stellar masses, optical luminosities, and gas-phase oxygen abundances for both our SDSS and AGES samples, we now proceed to study the change in the chemical abundances of star-forming galaxies since  $z = 0.75$ . Although we focus our analysis on the evolution of the  $\mathcal{M} - Z$  relation, we also examine the evolution of the  $B$ -band  $L - Z$  relation. In §6.1 we establish the  $\mathcal{M} - Z$  and  $L - Z$  relations at  $z \sim 0.1$  using our SDSS

TABLE 3  
 SDSS  $\mathcal{M} - Z$  AND  $L - Z$  RELATIONS

Calibration <sup>a</sup>	$\mathcal{M} - Z^b$				$L - Z^c$		
	$12 + \log(\text{O}/\text{H})^*$	$\log(\mathcal{M}^*/10^9 M_\odot)$	$\gamma$	$\sigma^d$	$c_0$	$c_1$	$\sigma^d$
Reddening-Corrected Fluxes <sup>a</sup>							
KK04	9.115	2.043	1.41	0.07	9.066	-0.231	0.16
M91	9.004	3.117	1.27	0.09	8.919	-0.256	0.18
T04	9.098	3.475	1.22	0.10	9.014	-0.291	0.20
MPA-JHU	9.137	3.436	0.89	0.09	9.026	-0.248	0.16
Equivalent Widths <sup>a</sup>							
KK04	9.108	2.001	1.25	0.07	9.054	-0.229	0.16
M91	9.006	3.151	1.06	0.09	8.903	-0.248	0.17
T04	9.097	3.575	1.05	0.10	8.997	-0.286	0.20

<sup>a</sup> Results derived using the Kobulnicky & Kewley (2004, KK04), McGaugh (1991, M91), and Tremonti et al. (2004, T04) calibrations of the  $R_{23}$  parameter, using both reddening-corrected line-fluxes and equivalent widths (see §5.2 for details). For comparison, we also derive the  $\mathcal{M} - Z$  and  $L - Z$  relations using the oxygen abundances published by the MPA-JHU team (see §6.1.1).

<sup>b</sup>  $\mathcal{M} - Z$  relation given by  $12 + \log(\text{O}/\text{H}) = 12 + \log(\text{O}/\text{H})^* - \log[1 + (\mathcal{M}^*/10^9 M_\odot)^\gamma]$ .

<sup>c</sup>  $B$ -band  $L - Z$  relation given by  $12 + \log(\text{O}/\text{H}) = c_0 + c_1(M_B + 20.5)$ .

<sup>d</sup> Residual  $1\sigma$  scatter about the best-fitting relation in dex.

sample, and in §6.2, we use AGES to measure their evolution from  $z = 0.05 - 0.75$ . We conclude in §6.3 by comparing our results with previous determinations of the  $\mathcal{M} - Z$  relation at intermediate redshift.

### 6.1. SDSS $\mathcal{M} - Z$ and $B$ -Band $L - Z$ Relations

We begin by determining the  $\mathcal{M} - Z$  relation for star-forming galaxies at  $z \sim 0.1$  in §6.1.1, and the  $L - Z$  relation in §6.1.2. In particular, we examine the effect of adopting a specific abundance calibration on the results. In both sections we derive metallicities using the reddening-corrected emission-line fluxes (see §5.2), although in §6.1.3 we examine the effect of using EWs on our results.

#### 6.1.1. $\mathcal{M} - Z$ Relation at $z \sim 0.1$

In Figure 10 we plot the SDSS  $\mathcal{M} - Z$  relation using four different abundance calibrations. The first three panels show the  $\mathcal{M} - Z$  relations based on the KK04, M91, and T04 abundance calibrations, and the lower-right panel shows, for comparison, the  $\mathcal{M} - Z$  relation using the oxygen abundances derived by the MPA-JHU team.<sup>30</sup> The MPA-JHU abundances are based on fitting the Charlot & Longhetti (2001) photoionization models to *all* the available nebular emission lines, and therefore they serve as a useful cross-check of the  $R_{23}$ -based abundances. We point out that the T04 calibration of  $R_{23}$  by Tremonti et al. (2004) was derived by correlating  $R_{23}$  against the MPA-JHU metallicities; therefore, the statistical agreement between the T04 and MPA-JHU  $\mathcal{M} - Z$  relations is not unexpected.

We characterize the shape of the  $\mathcal{M} - Z$  relation by computing the weighted mean metallicity in 0.05 dex wide bins of stellar mass, and plot the results in Figure 10 using red circles, blue squares, green triangles, and black diamonds for each of the four calibrations, as indicated in the figure. To fit the  $\mathcal{M} - Z$  relation we adopt the following functional form:

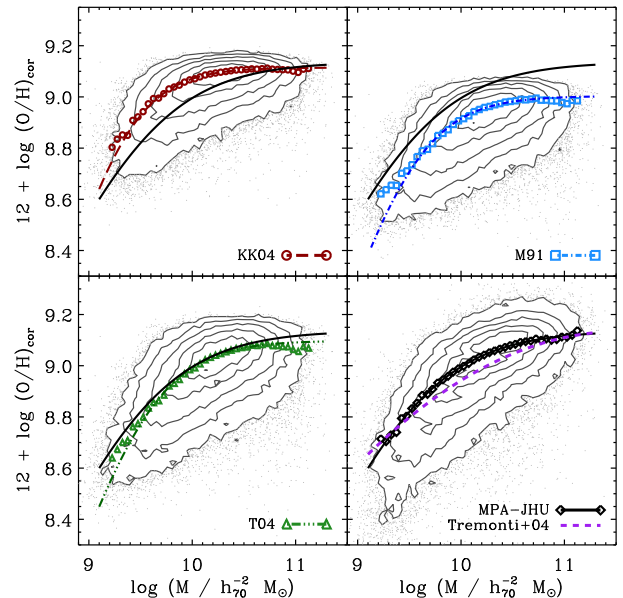


FIG. 10.— SDSS  $\mathcal{M} - Z$  relation based on four different methods of deriving oxygen abundances from the reddening-corrected line-fluxes. The first three panels show the  $\mathcal{M} - Z$  relation based on the three  $R_{23}$ -based strong-line calibrations adopted in this paper (KK04, M91, and T04), while the  $\mathcal{M} - Z$  relation in the lower-right panel shows the metallicities for SDSS/DR7 galaxies derived by the MPA-JHU team (see §6.1.1). The contours enclose 25%, 50%, 75%, 90%, and 97.5% of the sample, and the small grey points are individual galaxies that lie outside the 97.5% contour level. The symbols in each panel (as indicated in the legend) show the weighted mean metallicity in 0.05-dex wide bins of stellar mass, and the corresponding curves show the best-fitting  $\mathcal{M} - Z$  relation given by equation (10). For reference, we reproduce in each panel the MPA-JHU  $\mathcal{M} - Z$  relation (*solid black curve*). In the lower-right panel we also show for comparison the original SDSS  $\mathcal{M} - Z$  relation (based on the SDSS/DR4) published by Tremonti et al. (2004) (*dashed purple curve*). This figure demonstrates that both the normalization and the shape of the  $\mathcal{M} - Z$  relation depend on the method used to derive oxygen abundances.

<sup>30</sup> <http://www.mpa-garching.mpg.de/SDSS/DR7>



$$12 + \log(\text{O}/\text{H}) = 12 + \log(\text{O}/\text{H})^* - \log \left[ 1 + \left( \frac{\mathcal{M}^*}{10^9 \mathcal{M}_\odot} \right)^\gamma \right], \quad (10)$$

where  $12 + \log(\text{O}/\text{H})^*$  and  $\mathcal{M}^*$  are the characteristic metallicity and stellar mass, respectively. We discuss and justify this particular parameterization of the  $\mathcal{M} - Z$  relation compared to the more commonly used polynomial model in Appendix B. We show the best-fitting KK04, M91, T04, and MPA-JHU  $\mathcal{M} - Z$  relations in Figure 10 using long-dashed, dot-dashed, triple-dot-dashed, and solid lines, respectively, and list the best-fitting coefficients in Table 3. Note that the formal statistical uncertainties on the coefficients are negligible ( $< 0.01$  dex), and therefore have not been tabulated. For reference, we reproduce the MPA-JHU  $\mathcal{M} - Z$  relation in every panel of Figure 10. In addition, in the lower-right panel we show the  $\mathcal{M} - Z$  relation derived by Tremonti et al. (2004) from a sample of  $\sim 53,000$  galaxies from the SDSS Data Release 4 (DR4) as a short-dashed purple line. The origin of the discrepancy between the  $\mathcal{M} - Z$  relation published by Tremonti et al. (2004) using DR4 and the MPA-JHU  $\mathcal{M} - Z$  relation we derive using DR7 is not clear, given that the metallicities were derived using the same maximum likelihood technique and Charlot & Longhetti (2001) photoionization models. Nevertheless, evolutionary studies and theoretical models that are calibrated against the original Tremonti et al. (2004)  $\mathcal{M} - Z$  relation should bear these differences in mind.

Returning to Figure 10, we find that all four abundance calibrations yield a tight, well-defined  $\mathcal{M} - Z$  relation—the  $1\sigma$  scatter ranges from 0.07–0.10 dex—that increases monotonically with stellar mass and then flattens by varying amounts above a characteristic mass around  $\sim 10^{10} \mathcal{M}_\odot$ . However, both the normalization and shape of the  $\mathcal{M} - Z$  relation vary significantly among the different calibrations, a result that has been explored in detail by Kewley & Ellison (2008). For example, the KK04  $\mathcal{M} - Z$  relation is much flatter ( $\gamma$  is larger), and the characteristic mass is a factor of  $\sim 1.6$  smaller compared to the other three  $\mathcal{M} - Z$  relations, although the characteristic metallicities of the four  $\mathcal{M} - Z$  relations are within  $\sim 0.1$  dex (25%) of one another.

Understanding the origin of the differences between the  $\mathcal{M} - Z$  relations implied by these strong-line calibrations is beyond the scope of this paper (but see the discussion in Moustakas et al. 2010). The main points to take away from the preceding discussion and Figure 10 are that both the normalization *and* shape of the  $\mathcal{M} - Z$  relation depend on the method used to derive gas-phase abundances. This result has important implications for theoretical semianalytic and hydrodynamic models of galaxy formation that use the  $\mathcal{M} - Z$  relation to calibrate and tune so-called “recipes” for star formation efficiency, supernova feedback, and galactic winds (e.g., Brooks et al. 2007; Finlator & Davé 2008; Dutton & van den Bosch 2009; Davé et al. 2011b). From an observational standpoint, these results emphasize the importance of focusing on the *differential* metallicity evolution, and of considering multiple abundance diagnostics to ascertain whether the *rate* of metallicity evolution depends on the adopted abundance calibration (see especially §6.2.1), an issue

that heretofore has largely been ignored.

We conclude this section by verifying that the  $\mathcal{M} - Z$  relations measured from our SDSS sample at  $z \sim 0.1$  and the subset of AGES galaxies in our lowest redshift bin,  $0.05 < z < 0.20$  (hereafter, the low-redshift AGES sample), are consistent. In Figure 11 we plot the KK04-based  $\mathcal{M} - Z$  relations for these two samples. We emphasize that the M91 and T04 abundance calibrations yield identical conclusions. The red squares and blue circles show the median metallicity in 0.05 and 0.15 dex wide bins of stellar mass for our SDSS and low-redshift AGES sample, respectively. The error bars on the AGES points reflect the standard error of the mean metallicity in each stellar mass bin (the SDSS error bars are generally smaller than the symbols).

Examining Figure 11, we find that the two  $\mathcal{M} - Z$  relations are statistically consistent with one another. This figure also strikingly demonstrates that the SDSS sample is crucial for constraining the massive end of the  $\mathcal{M} - Z$  relation; our low-redshift AGES sample simply contains too few massive, metal-rich galaxies due to the limited cosmological volume probed by the survey. Moreover, the consistency of the two  $\mathcal{M} - Z$  relations suggests that the relative aperture bias between the two surveys is negligible, even though the fibers used by AGES are a factor of two smaller (see also the detailed discussion of aperture effects in §7.4). Therefore, we conclude that our SDSS sample provides an unbiased sample for measuring the evolution of the  $\mathcal{M} - Z$  relation at intermediate redshift from AGES.

### 6.1.2. *B*-band $L - Z$ Relation at $z \sim 0.1$

We turn our attention next to measuring the *B*-band  $L - Z$  relation at  $z \sim 0.1$  using our SDSS sample. Although the optical  $L - Z$  relation is considerably more sensitive to variations in star formation history (age or mass-to-light ratio, recent bursts of star formation, etc.) and dust attenuation than the  $\mathcal{M} - Z$  relation (e.g., Lee et al. 2004; Salzer et al. 2005), many previous studies of the nebular abundances of star-forming galaxies at both low and high redshift have investigated the *B*-band  $L - Z$  relation as a proxy for the  $\mathcal{M} - Z$  relation. However, we will see in §6.2.2 that the optical  $L - Z$  relation is an ineffective means of quantifying the chemical evolution of star-forming galaxies due to its greater sensitivity to the effects of *luminosity* evolution.

In Figure 12 we show the *B*-band  $L - Z$  relations from the SDSS based on the same four abundance calibrations presented in Figure 10. As has been known for nearly three decades (see §1), star-forming galaxies exhibit a strong correlation between optical luminosity and gas-phase abundance; however, the  $L - Z$  relation is clearly sensitive to the adopted abundance calibration, among other factors. To quantify the observed differences we defer to historical precedent and model the  $L - Z$  relation using a simple linear model, given by

$$12 + \log(\text{O}/\text{H}) = c_0 + c_1(M_B + 20.5), \quad (11)$$

where  $c_0$  is the metallicity at  $M_B = -20.5$  and  $c_1$  is the slope in dex mag<sup>-1</sup>. We solve equation (11) using an ordinary least-squares bisector fit, which is appropriate when the scatter in the observed correlation is larger than the measurement error in either axis (Isobe et al.

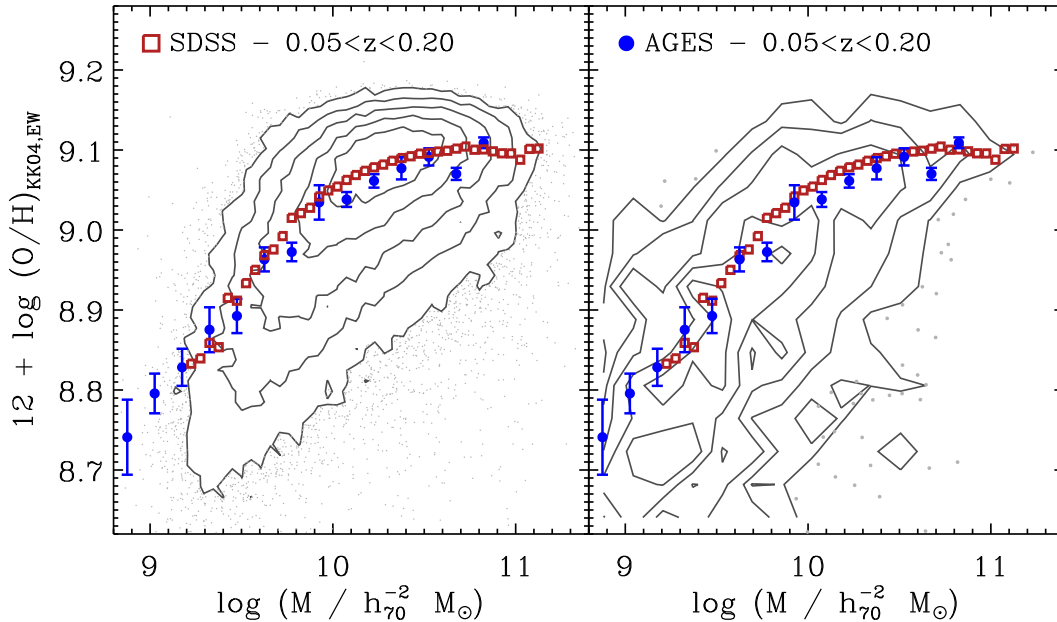


FIG. 11.—  $\mathcal{M} - Z$  relation at  $z \sim 0.1$  based on our (left) SDSS and (right) low-redshift ( $0.05 < z < 0.20$ ) AGES samples. In both panels the contours enclose 25%, 50%, 75%, 90%, and 97.5% of the sample, and the small grey points are individual galaxies that lie outside the 97.5% contour level. The open red squares and filled blue points represent the median metallicity in 0.05 and 0.15 dex wide bins of stellar mass for the SDSS and AGES, respectively, and the error bars on the AGES points are the standard error in the mean metallicity in each stellar mass bin. Where they overlap, the  $\mathcal{M} - Z$  relations of the two samples are statistically consistent with one another. Note however, the relative paucity of massive, metal-rich galaxies in AGES over this redshift range, due to the relatively small amount of cosmological volume probed.

1990). We show the best-fitting  $L - Z$  relations in Figure 12 based on the KK04, M91, T04, and MPA-JHU metallicities as long-dashed red, dot-dashed blue, triple-dot-dashed green, and solid black lines, respectively, and list the best-fitting coefficients in Table 3. Again, the statistical uncertainties on the coefficients are negligible given the sample size and have not been tabulated. For comparison, we also show in the lower-right panel as a short-dashed purple line the  $B$ -band  $L - Z$  relation determined by Tremonti et al. (2004) using the MPA-JHU abundances of  $\sim 53,000$  galaxies from the SDSS/DR4.

We find that the slope of the  $B$ -band  $L - Z$  relation we derive ranges from  $-0.231$  dex  $\text{mag}^{-1}$  when using the KK04 calibration, to  $-0.291$  dex  $\text{mag}^{-1}$  based on the T04 abundance calibration. Tremonti et al. (2004), on the other hand, inferred a  $L - Z$  slope of  $-0.185$  dex  $\text{mag}^{-1}$  using a sample that extended to much fainter luminosities. Other studies studying both low-luminosity dwarfs and massive disk galaxies have obtained slopes ranging from  $-0.130$  dex  $\text{mag}^{-1}$  to  $-0.280$  dex  $\text{mag}^{-1}$  (e.g., Skillman et al. 1989; Lee et al. 2004; Lamareille et al. 2004; Salzer et al. 2005; Moustakas et al. 2010). We conclude, therefore, that the slope of the  $L - Z$  relation is sensitive to both the adopted abundance calibration, and the range of luminosities spanned by the parent sample. Finally, we note that for a given abundance calibration, the  $1\sigma$  scatter in the  $B$ -band  $L - Z$  relation is roughly a factor of two larger than the scatter in the corresponding  $\mathcal{M} - Z$  relation.

### 6.1.3. Effect of Using $\text{EW}(R_{23})$ on the Local $\mathcal{M} - Z$ and $L - Z$ Relations

The preceding analysis has all been based on abundances derived from reddening-corrected fluxes; however, to measure the evolution of the  $\mathcal{M} - Z$  relation from AGES (see §6.2) we must rely on oxygen abundances derived from emission-line EWs (see §5.2). Therefore, in Table 3 we also list the coefficients of the SDSS  $\mathcal{M} - Z$  and  $L - Z$  relations using our EW-based abundances. With respect to the  $\mathcal{M} - Z$  relations derived using reddening-corrected fluxes, we find that the EW-based  $\mathcal{M} - Z$  relations are slightly steeper ( $\gamma$  is smaller by 15% – 20%), but that the characteristic stellar masses and characteristic metallicities agree to within  $\lesssim 0.01$  dex. These differences translate into maximum metallicity differences of  $\sim 0.02$  dex around  $\sim 10^{9.8} M_{\odot}$ , and  $\lesssim 0.01$  dex around  $10^{11} M_{\odot}$ . Similarly, the  $L - Z$  relations derived using either reddening-corrected fluxes or EWs have nearly identical slopes and zeropoints. Therefore, we conclude that using EWs to measure the evolution of the  $\mathcal{M} - Z$  relation should not bias our conclusions.

## 6.2. Evolution of the $\mathcal{M} - Z$ and $B$ -Band $L - Z$ Relations Since $z = 0.75$

Building on our measurement of the local  $\mathcal{M} - Z$  and  $L - Z$  relations in the previous section, we now use AGES to measure their evolution since  $z = 0.75$ .

### 6.2.1. Evolution of the $\mathcal{M} - Z$ Relation

In Figure 13 we plot the  $\mathcal{M} - Z$  relation from AGES in six redshift bins centered on  $z = 0.1, 0.2, 0.3, 0.4, 0.5,$  and  $0.65$  (see also Fig. 7). Here we only show results using the KK04 abundance calibration, although below

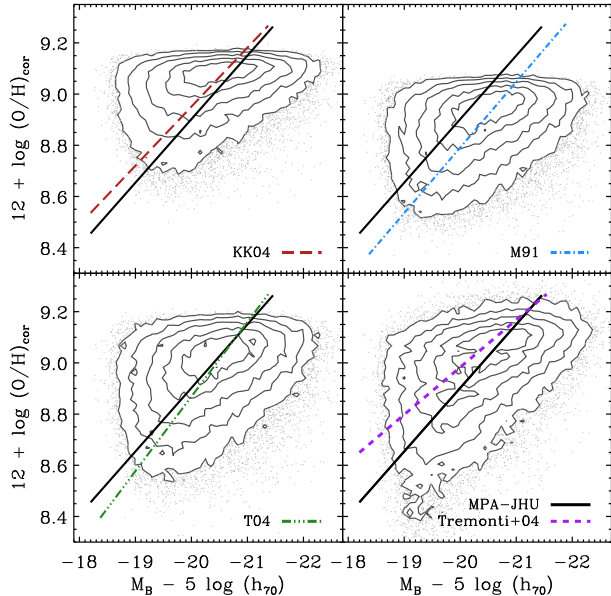


FIG. 12.—  $B$ -band  $L - Z$  relation from the SDSS based on four different abundance calibrations. The contours enclose 25%, 50%, 75%, 90%, and 97.5% of the sample, and the small grey points represent galaxies lying outside the 97.5% contour level. The dashed red, dot-dashed blue, triple-dot-dashed green, and solid black lines represent the ordinary least-squares bisector fits to the KK04, M91, T04, and MPA-JHU  $L - Z$  relations, respectively. We reproduce the MPA-JHU  $L - Z$  relation in each panel for reference, and in the lower-right panel we also show the  $L - Z$  relation derived by Tremonti et al. (2004) as a short-dashed purple line. The best-fitting slopes range from  $-0.231 \text{ dex mag}^{-1}$  to  $-0.291 \text{ dex mag}^{-1}$  (see Table 3), demonstrating that the choice of abundance calibration can have a significant effect on the inferred  $L - Z$  relation. The large difference in slope with respect to Tremonti et al. (2004), whose sample extended to lower absolute magnitudes, also demonstrates that the  $L - Z$  relation is sensitive to the range of luminosities spanned by the sample.

we explicitly explore how the choice of abundance calibration affects the amount of inferred evolution. For reference, we overplot the local  $\mathcal{M} - Z$  relation from the SDSS in every panel as a solid black curve (see Table 3). To quantify the observed evolution we compute the weighted mean metallicity in 0.2 dex wide bins of stellar mass, requiring a minimum of 10 galaxies with well-measured abundances in each bin. We weight each galaxy  $i$  by  $\sigma_{\text{eff},i}^{-2}$ , the effective inverse variance, given by

$$\sigma_{\text{eff},i}^{-2} \equiv w_i \sigma_{\log(\text{O}/\text{H})_i}^{-2}, \quad (12)$$

where  $w_i$  is that object’s statistical weight (see §2.2.1), and  $\sigma_{\log(\text{O}/\text{H})_i}$  is the statistical uncertainty on the metallicity (see §5.3). We list the measured mean metallicities in Table 4, and plot the results in Figure 13 using filled (open) red points for stellar masses above (below) our completeness limit (see §4.3). Examining Figure 13, we find a well-defined  $\mathcal{M} - Z$  relation that changes remarkably little over this redshift range. Nevertheless, at fixed stellar mass the mean metallicity of galaxies clearly decreases with increasing redshift, although it is not yet clear whether the observed evolution varies with mass.

We note in passing that the *distribution* of oxygen abundance at fixed stellar mass also appears to vary with

redshift. For example, in the two highest redshift bins we see a tail of massive galaxies with lower-than-average oxygen abundances,  $12 + \log(\text{O}/\text{H}) \approx 8.8 - 9$ , that are not present at lower redshift. We find a comparable number of objects based on both the T04 and M91 abundance calibrations. These objects may be similar to the population of “metal-poor” galaxies reported by Lilly et al. (2003) and Maier et al. (2005). However, we defer a more detailed analysis of this population of objects, and of the full metallicity distributions to a future paper, and focus instead on the evolution of the mean metallicity with redshift.

To investigate the trends seen in Figure 13 in more detail, in Figure 14 we show the mean metallicity  $\langle 12 + \log(\text{O}/\text{H}) \rangle$  versus redshift for both our SDSS and AGES samples in eight bins of stellar mass spanning  $10^{9.5} - 10^{11.1} \mathcal{M}_{\odot}$ . We show results based on the KK04, T04, and M91 calibrations using red points, green triangles, and blue squares, respectively, and render stellar mass bins above and below our completeness limit using filled and open symbols. We model the observed evolution, separately for each calibration and stellar mass interval, as a linear function of redshift given by

$$\langle 12 + \log(\text{O}/\text{H}) \rangle = \langle 12 + \log(\text{O}/\text{H}) \rangle_{z=0.1} + \frac{d[\log(\text{O}/\text{H})]}{dz} (z - 0.1), \quad (13)$$

where  $\langle 12 + \log(\text{O}/\text{H}) \rangle_{z=0.1}$  is the mean metallicity at  $z = 0.1$  and  $d[\log(\text{O}/\text{H})]/dz$  is the logarithmic rate of metallicity evolution. We tabulate the best-fitting linear coefficients in Table 5.

Figure 14 conveys several interesting results. First, we find that the KK04, T04, and M91 abundance calibrations yield mean metallicities that differ in an absolute sense by significant amounts (no vertical offsets have been applied to the measurements). On average, the KK04-based metallicities are 0.093 dex (24%) and 0.16 dex (45%) higher than the metallicities derived using the T04 and M91 calibration, respectively. These systematic differences likely originate from the different assumptions and ingredients underlying the photoionization models used to calibrate these strong-line methods (e.g., Kewley & Dopita 2002). Understanding the origin of these discrepancies is beyond the scope of this paper, although these results highlight that even within the class of theoretical abundance calibrations there are non-negligible systematic differences (see, e.g., the discussion in Moustakas et al. 2010).

Despite the significant differences in the *absolute* abundances of the galaxies in our sample, all three calibrations reveal that star-forming galaxies of a given stellar mass become increasingly more metal poor with increasing redshift. The *rate* of metallicity evolution, however, clearly depends on the adopted abundance calibration (see Table 5). Specifically, we find that  $d[\log(\text{O}/\text{H})]/dz$  based on the KK04 calibration is systematically shallower (by a factor of  $\sim 1.7$  at  $> 3\sigma$  significance) than the slopes measured using the other two calibrations. We attribute this difference to the relatively flat  $\mathcal{M} - Z$  relation for massive galaxies implied by the KK04 calibration (see Fig. 10, top-left panel), which has the effect of reducing the rate of metallicity evolution we measure compared to the other two calibrations. From these data



TABLE 4  
 MEAN OXYGEN ABUNDANCE IN BINS OF STELLAR MASS AND REDSHIFT<sup>a</sup>

Redshift Range	$N^b$	$\langle z \rangle^c$	$\langle \log(\mathcal{M}/\mathcal{M}_\odot) \rangle^d$	$\langle 12 + \log(\text{O}/\text{H})_{\text{KK04}} \rangle$	$\langle 12 + \log(\text{O}/\text{H})_{\text{M91}} \rangle$	$\langle 12 + \log(\text{O}/\text{H})_{\text{T04}} \rangle$
$10.9 < \log(\mathcal{M}/\mathcal{M}_\odot) < 11.1$						
0.05 – 0.20	1217	0.14	10.98	$9.095 \pm 0.010$	$8.975 \pm 0.010$	$9.055 \pm 0.010$
0.15 – 0.25	15	0.20	10.97	$9.099 \pm 0.010$	$8.964 \pm 0.015$	$9.057 \pm 0.020$
0.25 – 0.35	27	0.32	10.97	$9.055 \pm 0.018$	$8.896 \pm 0.027$	$8.976 \pm 0.029$
0.35 – 0.45	41	0.39	10.99	$9.067 \pm 0.010$	$8.923 \pm 0.015$	$8.997 \pm 0.019$
0.45 – 0.55	18	0.50	11.01	$9.039 \pm 0.010$	$8.891 \pm 0.013$	$8.965 \pm 0.016$
0.55 – 0.75	16	0.62	10.97	$9.032 \pm 0.021$	$8.884 \pm 0.033$	$8.952 \pm 0.031$
$10.7 < \log(\mathcal{M}/\mathcal{M}_\odot) < 10.9$						
0.05 – 0.20	4070	0.12	10.78	$9.102 \pm 0.010$	$8.985 \pm 0.010$	$9.073 \pm 0.010$
0.05 – 0.15	16	0.12	10.78	$9.106 \pm 0.010$	$8.977 \pm 0.016$	$9.072 \pm 0.019$
0.15 – 0.25	35	0.22	10.80	$9.074 \pm 0.010$	$8.933 \pm 0.013$	$9.015 \pm 0.015$
0.25 – 0.35	65	0.31	10.78	$9.077 \pm 0.010$	$8.945 \pm 0.016$	$9.025 \pm 0.018$
0.35 – 0.45	64	0.39	10.79	$9.065 \pm 0.010$	$8.921 \pm 0.015$	$9.004 \pm 0.015$
0.45 – 0.55	32	0.51	10.79	$9.039 \pm 0.010$	$8.880 \pm 0.012$	$8.963 \pm 0.014$
0.55 – 0.75	20	0.61	10.78	$9.058 \pm 0.015$	$8.913 \pm 0.021$	$8.968 \pm 0.040$
$10.5 < \log(\mathcal{M}/\mathcal{M}_\odot) < 10.7$						
0.05 – 0.20	8760	0.11	10.59	$9.098 \pm 0.010$	$8.980 \pm 0.010$	$9.067 \pm 0.010$
0.05 – 0.15	19	0.12	10.58	$9.104 \pm 0.017$	$8.982 \pm 0.022$	$9.068 \pm 0.030$
0.15 – 0.25	75	0.20	10.58	$9.076 \pm 0.010$	$8.938 \pm 0.017$	$9.019 \pm 0.018$
0.25 – 0.35	84	0.31	10.60	$9.061 \pm 0.010$	$8.910 \pm 0.013$	$8.994 \pm 0.013$
0.35 – 0.45	80	0.39	10.59	$9.058 \pm 0.010$	$8.909 \pm 0.011$	$8.990 \pm 0.012$
0.45 – 0.55	31	0.50	10.61	$9.047 \pm 0.013$	$8.898 \pm 0.020$	$8.968 \pm 0.018$
0.55 – 0.75	14	0.60	10.63	$9.044 \pm 0.021$	$8.885 \pm 0.031$	$8.963 \pm 0.033$
$10.3 < \log(\mathcal{M}/\mathcal{M}_\odot) < 10.5$						
0.05 – 0.20	12679	0.10	10.40	$9.091 \pm 0.010$	$8.963 \pm 0.010$	$9.047 \pm 0.010$
0.05 – 0.15	37	0.12	10.39	$9.082 \pm 0.021$	$8.963 \pm 0.041$	$9.020 \pm 0.043$
0.15 – 0.25	120	0.20	10.39	$9.075 \pm 0.011$	$8.937 \pm 0.020$	$9.012 \pm 0.018$
0.25 – 0.35	114	0.30	10.39	$9.049 \pm 0.010$	$8.899 \pm 0.012$	$8.977 \pm 0.010$
0.35 – 0.45	93	0.39	10.39	$9.053 \pm 0.010$	$8.899 \pm 0.011$	$8.977 \pm 0.012$
0.45 – 0.55	28	0.50	10.39	$9.020 \pm 0.018$	$8.847 \pm 0.026$	$8.931 \pm 0.030$
$10.1 < \log(\mathcal{M}/\mathcal{M}_\odot) < 10.3$						
0.05 – 0.20	14559	0.08	10.20	$9.076 \pm 0.010$	$8.935 \pm 0.010$	$9.014 \pm 0.010$
0.05 – 0.15	44	0.11	10.20	$9.072 \pm 0.010$	$8.922 \pm 0.012$	$9.007 \pm 0.014$
0.15 – 0.25	161	0.21	10.19	$9.053 \pm 0.010$	$8.896 \pm 0.011$	$8.974 \pm 0.012$
0.25 – 0.35	100	0.30	10.19	$9.037 \pm 0.010$	$8.872 \pm 0.012$	$8.952 \pm 0.012$
0.35 – 0.45	65	0.39	10.20	$9.025 \pm 0.010$	$8.855 \pm 0.015$	$8.925 \pm 0.016$
0.45 – 0.55	12	0.50	10.22	$8.965 \pm 0.014$	$8.784 \pm 0.016$	$8.854 \pm 0.019$
$9.9 < \log(\mathcal{M}/\mathcal{M}_\odot) < 10.1$						
0.05 – 0.20	13523	0.08	10.00	$9.053 \pm 0.010$	$8.891 \pm 0.010$	$8.967 \pm 0.010$
0.05 – 0.15	93	0.12	9.99	$9.032 \pm 0.011$	$8.855 \pm 0.017$	$8.924 \pm 0.016$
0.15 – 0.25	151	0.21	10.00	$9.017 \pm 0.012$	$8.837 \pm 0.018$	$8.903 \pm 0.021$
0.25 – 0.35	76	0.30	9.99	$9.012 \pm 0.010$	$8.838 \pm 0.013$	$8.919 \pm 0.013$
0.35 – 0.45	37	0.38	9.99	$8.953 \pm 0.015$	$8.764 \pm 0.017$	$8.832 \pm 0.018$
$9.7 < \log(\mathcal{M}/\mathcal{M}_\odot) < 9.9$						
0.05 – 0.20	10378	0.07	9.81	$9.016 \pm 0.010$	$8.833 \pm 0.010$	$8.904 \pm 0.010$
0.05 – 0.15	105	0.12	9.80	$9.014 \pm 0.034$	$8.827 \pm 0.035$	$8.894 \pm 0.038$
0.15 – 0.25	162	0.20	9.80	$8.986 \pm 0.010$	$8.797 \pm 0.012$	$8.866 \pm 0.013$
0.25 – 0.35	63	0.29	9.81	$8.979 \pm 0.019$	$8.780 \pm 0.024$	$8.850 \pm 0.025$
0.35 – 0.45	15	0.37	9.82	$8.955 \pm 0.022$	$8.766 \pm 0.019$	$8.833 \pm 0.018$
$9.5 < \log(\mathcal{M}/\mathcal{M}_\odot) < 9.7$						
0.05 – 0.20	6474	0.06	9.61	$8.961 \pm 0.010$	$8.763 \pm 0.010$	$8.828 \pm 0.010$
0.05 – 0.15	107	0.12	9.60	$8.958 \pm 0.020$	$8.764 \pm 0.022$	$8.829 \pm 0.026$
0.15 – 0.25	118	0.20	9.59	$8.931 \pm 0.015$	$8.736 \pm 0.014$	$8.804 \pm 0.018$
0.25 – 0.35	33	0.28	9.62	$8.880 \pm 0.020$	$8.691 \pm 0.020$	$8.747 \pm 0.023$

<sup>a</sup> Mean metallicity of galaxies in multiple bins of stellar mass and redshift, based on the KK04, M91, and T04 calibrations. Note that the metallicities in the first row of each stellar mass interval correspond to our SDSS sample, while the metallicities in the other rows are based on our AGES sample.

<sup>b</sup> Mean number of galaxies in this redshift interval and stellar mass bin. Note that the number of objects varies slightly depending on the abundance calibration (see, e.g., Table 1), so we show here the average number. We only provide redshift and stellar mass bins with at least ten galaxies.

<sup>c</sup> Mean redshift of the galaxies in this subsample.

<sup>d</sup> Mean stellar mass of the galaxies in this subsample.

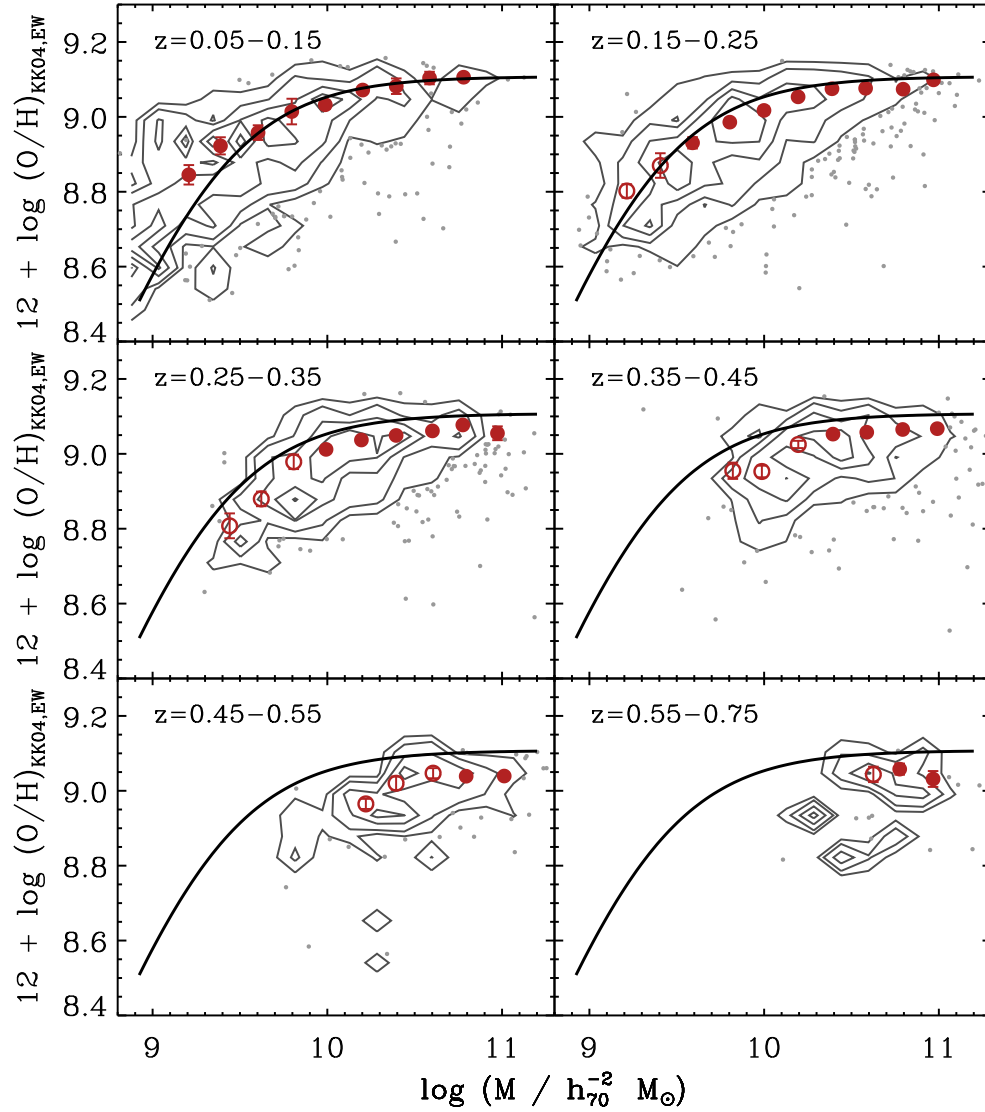


FIG. 13.— AGES  $\mathcal{M} - Z$  relation at  $z = 0.05 - 0.75$  based on the KK04 abundance calibration. For reference, the contours enclose 25%, 50%, 75%, and 90% of the galaxies in each redshift interval, and the small grey points represent individual galaxies that lie outside the 90% contour level. The filled (open) points show the weighted mean metallicity in 0.2 dex wide bins of stellar mass for galaxies above (below) our completeness limit (see §4.3). The solid black curve, reproduced in every panel for reference, is the local  $\mathcal{M} - Z$  relation from the SDSS (see §6.1.1). We find that galaxies experience relatively little chemical evolution over this redshift range. Note that the T04 and M91 abundance calibrations yield similar results.

TABLE 5  
 LINEAR EVOLUTION OF THE MEAN METALLICITY OF GALAXIES AT  $z = 0.05 - 0.75^a$ 

Calibration	$\langle 12 + \log(\text{O}/\text{H}) \rangle_{z=0.1}$ (dex)	$d[\log(\text{O}/\text{H})]/dz$ (dex $z^{-1}$ )	$\langle 12 + \log(\text{O}/\text{H}) \rangle_{z=0.1}$ (dex)	$d[\log(\text{O}/\text{H})]/dz$ (dex $z^{-1}$ )
	$10.9 < \log(\mathcal{M}/\mathcal{M}_\odot) < 11.1$		$10.7 < \log(\mathcal{M}/\mathcal{M}_\odot) < 10.9$	
KK04	$9.101 \pm 0.01$	$-0.139 \pm 0.018$	$9.104 \pm 0.01$	$-0.140 \pm 0.015$
M91	$8.983 \pm 0.01$	$-0.224 \pm 0.029$	$8.990 \pm 0.01$	$-0.236 \pm 0.023$
T04	$9.064 \pm 0.01$	$-0.244 \pm 0.034$	$9.079 \pm 0.01$	$-0.276 \pm 0.028$
	$10.5 < \log(\mathcal{M}/\mathcal{M}_\odot) < 10.7$		$10.3 < \log(\mathcal{M}/\mathcal{M}_\odot) < 10.5$	
KK04	$9.100 \pm 0.01$	$-0.161 \pm 0.021$	$9.090 \pm 0.01$	$-0.157 \pm 0.019$
M91	$8.982 \pm 0.01$	$-0.284 \pm 0.033$	$8.962 \pm 0.01$	$-0.246 \pm 0.032$
T04	$9.069 \pm 0.01$	$-0.306 \pm 0.036$	$9.045 \pm 0.01$	$-0.279 \pm 0.031$
	$10.1 < \log(\mathcal{M}/\mathcal{M}_\odot) < 10.3$		$9.9 < \log(\mathcal{M}/\mathcal{M}_\odot) < 10.1$	
KK04	$9.073 \pm 0.01$	$-0.177 \pm 0.031$	$9.048 \pm 0.01$	$-0.203 \pm 0.040$
M91	$8.930 \pm 0.01$	$-0.294 \pm 0.046$	$8.884 \pm 0.01$	$-0.267 \pm 0.054$
T04	$9.010 \pm 0.01$	$-0.294 \pm 0.050$	$8.960 \pm 0.01$	$-0.256 \pm 0.056$
	$9.7 < \log(\mathcal{M}/\mathcal{M}_\odot) < 9.9$		$9.5 < \log(\mathcal{M}/\mathcal{M}_\odot) < 9.7$	
KK04	$9.010 \pm 0.01$	$-0.225 \pm 0.076$	$8.954 \pm 0.01$	$-0.207 \pm 0.107$
M91	$8.825 \pm 0.01$	$-0.267 \pm 0.088$	$8.757 \pm 0.01$	$-0.187 \pm 0.101$
T04	$8.895 \pm 0.01$	$-0.286 \pm 0.094$	$8.822 \pm 0.01$	$-0.159 \pm 0.128$

<sup>a</sup> We model the measured change in the mean metallicity as a linear function of redshift given by:  $\langle 12 + \log(\text{O}/\text{H}) \rangle = \langle 12 + \log(\text{O}/\text{H}) \rangle_{z=0.1} + d[\log(\text{O}/\text{H})]/dz \times (z - 0.1)$ , where  $\langle 12 + \log(\text{O}/\text{H}) \rangle_{z=0.1}$  is the mean metallicity at  $z = 0.1$  and  $d[\log(\text{O}/\text{H})]/dz$  is the logarithmic rate of metallicity evolution.

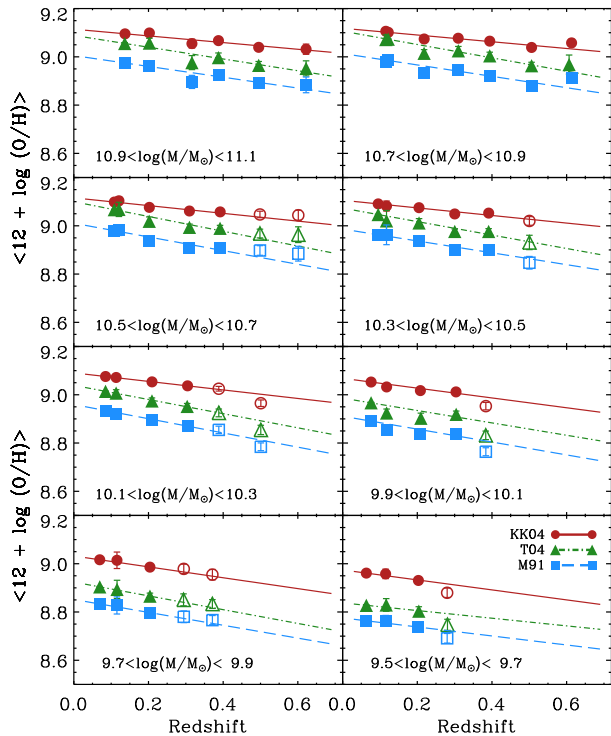


FIG. 14.— Mean metallicity of galaxies at  $z = 0.05 - 0.75$  as a function of stellar mass and redshift. The red points, green diamonds, and blue squares correspond to the KK04, T04, and M91 abundance calibration, respectively. Open and filled symbols represent stellar masses above and below our completeness limit, respectively. We model the observed evolution as a linear function of redshift given by equation (13), and show the best fitting lines using solid red, dot-dashed green, and dashed blue lines for each calibration. We find that galaxies in all eight stellar mass bins become progressively more metal-poor with increasing redshift at comparable rates.

alone it is impossible to ascertain which of these three strong-line calibrations is “right.” The inevitable conclusion, therefore, is that the uncertainties in both the

absolute metallicities and the relative rates of metallicity evolution we measure are dominated by systematic errors in the strong-line abundance calibrations.

With the preceding discussion in mind, we now explore in more detail whether the chemical enrichment rate depends on stellar mass. In Figure 15 we plot  $d[\log(\text{O}/\text{H})]/dz$  versus stellar mass for galaxies with  $\mathcal{M} = 10^{9.7} - 10^{11.1} \mathcal{M}_\odot$  using the KK04 (red points), T04 (green triangles), and M91 (blue squares) abundance calibration. We exclude our lowest stellar mass bin in the following because it is most affected by the limited redshift coverage of AGES in this stellar mass range. In each stellar mass interval we use the average mass of all the galaxies in that bin (i.e., across all redshifts), although

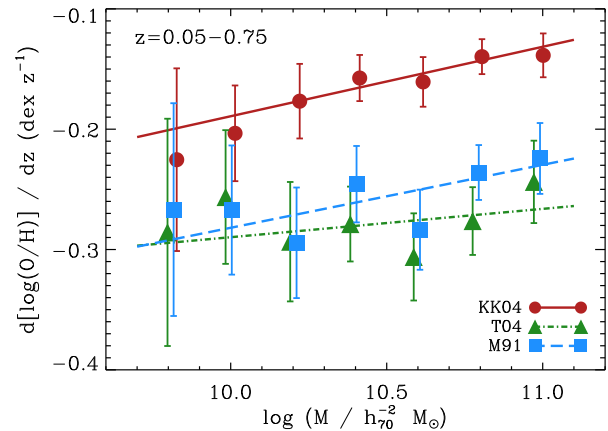


FIG. 15.— Redshift-dependent rate of change in the mean oxygen abundance for star-forming galaxies at  $z = 0.05 - 0.75$  vs. stellar mass. The red points, green diamonds, and blue squares correspond to the KK04, T04, and M91 calibrations, respectively, while the corresponding solid red, dot-dashed green, and dashed blue lines show the best-fitting linear relation (see Table 5). The KK04 calibration yields the smaller *absolute* rate of metallicity evolution,  $-0.160 \text{ dex } z^{-1}$  at  $\mathcal{M} = 10^{10.5} \mathcal{M}_\odot$ , but the steepest stellar mass dependence. By contrast, the T04 and M91 calibrations indicate a large rate of metallicity evolution,  $\sim -0.26 \text{ dex}$  per unit redshift, and no significant dependence of this rate on stellar mass.



we have applied small horizontal offsets to the points in this figure for clarity.

To quantify the observed trends we fit a linear model of the form

$$\frac{d[\log(\text{O}/\text{H})]}{dz} = a_0 + a_1 \log\left(\frac{\mathcal{M}}{10^{10.5} \mathcal{M}_\odot}\right), \quad (14)$$

where  $a_0$  is the rate of evolution in dex per unit redshift, and  $a_1$  characterizes the power-law dependence of this rate on stellar mass. We list the best-fitting coefficients and uncertainties for the individual calibrations in Table 6.

Figure 15 nicely encapsulates many of the principal results of this section, and of this paper. First, the factor of  $\sim 1.7$  shallower rate of metallicity evolution implied by the KK04 calibration compared with the T04 and M91 calibrations is clearly apparent in this figure. Specifically, the KK04 calibration indicates a metal enrichment rate of  $-0.160 \pm 0.009 \text{ dex } z^{-1}$  for star-forming galaxies with  $\mathcal{M} = 10^{10.5} \mathcal{M}_\odot$ , while the T04 and M91 calibrations indicate more rapid evolution,  $-0.278 \pm 0.015$  and  $-0.256 \pm 0.014 \text{ dex } z^{-1}$ , respectively. The KK04 calibration also indicates a steeper dependence of the rate of metallicity evolution on stellar mass, whereas the T04 and M91 calibrations show no statistically significant ( $\lesssim 1\sigma$ ) dependence on mass for galaxies with  $\mathcal{M} = 10^{9.8} - 10^{11} \mathcal{M}_\odot$ . We emphasize, however, that even the stellar mass dependence implied by the KK04 calibration,  $0.058 \pm 0.029$ , is only marginally statistically significant ( $2\sigma$ ). We conclude, therefore, that there is no compelling evidence that the  $\mathcal{M} - Z$  relation evolves differentially, that is, in a mass-dependent way, over this range of stellar masses and redshifts.

We conclude this section by examining whether we can synthesize the preceding results in terms of evolution in the physical parameters  $12 + \log(\text{O}/\text{H})^*$  and  $\mathcal{M}^*$  given by equation (10) (see also Appendix B). Recall that  $12 + \log(\text{O}/\text{H})^*$  is the asymptotic metallicity of the  $\mathcal{M} - Z$  relation, and  $\mathcal{M}^*$  represents the stellar mass at which the relation begins to turn over. We begin with the simplest possible model by fixing  $\mathcal{M}^*$  and  $\gamma$  at their local values and allowing  $12 + \log(\text{O}/\text{H})^*$  to vary linearly with redshift as

$$12 + \log(\text{O}/\text{H})_z^* = 12 + \log(\text{O}/\text{H})_{z=0.1}^* + \mathcal{P}(z - 0.1), \quad (15)$$

where  $12 + \log(\text{O}/\text{H})_{z=0.1}^*$  is the characteristic metallicity at  $z = 0.1$  (see Table 3), and  $\mathcal{P}$  is the rate of chemical evolution in dex per unit redshift. Solving for the maximum likelihood value of  $\mathcal{P}$  using MPFIT<sup>31</sup>, we obtain  $\mathcal{P} = -0.137 \pm 0.017$ ,  $-0.258 \pm 0.034$ , and  $-0.250 \pm 0.044 \text{ dex } z^{-1}$  using the KK04, T04, and M91 calibration, respectively. These results are statistically consistent with the rate of chemical evolution given in Table 6 (ignoring the weak dependence on stellar mass), and therefore provide a convenient way of evaluating the  $\mathcal{M} - Z$  relation for star-forming galaxies at any redshift between  $z = 0.05$  and  $z = 0.75$ .

In Figure 16 we show the evolution of the T04-based  $\mathcal{M} - Z$  relation predicted by this empirical model, along

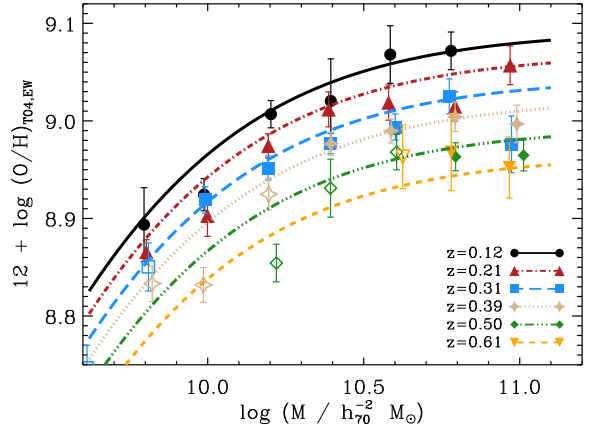


FIG. 16.— Comparison of the T04-based mean metallicities of AGES galaxies in six redshift bins between  $z = 0.1$  and  $z = 0.6$  to the empirical model proposed in §6.2.1. The filled (open) symbols represent stellar mass bins above (below) our completeness limit in each redshift bin, and to best match the plotted measurements we have evaluated the model at the median redshift of the galaxies in each sample, as indicated in the legend. We find that this simple model, in which the  $\mathcal{M} - Z$  relation simply shifts toward lower metallicity without changing its shape, reproduces the observations well.

with the mean metallicities from AGES in our six redshift bins. As before, the filled and open symbols represent stellar mass bins above and below our completeness limit, respectively. To optimally match the measurements plotted, we evaluate the model at the median redshift of the galaxies in each redshift bin, as indicated in the legend. We find that this simple model, which consists of a linear decrease in the oxygen abundance of star-forming galaxies as a function of redshift and an invariant  $\mathcal{M} - Z$  relation *shape*, reproduces the observed data reasonably well.

We also attempt to fit the data with a more complex model, in which the characteristic stellar mass  $\mathcal{M}^*$  also evolves linearly with redshift as

$$\log(\mathcal{M}_z^*/\mathcal{M}_\odot) = \log(\mathcal{M}_{z=0.1}^*/\mathcal{M}_\odot) + \mathcal{R}(z - 0.1). \quad (16)$$

Combining this relation with equation (10), the redshift-dependent  $\mathcal{M} - Z$  relation becomes

$$12 + \log(\text{O}/\text{H})_z = 12 + \log(\text{O}/\text{H})_{z=0.1}^* + \mathcal{P}(z - 0.1) - \log\left[1 + \left(\frac{\mathcal{M}^* \times 10^{R(z-0.1)}}{10^9 \mathcal{M}_\odot}\right)^\gamma\right], \quad (17)$$

where once again we fix  $\gamma$  at its local value. Finding the maximum likelihood values of the free parameters, we find that the data are only marginally better fit, but not by a statistically meaningful amount, compared to the simpler model in which  $\mathcal{R} = 0$ . We conclude that our metallicity measurements from the SDSS and AGES are statistically consistent with an  $\mathcal{M} - Z$  relation that shifts toward lower metallicity with decreasing redshift, but whose shape does not evolve.

<sup>31</sup> A Levenberg-Marquardt least-squares minimization routine available at <http://cow.physics.wisc.edu/~simcraig/idl>.

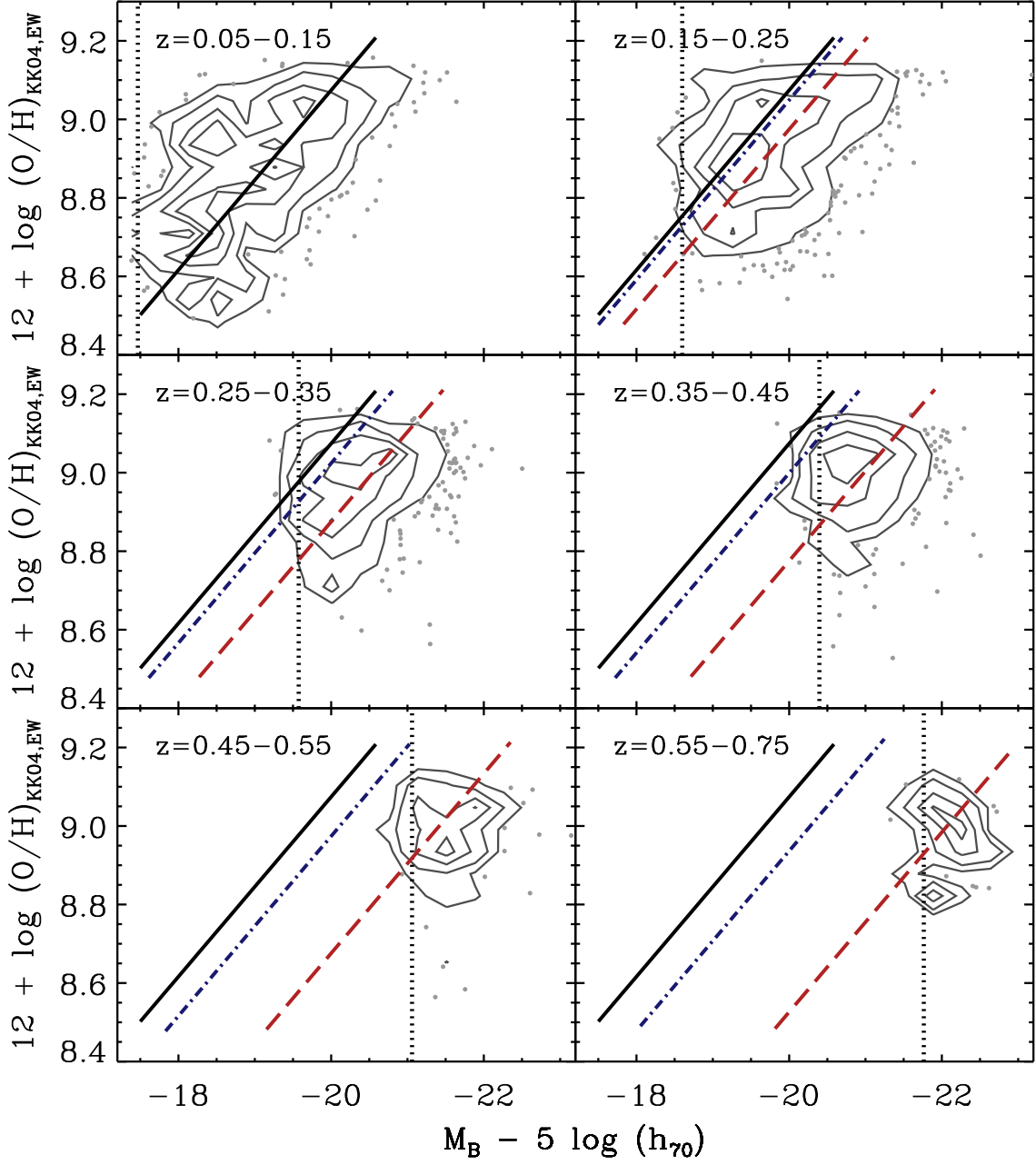


FIG. 17.— Evolution of the  $B$ -band  $L - Z$  relation at  $z = 0.05 - 0.75$  based on the KK04 abundance calibration. For reference, the contours enclose 25%, 50%, 75%, and 90% of the galaxies in each redshift interval, and the small grey points represent individual galaxies that lie outside the 90% contour level. The solid black line reproduced in every panel shows the local  $L - Z$  relation derived in §6.1.2, and the vertical dashed lines show the completeness limits of AGES in each redshift interval (see §4.3). Taken at face value, the observations suggest  $-1.00 \text{ dex } z^{-1}$  of metallicity evolution at fixed luminosity (*dashed red line*), which significantly exceeds the much smaller rate of metallicity evolution inferred from the  $\mathcal{M} - Z$  relation (*dot-dashed blue line*). We attribute the discrepancy to significant brightening in the  $B$ -band luminosities of star-forming galaxies over this redshift range, and conclude that the  $B$ -band  $L - Z$  relation does not provide an effective means of constraining the chemical enrichment histories of galaxies.

TABLE 6  
STELLAR MASS DEPENDENCE OF THE RATE OF  
METALLICITY EVOLUTION<sup>a</sup>

Calibration	$a_0$	$a_1$
KK04	$-0.160 \pm 0.009$	$0.058 \pm 0.029$
T04	$-0.278 \pm 0.015$	$0.024 \pm 0.046$
M91	$-0.256 \pm 0.014$	$0.052 \pm 0.042$

<sup>a</sup> Mass-dependent rate of metallicity evolution given by  $d[\log(\text{O}/\text{H})]/dz = a_0 + a_1 \log(\mathcal{M}/10^{10.5} \mathcal{M}_\odot)$ , where the units of  $a_0$  are dex per unit redshift.

We turn next to the evolution of the  $B$ -band  $L - Z$  relation at intermediate redshift. In Figure 17 we plot the relationship between  $M_B$  and oxygen abundance in the same redshift bins used in the previous section. For clarity, we again only show the  $L - Z$  relation using the KK04 calibration, but we present results from the other two calibrations below. The solid black line reproduced in every panel is the SDSS  $L - Z$  relation derived in §6.1.2, and the vertical dotted lines show the absolute magnitude limits of the survey in each redshift bin (see Table 2).

Taken at face value, Figure 17 suggests that galaxies at  $z = 0.05 - 0.75$  have experienced a significant amount of metallicity evolution, luminosity evolution, or both. To quantify the observed trends we modify the local  $L - Z$  relation given by equation (11) to allow the characteristic metallicity at  $z = 0.1$ ,  $c_{0,z=0.1}$ , to change linearly with redshift according to  $c_0(z) = c_{0,z=0.1} + \mathcal{S}(z - 0.1)$ , where the rate of metallicity evolution,  $\mathcal{S}$ , is in units of dex  $z^{-1}$ . We also allow the ensemble of star-forming galaxies in AGES to brighten as  $M_B(z) = M_{B,z=0.1} + Q_B(z - 0.1)$ , where  $Q_B$  is the rate of luminosity evolution in mag  $z^{-1}$ . Combining these relations with equation (11), the  $B$ -band  $L - Z$  relation at a given redshift becomes

$$12 + \log(\text{O}/\text{H})_z = c_{0,z=0.1} + c_1(M_B + 20.5) + (\mathcal{S} + c_1 Q_B)(z - 0.1). \quad (18)$$

Note that we have implicitly assumed that the *slope* of the  $L - Z$  relation,  $c_1$ , does not change with redshift, which is likely an oversimplification; unfortunately, AGES does not extend far enough down the luminosity function to test this assumption.

Momentarily ignoring luminosity evolution (i.e., setting  $Q_B = 0$ ), we find  $\mathcal{S} = -1.00$ ,  $-1.32$ , and  $-1.11$  dex  $z^{-1}$  using the KK04, T04, and M91 calibration, respectively, with negligible statistical uncertainties. We show the results of this evolutionary model as a dashed red line in Figure 17 for the KK04 calibration. However, these results are clearly at odds with the  $\sim -0.2$  dex  $z^{-1}$  of evolution inferred from our analysis of the  $\mathcal{M} - Z$  relation in §6.2.1, which we plot in Figure 17 as a dot-dashed blue line for comparison. We conclude, therefore, that the evolution of the  $B$ -band  $L - Z$  relation *requires* star-forming galaxies in AGES to have been brighter in the past, that is  $Q_B < 0$ . Indeed, setting  $\mathcal{P} = \mathcal{S}$  and solving for  $Q_B$ , we obtain  $Q_B = -3.5 \pm 0.15$  mag  $z^{-1}$  averaged over all three calibrations.

Measurements of the  $B$ -band luminosity function for

blue, star-forming galaxies at intermediate redshift provide an independent estimate of  $Q_B$ . For example, Blanton (2006) report a brightening of  $\sim 1.0$  mag for blue galaxies since  $z = 1$  using data from the SDSS and DEEP2 surveys; Faber et al. (2007) find a luminosity evolution rate  $\sim 1.4$  mag  $z^{-1}$  over the same redshift interval from an analysis of COMBO-17 and DEEP2 observations; and Cool et al. (2011) find  $Q_B = -1.3 \pm 0.2$  mag  $z^{-1}$  based on data from the SDSS and AGES. Although we find a considerably larger rate of luminosity evolution, recall that the luminosity function studies cited above measure the brightening at the ‘knee’ of the luminosity function,  $M_B^*$ , whereas our sample is dominated galaxies with  $M_B \ll M_B^*$  at higher redshift. Moreover, our assumption that the  $L - Z$  relation is linear is clearly not strictly appropriate in light of our analysis of the  $\mathcal{M} - Z$  relation in §6.2.1. The principal conclusion from the preceding analysis is that the  $B$ -band  $L - Z$  relation does *not* provide a robust means of quantifying the evolution in the chemical abundances of star-forming galaxies at higher redshift, as has been previously emphasized by Tremonti et al. (2004), Salzer et al. (2005), Zahid et al. (2011), and others.

### 6.3. Comparison with Previous Results

A detailed comparison of our results with previous studies poses numerous challenges. Among the issues to consider are the wide variations in sample selection, sample size, and survey area (i.e., cosmic variance), differences in the methods used to estimate oxygen abundances (i.e., choice of abundance diagnostics), and differences in the treatment of systematic effects like dust attenuation, stellar absorption, and AGN contamination. Moreover, most previous abundance studies have measured the evolution of the  $B$ -band  $L - Z$  relation, which we have seen is not a robust means of quantifying the chemical evolution histories of star-forming galaxies. And finally, different studies have relied on disparate measurements of the local  $\mathcal{M} - Z$  and  $L - Z$  relations, which can also influence the amount of chemical evolution inferred.

With these issues in mind, we focus our comparison on three recent measurements of the  $\mathcal{M} - Z$  relation at intermediate redshift by Cowie & Barger (2008, hereafter CB08), Lamareille et al. (2009, hereafter L09), and Zahid et al. (2011, hereafter ZKB11). We select these studies because they are based on a large number of homogeneously selected galaxies over a relatively wide area, and they make use of state-of-the-art techniques for measuring stellar mass from broadband photometry. CB08 derived gas-phase oxygen abundances for roughly 200 galaxies at  $z = 0.05 - 0.9$  in the 145 arcmin<sup>2</sup> GOODS-N (Giavalisco et al. 2004) field, L09 measured the  $\mathcal{M} - Z$  relation at  $z = 0.0 - 0.9$  based on optical spectroscopy of  $\sim 3000$  galaxies in the 0.61 deg<sup>2</sup> VVDS-DEEP and 6.1 deg<sup>2</sup> VVDS-WIDE survey fields (Le Fèvre et al. 2005; Garilli et al. 2008), and ZKB11 measured the metallicities of 1350 galaxies at  $z = 0.75 - 0.82$  selected from the 3.5 deg<sup>2</sup> DEEP2 survey (Davis et al. 2003). For simplicity, we concentrate here on a single redshift interval,  $z = 0.6 - 0.8$ , for which all three studies have measured the  $\mathcal{M} - Z$  relation. Although this redshift range is the highest red-



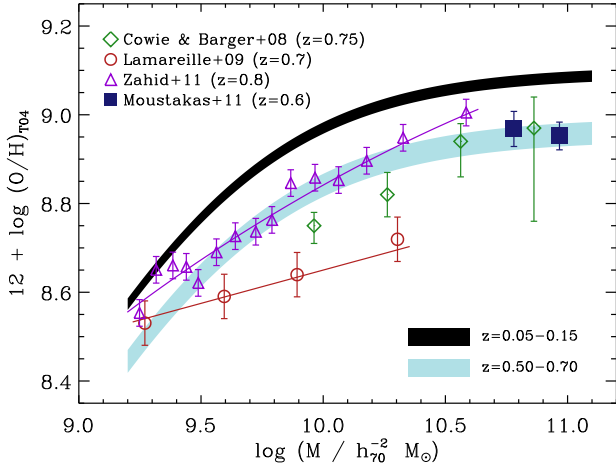


FIG. 18.— Comparison of the  $\mathcal{M} - Z$  relation we infer at intermediate redshift from AGES (filled blue squares) to previous measurements by Cowie & Barger (2008) (open green diamonds), Lamareille et al. (2009) (open red circles), and Zahid et al. (2011) (open purple triangles), all converted to the T04 abundance scale and the Chabrier (2003) IMF. For comparison, we show the  $\mathcal{M} - Z$  relation at  $z \sim 0.1$  (shaded black region) and at  $z \sim 0.6$  (shaded light blue region) based on the empirical evolutionary model derived in §6.2.1. We find very good agreement between our empirical model, which is constrained at low stellar mass by our lower-redshift observations, and the detailed measurements by Zahid et al. (2011), and with Cowie & Barger (2008) above  $\sim 10^{10.5} M_{\odot}$ .

shift bin probed by AGES, in which our sample spans a relatively limited range of stellar mass, the evolutionary model of the  $\mathcal{M} - Z$  relation we derive in §6.2.1 is nevertheless constrained by our larger sample of lower redshift galaxies.

In Figure 18 we plot stellar mass versus oxygen abundance for galaxies at  $z \sim 0.7$ . We plot the mean metallicity measurements from CB08, L09, ZKB11, and AGES using green diamonds, red circles, purple triangles, and filled dark blue squares, respectively. For consistency across all the studies we show metallicities derived using the T04 calibration of  $R_{23}$ . CB08 and L09 derive their abundances using this calibration, and we have applied the appropriate conversion formula from Kewley & Ellison (2008) to adjust the measurements from ZKB11. Finally, we subtract 0.25 dex from the CB08 stellar masses to convert them to the Chabrier (2003) IMF. We also show in Figure 18 the  $\mathcal{M} - Z$  relation at  $z = 0.05 - 0.15$  as a shaded black region, and the  $\mathcal{M} - Z$  relation at  $z = 0.50 - 0.70$  from AGES as a light blue shaded region.

Examining Figure 18, we find generally very good agreement between the intermediate-redshift  $\mathcal{M} - Z$  relation we infer from AGES, and the  $\mathcal{M} - Z$  relations measured by CB08 and ZKB11. The agreement with ZKB11 between  $\sim 10^{9.5} - 10^{10.5} M_{\odot}$  is especially striking since it represents an extrapolation of the  $\mathcal{M} - Z$  relation we measure at lower redshift (AGES does not probe these stellar masses at this redshift). In particular, our conclusion that the evolution of the  $\mathcal{M} - Z$  relation does not depend significantly on stellar mass (see §6.2.1) is strengthened by this comparison. The evolution of the  $\mathcal{M} - Z$  relation since  $z \sim 0.7$  is con-

sistent with a progressive increase in metallicity, with no significant change in shape, contrary to the conclusions of several previous studies (e.g., Savaglio et al. 2005; Lamareille et al. 2009). Our intermediate-redshift  $\mathcal{M} - Z$  relation is also reasonably consistent with the measurements by CB08, particularly at the massive end. Between  $\sim 10^{10} - 10^{10.3} M_{\odot}$ , however, CB08 measure slightly lower mean metallicities, but given the uncertainties in this comparison the differences are probably not significant. On the other hand, L09 measure mean abundances that are  $\sim 50\%$  lower at  $\sim 10^{10.3} M_{\odot}$  and a considerably shallower  $\mathcal{M} - Z$  relation. The origin of this discrepancy is not clear, although the relatively low spectral resolution ( $R \approx 230$ ) of the VVDS spectra analyzed by L09 may introduce unintended selection effects related to a preferential loss of massive, metal-rich galaxies with relatively low equivalent-width emission lines (see, e.g., Liang et al. 2004). On balance, we conclude that our measurement of the  $\mathcal{M} - Z$  relation at intermediate redshift is consistent with previous measurements.

## 7. SYSTEMATIC UNCERTAINTIES

Before discussing our results in the next section, we first investigate how emission-line selection effects, aperture bias, AGN contamination, and other potential sources of systematic bias might impact our conclusions. Readers that are only interested in the interpretation of our results can safely skip ahead to §8.

### 7.1. Emission-Line Selection Effects

We selected our SDSS and AGES emission-line galaxy samples using an  $H\beta$  flux cut, and by requiring well-measured  $[O II] \lambda 3727$  and  $[O III] \lambda 5007$  emission lines (see §4.1). Here, we examine how these emission-line selection criteria might affect our conclusions.

At a basic level, gas-phase abundances can only be measured for galaxies with ongoing star formation, otherwise  $H\beta$  will be absent from their integrated spectra. In principal, the metallicity of the gas during the last major epoch of star formation is encoded in the distribution of *stellar* metallicities of the stars responsible for the continuum light; however, disentangling this relationship is complicated (although not intractable; see, e.g., Gallazzi et al. 2005; Tojeiro et al. 2007; Cid Fernandes et al. 2007; Panter et al. 2008), and outside the scope of the present analysis. At face value, therefore, our  $H\beta$  flux cut translates into an  $H\beta$  luminosity cut, or, modulo aperture effects and dust attenuation, a cut in absolute SFR (Kennicutt 1998b).

In detail, however, our AGES and SDSS samples are also  $I$ - and  $r$ -band limited, respectively; therefore,  $H\beta$  in a galaxy at a given redshift must be sufficiently bright relative to the underlying continuum to be detected and measured given the design of the spectroscopic survey (instrumental setup, flux limit, exposure time, etc.). In other words, in a broadband flux-limited survey, an  $H\beta$  flux cut translates into a EW-limited sample as a function of redshift (see Fig. 2). This  $EW(H\beta)$  limit is related to the minimum specific SFR (Kennicutt et al. 1994; Brinchmann et al. 2004) a galaxy must exceed to enter our sample, although, the minimum (redshift-dependent) specific SFR depends on many details, including aperture effects, dust attenuation, the frequency of starbursts, and

the amount of luminosity and SFR evolution in galaxies. Nevertheless, comparison of our results against theoretical models should be aware of the systematic loss of galaxies with low specific SFRs with increasing redshift.

In addition to excluding galaxies with low specific and absolute SFRs, our  $H\beta$  flux cut may also exclude extremely dusty galaxies. In an integrated spectrophotometric survey of star-forming galaxies in the nearby Universe that included a significant number of infrared-luminous galaxies, Moustakas & Kennicutt (2006) found that galaxies with significant  $H\alpha$  emission but with  $H\beta$  too buried in the stellar continuum to be measurable constituted  $\lesssim 10\%$  of the sample with  $L_{\text{IR}} > 10^{11} L_{\odot}$  (so-called LIRGs; Sanders & Mirabel 1996). Given the rapid increase in the incidence of LIRGs to  $z = 1$  (Le Floch et al. 2005; Rodighiero et al. 2010), our sample may be missing the dustiest galaxies at each redshift. On the other hand, we do not expect the metallicity properties of the small fraction of very dusty galaxies to be significantly different with respect to the galaxies that satisfy our  $H\beta$  selection. Nevertheless, future studies of distant emission-line galaxies that are  $H\alpha$ - or even Pa $\alpha$ -selected would mitigate the selection effects due to dust attenuation.

Next, we also required our sample to have a well-measured [O II] emission line. In §4.1 we found that galaxies that failed this cut constituted  $\sim 6\%$  of the  $H\beta$ -selected sample and were frequently dusty starbursts. In a volume-limited sample of SDSS galaxies, Yan et al. (2006) found that galaxies with significant  $H\alpha$  emission but without [O II] emission constituted  $\sim 15\%$  of their sample, the overwhelming majority of which had AGN-like forbidden emission-line ratios, and the remainder likely dusty star-forming galaxies. Therefore, we conclude that requiring a well-measured [O II] emission line has a negligible effect on our results. Indeed, the high detection rate of [O II], due to its intrinsic strength and relative insensitivity to variations in metallicity and excitation across a wide range of physical conditions, is why this line remains an appealing SFR diagnostic at both low and high redshift (Moustakas et al. 2006; Gilbank et al. 2010; Mostek et al. 2011).

Finally, we also required our sample of emission-line galaxies to have a significant [O III]  $\lambda 5007$  emission line. Unlike [O II], the strength of [O III] decreases rapidly with increasing metallicity and decreasing excitation (Kewley & Dopita 2002); therefore, an [O III]-limited sample could be biased against massive, metal-rich galaxies. To estimate the magnitude of this potential systematic bias, we appeal to the T04-based  $\mathcal{M} - Z$  relation plotted in the lower-left panel of Figure 10. Unlike the T04 calibration of  $R_{23}$  (see Appendix A), the MPA-JHU metallicities do not explicitly require significant [O III] emission. We find that the T04 and MPA-JHU  $\mathcal{M} - Z$  relations agree very well, and only begin to deviate from one another around  $\mathcal{M} \approx 10^{10.6} M_{\odot}$ . Furthermore, the magnitude of the deviation, in the sense that the T04-based  $\mathcal{M} - Z$  relation at large masses might be underestimated, is always  $\lesssim 0.05$  dex to  $10^{11.1} M_{\odot}$ . We conclude, therefore, that requiring well-measured [O III] emission line in our AGES and SDSS samples does not significantly bias our conclusions.

## 7.2. Strong-Line Abundance Calibration

We have shown that the choice of strong-line abundance calibration has a significant effect on the absolute normalization of the  $\mathcal{M} - Z$  relation and, to second order, its shape (see Fig. 10). The KK04 abundance calibration, for example, yields oxygen abundances that are, on average, 15% – 40% higher than abundances derived using the T04 and M91 calibrations, and results in a markedly shallower  $\mathcal{M} - Z$  relation. At fixed stellar mass, these differences translate into a factor of 1.5 – 2 systematic variation in the *rate* at which the mean metallicity of star-forming galaxies changes with redshift (see §6.2.1 and Fig. 14).

These results highlight two important points. First, great care must be exercised when examining chemical evolutionary trends with redshift based on oxygen abundances derived using different strong-line calibrations. For example, the abundances of distant galaxies derived using the KK04 calibration should not, in general, be compared blindly to the  $\mathcal{M} - Z$  relation published by Tremonti et al. (2004). And second, even differential trends in metallicity can depend on the adopted abundance calibration. An analogous result was found by Bresolin et al. (2009) and Moustakas et al. (2010), who showed that the slope of the radial abundance gradient in nearby disk galaxies depends on the adopted strong-line calibration. Obviously both these effects have wide-ranging implications for using abundance measurements to constrain theoretical models (e.g., Dutton et al. 2010; Davé et al. 2011b).

Various techniques have been devised to deal with these issues. For example, Kewley & Ellison (2008) provide polynomial expressions to transform abundances derived using different strong-line calibrations onto a common abundance scale. Other authors have used a combination of abundances derived using electron temperature measurements and photoionization models to attempt to generate a self-consistent suite of abundance diagnostics based on different strong-line ratios (Nagao et al. 2006; Maiolino et al. 2008), although these methods are susceptible to systematic errors and inconsistencies in the photoionization models and abundance measurements based on electron temperature estimates. However, these calibrations should not be applied beyond the range of parameter space for which they were developed (see especially the discussion in Stasińska 2010). Moreover, these techniques implicitly ignore the *origin* of the systematic differences between abundance derived using theoretical and empirical strong-line methods (see Moustakas et al. 2010, and references therein), which may introduce metallicity-dependent biases. These issues are particularly relevant when applying strong-line calibrations based on the strength of the *nitrogen* emission line [N II]  $\lambda 6584$  to infer the *oxygen* abundances of galaxies, such as [N II]/[O II], [N II]/ $H\alpha$ , and ([O III]/ $H\beta$ )/([N II]/ $H\alpha$ ) (also known as the N2O2, N2, and O3N2 diagnostics, respectively; Kewley & Ellison 2008, and references therein). Because nitrogen is both a primary and secondary nucleosynthetic product, the N/O abundance ratio in galaxies has a well-known second-order dependence on the recent star formation history, which can introduce a non-negligible systematic bias in the inferred metallicities

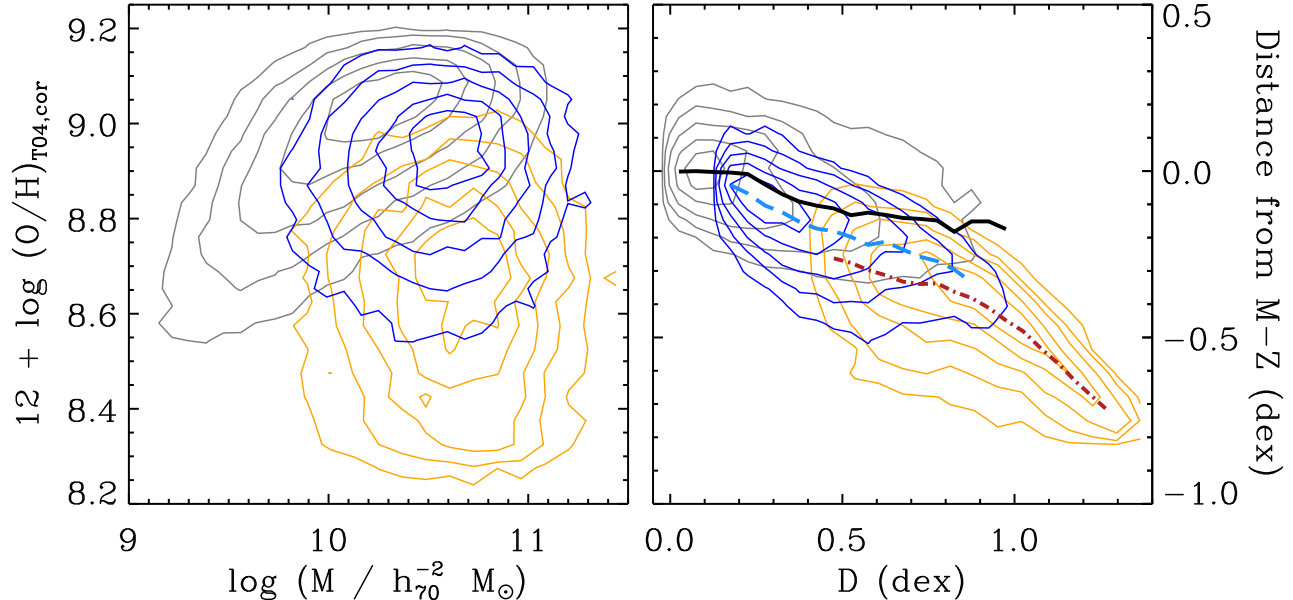


FIG. 19.— Effect of AGN contamination on metallicities derived using the  $R_{23}$  parameter. The grey, blue, and orange contours, enclosing 25%, 50%, 75%, 90%, and 97.5% of the galaxies in each sample, represent galaxies classified as SF, SF/AGN, and AGN, respectively (see §7.3 for the definition of these classes). (*Left*) Inspection of the T04-based  $\mathcal{M} - Z$  relation clearly demonstrates that applying an  $R_{23}$ -based abundance calibration to galaxies hosting AGN results in metallicities that are spuriously low. (*Right*) Residuals from the  $\mathcal{M} - Z$  relation vs. distance,  $D$ , from  $([\text{N II}]/\text{H}\alpha, [\text{O III}]/\text{H}\beta) = (-0.45, -0.5)$  dex in the BPT diagram. The solid black, dashed blue, and dot-dashed red curves show the median abundance residuals as a function of  $D$  for the SF, SF/AGN, and AGN class, respectively. We find that the metallicity bias for AGN is always  $\gtrsim 0.2$  dex, and can be as high as  $\sim 0.6$  dex; meanwhile, the metallicity bias for SF/AGN is always  $\lesssim 0.1$  dex.

(Contini et al. 2002; Pilyugin et al. 2003; Yin et al. 2007; Pérez-Montero & Contini 2009; Thuan et al. 2010). Exploring these issues in more quantitative detail is beyond the scope of this paper, suffice it to say that we have avoided most of these problems by using three independent abundance calibrations and applied them to our full sample of SDSS and AGES galaxies consistently.

### 7.3. Residual AGN Contamination

In §4.2 we identified AGN among the AGES emission-line galaxies using a combination of the BPT diagram, the Yan et al. (2011) empirical diagnostic diagram, and a variety of complementary multiwavelength diagnostics from the X-ray to the radio. We conservatively estimated, however, that up to  $\sim 50\%$  of the emission-line galaxies in our  $z > 0.4$  sample may host composite (weak) AGN. Of course, the true fraction may be higher or lower depending on a variety of different factors, such as evolution in the luminosity and optical color distribution of galaxies hosting AGN, dilution of the AGN spectrum due to aperture effects, and so forth. Nevertheless, oxygen abundances derived from the  $R_{23}$  parameter are particularly susceptible to AGN contamination because line-ratios involving high-ionization lines such as  $[\text{O III}]/\text{H}\beta$  are preferentially elevated in the narrow-line regions of AGN (e.g., Osterbrock & Ferland 2006). For galaxies on the upper  $R_{23}$  branch, an unidentified contribution from an AGN to the integrated emission-line spectrum will cause  $R_{23}$  to be *overestimated*, and therefore the metallicity to be systematically *underestimated* (see §5.2 and Appendix A).

We use our SDSS sample to quantify the effect of unidentified AGN on our  $R_{23}$ -based oxygen abundances. In Figure 19 (*left*) we plot the T04-based  $\mathcal{M} - Z$  relation for three sets of objects: (1) galaxies classified as star-forming using the BPT diagram (*grey contours*, hereafter SF galaxies); (2) objects classified as AGN using the BPT diagram, but as star-forming using the Yan et al. (2011) diagnostic diagram (*blue contours*, hereafter SF/AGN); and (3) objects classified as AGN using both the BPT and the Yan et al. (2011) diagnostic diagram (*orange contours*, hereafter AGN). In this example we adopt the T04 calibration, but the same conclusions would hold using any other  $R_{23}$ -based abundance calibration. Figure 19 (*right*) plots the residuals from the  $\mathcal{M} - Z$  relation against the logarithmic distance,  $D$ , from  $\log([\text{N II}]/\text{H}\alpha) = -0.45$ ,  $\log([\text{O III}]/\text{H}\beta) = -0.5$  in the BPT diagram, at the base of the sequence of star-forming galaxies (see Fig. 4 and Kauffmann et al. 2003c). For example, a galaxy with  $\log([\text{N II}]/\text{H}\alpha) = +0.2$  and  $\log([\text{O III}]/\text{H}\beta) = +0.6$  would have  $D = \sqrt{(0.2 + 0.45)^2 + (0.6 + 0.5)^2} = 0.66$  dex. In essence, powerful AGN have large values of  $D$  because they lie far from the tight sequence of star-forming emission-line galaxies, while normal star-forming galaxies have small  $D$  values. The solid black, dashed blue, and dot-dashed red curves show the median abundance residuals as a function of  $D$  for the SF, SF/AGN, and AGN, respectively.

Figure 19 clearly reveals why AGN and, to a lesser extent SF/AGN, must be removed from any  $R_{23}$ -based abundance study: the inferred metallicities are spuri-



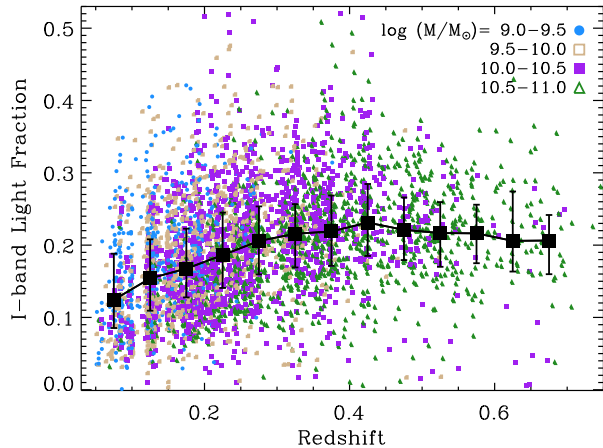


FIG. 20.— Fraction of  $I$ -band light subtended by the AGES  $1''.5$  diameter fiber-aperture for galaxies in four bins of stellar mass vs. redshift. The large solid black squares correspond to the median light fraction (for all objects) in fixed 0.05-wide bins of redshift, and the error bars indicate the interquartile range of the light fraction in each bin. The median light-fraction is a weak function of redshift, increasing from  $\sim 13\%$  at  $z \sim 0.1$ , to  $\sim 20\%$  above  $z \gtrsim 0.25$ .

ously low because the emission lines are not due to photoionization from massive stars. Quantitatively, we find a very strong correlation between  $D$  and the metallicity bias. Among AGN, the metallicity can be (mistakenly) underestimated by as much as  $\sim 0.6$  dex for objects with  $D \sim 1.2$ , with a typical bias of  $\sim 0.2$  dex for most objects. Meanwhile, the metallicity bias for SF/AGN is considerably more modest,  $\lesssim 0.1$  dex (the separation between the solid black and dashed blue curves in the right panel) over the full range of  $D$  values. A 50–50 mixture of SF and SF/AGN, therefore, would exhibit a mean metallicity bias of  $\lesssim 0.05$  dex. We conclude, therefore, that unidentified SF/AGN in our sample of AGES galaxies, even those at  $z > 0.4$ , should not significantly bias our measurement of the evolution of the  $\mathcal{M} - Z$  relation.

#### 7.4. Aperture Bias

Most star-forming disk galaxies in the local Universe exhibit radial abundance gradients, in the sense that the metallicity in their central regions is higher than in their outskirts (Zaritsky et al. 1994; van Zee et al. 1998; Moustakas et al. 2010). Therefore, oxygen abundances derived from fiber-optic spectra, which target the inner, metal-rich regions of the galaxy, may be biased relative to abundances derived from integrated spectroscopy (Zaritsky et al. 1995; Kochanek et al. 2001; Kewley et al. 2005; Moustakas et al. 2006). If the amount of light subtended by the spectroscopic aperture is a strong function of redshift then so-called aperture bias (or aperture effects) could mimic genuine chemical evolution.

In Figure 20 we explore this question by plotting the  $I$ -band light fraction versus redshift for galaxies in our abundance sample divided into four bins of stellar mass,  $\log(M/M_\odot)$ : 9–9.5 (*blue points*), 9.5–10 (*open tan squares*), 10–10.5 (*filled purple squares*), and 10.5–11 (*green diamonds*). We define the light-fraction as the flux measured from our unconvolved  $I$ -band mosaics inside a  $1''.5$  diameter aperture centered on each galaxy, divided

by the total galaxy flux. The median light-fraction for the whole sample is 0.19, with an interquartile range of 0.14–0.24; however, Figure 20 reveals that the light-fraction is indeed a (weak) function of redshift. The large solid black squares correspond to the median light fraction in 0.05-wide bins of redshift, while the error bars indicate the interquartile range in each bin. The median light-fraction increases from  $\sim 13\%$  at  $z \sim 0.1$ , and then remains approximately constant at  $\sim 20\%$  above  $z \gtrsim 0.25$ . For reference, the physical diameter subtended by the AGES fiber-aperture is 5.9 kpc at  $z = 0.25$ , ranging from 2.8–10.7 kpc between  $z = 0.1 - 0.7$ .

Taking these results at face value, the *relative* metallicities we measure in AGES should be insensitive to aperture bias between  $z = 0.25 - 0.75$ . Below  $z \sim 0.25$  we expect aperture effects to be more severe; however, at these redshifts we rely on the abundances inferred from the SDSS spectra, which were obtained through a  $3''$  diameter fiber-optic aperture. The median  $i$ -band light-fraction for our SDSS sample is 0.24, with an interquartile range of 0.18–0.31. The physical diameter subtended by the SDSS fiber is 5.5 kpc at  $z = 0.1$ , ranging from 2.9–9.9 kpc between  $z = 0.05 - 0.2$ . In other words, by combining our SDSS sample at low redshift with AGES at higher redshift the relative metallicity evolution we measure should be insensitive to aperture effects. Of course, because of the existence of abundance gradients, the *absolute* metallicities we measure may be susceptible to aperture bias at all redshifts.

We can place these results on a more quantitative footing by performing some simple simulations. For convenience, in the following we adopt the notation  $Z \equiv 12 + \log(O/H)$ . The inputs to our simulation are the (assumed linear) abundance gradient  $Z(r) = Z_0 + (dZ/dr)r$ , where  $r$  is the galactocentric radius,  $Z_0$  is the metallicity at  $r = 0$ , and  $dZ/dr$  is the slope; and the radial surface-brightness profile,  $I(r) \propto \exp[-(r/r_0)^{1/n}]$ , where  $n$  is the Sérsic (1968) index, and  $r_0$  is a scale factor that is related to the half-light radius,  $r_{50}$  (see Graham & Driver 2005 for the relationship). The Sérsic index indicates the *concentration* of the galaxy, with increasing  $n$  corresponding to a more centrally concentrated surface-brightness profile (e.g., Graham 2001; Peng et al. 2002). For example,  $n = 1$  implies a pure exponential disk, while  $n = 4$  corresponds to a classical de Vaucouleurs (1948)  $r^{1/4}$  light-profile.

At a given radius the enclosed light-fraction,  $F(r)$ , is given by

$$F(r) = \frac{\int_0^r I(r) r dr}{\int_0^\infty I(r) r dr}, \quad (19)$$

and the surface-brightness weighted metallicity is given by

$$\langle Z(r) \rangle \propto \frac{\int_0^r Z(r) I(r) r dr}{\int_0^r I(r) r dr}. \quad (20)$$

The *integrated* metallicity,  $\langle Z_{\text{int}} \rangle$ , that would be measured from a spectroscopic aperture that captures all the light of the galaxy (e.g., Jansen et al. 2000; Moustakas & Kennicutt 2006) follows from equation (20) by letting  $r \rightarrow \infty$ .

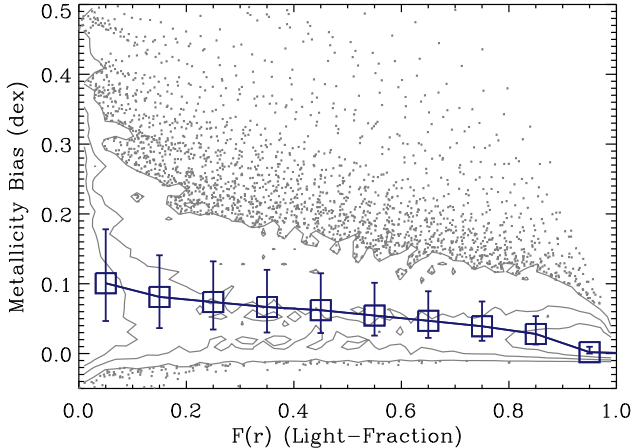


FIG. 21.— Simulated effect of aperture bias on the metallicity inferred from spectra that enclose a fraction of the integrated light of the galaxy (see §7.4 for a complete description of the parameters of the simulation). For a given light-fraction,  $0 < F(r) < 1$ , the abscissa gives the difference between the metallicity one would infer from a spectrum that encloses  $F(r)$  of the total light of the galaxy and the integrated metallicity. The metallicity bias is positive because disk galaxies exhibit radial abundance gradients; therefore, their centers are generally more metal-rich than their outskirts. The contours and small grey points correspond to simulated galaxies with a range of concentrations (Sérsic indices), sizes, and abundance gradient slopes. For reference, the contours enclose 50%, 75%, and 95% of the simulated galaxies and the points are objects that lie outside the 95% contour level. The large blue squares show the median metallicity bias in fixed bins of  $F(r)$ , and the error bars indicate the interquartile range. We find that the metallicity bias is typically  $\lesssim 0.1$  dex, and a relatively weak function of enclosed light fraction.

With these simple ingredients in-hand we can now estimate the relative effects of aperture bias on the inferred metallicities for a wide range of surface-brightness profiles, sizes, and abundance gradients. To constrain the range of  $n$  and  $r_{50}$  we use the distribution of physical properties for late-type galaxies recently compiled by Blanton & Moustakas (2009, see especially §3.1 and Fig. 8 in that review) for SDSS galaxies at  $z < 0.05$ . Specifically, we adopt a normally distributed prior on  $n$  with mean  $\langle n \rangle = 1.8$  and standard deviation  $\sigma_n = 0.6$ , and a log-normal prior on  $r_{50}$  with  $\langle \log(r_{50}) \rangle = 0.35$  kpc and  $\sigma_{\log(r_{50})} = 0.25$  kpc. For the range of abundance gradient slopes we use the recent measurements by Moustakas et al. (2010) based on a sample of 21 nearby disk galaxies; they find typical values  $\langle dZ/dr \rangle = -0.03$  dex  $\text{kpc}^{-1}$  and  $\sigma_{dZ/dr} = 0.02$  dex  $\text{kpc}^{-1}$ . For each mock galaxy, we simulate the effects of metallicity scatter at fixed galactocentric radius (e.g., due to azimuthal metallicity variations) by perturbing the metallicity at each radius by a Gaussian distribution with mean 0.06 dex and standard deviation 0.02 dex (Moustakas et al. 2010). Finally, for each simulated galaxy we compute, as a function of  $r$ , the enclosed light fraction,  $F(r)$ , and the *metallicity bias*,  $\Delta\langle Z(r) \rangle \equiv \langle Z(r) \rangle - \langle Z_{\text{int}} \rangle$ , or the difference between the surface-brightness weighted metallicity at that radius and the integrated metallicity using equations (19) and (20). We perform 1000 Monte Carlo simulations and plot the results in Figure 21.

Figure 21 reveals that, for our fiducial set of simula-

tions, the metallicity bias is typically  $\lesssim 0.1$  dex; moreover, it is a relatively weak function of enclosed light fraction. The principal reason for this result is that, although disk galaxies do indeed possess radial abundance gradients, they are not especially steep in absolute terms (i.e., in dex  $\text{kpc}^{-1}$ ). For example, making the mean abundance gradient slope a factor of three steeper,  $\langle dZ/dr \rangle = -0.09$  dex  $\text{kpc}^{-1}$  (e.g., if abundance gradients were steeper at higher redshift; Boissier & Prantzos 2001), increases the absolute metallicity bias to 0.2 – 0.3 dex for  $F(r) \lesssim 0.5$ , and makes it a much stronger function of light-fraction; however, the *relative* metallicity bias over the relevant range of light-fractions (see Fig. 20) is still  $\lesssim 0.1$  dex. Finally, we tested making our simulated galaxies a factor of 2–3 larger and a factor of 2–3 more concentrated and the basic results do not change. Based on these tests, we conclude that aperture bias should not significantly affect our measurement of the relative change in the abundances of star-forming galaxies from  $z = 0.05 - 0.75$ .

## 8. DISCUSSION

We have measured the evolution of the  $\mathcal{M} - Z$  relation from  $z = 0.05 - 0.75$  using statistically complete samples of star-forming galaxies selected from AGES and the SDSS, carefully accounting for both random and systematic sources of uncertainty. Our analysis has yielded three key results. First, we find that star-forming galaxies obey a well-defined  $\mathcal{M} - Z$  relation over the entire redshift range studied,  $z = 0.05 - 0.75$ . This result is generally consistent with previous measurements of the  $\mathcal{M} - Z$  relation at intermediate redshift, although the size and statistical completeness of our sample places it on a firmer quantitative footing. Second, we find that at fixed stellar mass,  $\mathcal{M} = 10^{10.5} \mathcal{M}_{\odot}$ , the mean metallicity of star-forming galaxies changes by just 30% – 60% since  $z \sim 0.7$ . The factor of two uncertainty on the amount of metallicity evolution is due to the systematic differences in the abundances inferred using the three strong-line calibrations investigated in this paper (KK04, T04, and M91). Finally, we find no statistically significant evidence that the  $\mathcal{M} - Z$  relation evolves in a mass-dependent way over this redshift range for galaxies with  $\mathcal{M} \simeq 10^{9.8} - 10^{11} \mathcal{M}_{\odot}$ .

Despite considerable effort in recent years, a thorough theoretical explanation of the physical origin and evolution of the  $\mathcal{M} - Z$  relation remains elusive. However, models now provide quantitative estimates not only of the  $\mathcal{M} - Z$  relation, but also auxiliary relations between stellar mass, SFR, and gas fraction, that can be utilized in concert to test the underlying model assumptions. Although we postpone a detailed comparison of our results on the evolution of the  $\mathcal{M} - Z$  relation with various theoretical models to a forthcoming paper, a brief discussion of one class models is suggestive of what can be done.

Davé et al. (2011a) have proposed a simple analytic framework for interpreting the  $\mathcal{M} - Z$  relation based on insights gained analyzing a suite of cosmological hydrodynamic simulations with different prescriptions for galactic winds (Davé et al. 2006, 2011b; Oppenheimer & Davé 2008; Finlator & Davé 2008; Oppenheimer et al. 2010). Their central hypothesis is that most galaxies are in a slowly evolving equilibrium with the intergalactic medium (IGM), balanced

between the competing effects of accretion, outflows, and star formation. They derive an expression for the  $\mathcal{M} - Z$  relation given by

$$Z_g = \frac{y}{(1 + \eta)(1 - \alpha_Z)}, \quad (21)$$

where  $\eta$  (the *mass loading factor*) is a proportionality constant relating the outflow-driven mass-loss rate to the instantaneous SFR, and  $\alpha_Z$  is the ratio of the metallicity of the gas being accreted from the IGM relative to the gas-phase metallicity of the galaxy (Finlator & Davé 2008). Their simulations show that a significant fraction of the metals previously ejected from galaxies in star-formation driven outflows are reaccreted in a mass-dependent way (*wind recycling*; Oppenheimer & Davé 2008; Oppenheimer et al. 2010), or  $\alpha_Z > 0$ . The result is an  $\mathcal{M} - Z$  relation whose shape is predominantly determined by the fraction of accreted gas that forms stars (modulated by  $\eta$ ), while its evolution is governed by  $\alpha_Z$ , the relative enrichment level of the infalling gas. Their favored model based on momentum-driven galactic winds (Murray et al. 2005a) grossly reproduces both the shape and evolution of the  $\mathcal{M} - Z$  relation from  $z = 0 - 3$  (with some notable discrepancies; see Davé et al. 2011b for details).

An interesting consequence of this model is that deviations from equilibrium at fixed stellar mass should correlate with metallicity, SFR, and gas fraction. For example, galaxies that have recently accreted significant amounts of cold gas from the IGM should have slightly lower metallicities (via dilution, assuming  $\alpha_Z \sim 0$ ), and should be forming stars at slightly higher rates (due to the renewed gas supply) compared to galaxies of the same stellar mass still at equilibrium. These results provide a compelling physical explanation for the so-called fundamental metallicity relation (Mannucci et al. 2010), which posits that galaxies occupy a three-dimensional plane linking stellar mass, gas-phase metallicity, and SFR. Specifically, the fundamental metallicity relation reveals that at fixed stellar mass, galaxies with high SFRs tend to be metal-poor, while galaxies that lie above the median  $\mathcal{M} - Z$  relation generally have lower SFRs.

This type of comparison can, and will, be done with our SDSS and AGES observations. By incorporating accurate SFRs and approximate gas fractions, the latter of which we intend to estimate by inverting the Kennicutt-Schmidt (Kennicutt 1998c) law (see, e.g., Appendix A in Peeples & Shankar 2011), our analysis will provide powerful new insights into the physical origin and evolution of the  $\mathcal{M} - Z$  relation, and, more generally, on our theoretical understanding of galaxy formation.

We conclude this section with a brief discussion of previous and ongoing efforts to measure the  $\mathcal{M} - Z$  relation at even higher redshift,  $z > 1$ . Abundance studies of star-forming galaxies at these redshifts are especially challenging because they require near-infrared spectroscopy, which remains difficult and time-consuming to obtain from the ground. Nevertheless, building on a handful of pioneering abundance studies of  $z \sim 2$  galaxies (Pettini et al. 1998, 2001; Kobulnicky & Koo 2000; Shapley et al. 2004; Swinbank et al. 2004), measurements of the  $\mathcal{M} - Z$  relation for star-forming galaxies now exist for galaxies at  $1 < z < 1.6$

(Shapley et al. 2005; Maier et al. 2006; Liu et al. 2008; Pérez-Montero et al. 2009; Queyrel et al. 2009), Lyman-break and near-infrared selected galaxies at  $z \sim 2$  (Erb et al. 2006; Hayashi et al. 2009), and star-forming galaxies at redshifts as high as  $z \sim 3.5$  (Maiolino et al. 2008; Mannucci et al. 2009; Lemoine-Busserolle et al. 2010; Richard et al. 2011).

It is instructive to highlight two important, outstanding issues confronting observational abundance studies of star-forming galaxies at  $z > 1$ . First, the availability of different emission lines depending on the redshift range of the sample under investigation and the spectral range of the observations means that metallicities in general cannot be derived using the same strong-line calibration at all redshifts. For example, the abundances of star-forming galaxies at  $z = 1 - 2$  have been based, in most cases, on the N2 and O3N2 diagnostics (see §7.2; e.g., Shapley et al. 2005; Erb et al. 2006; Queyrel et al. 2009, but see Pérez-Montero et al. 2009 for application of the so-called O2Ne3 diagnostic), while the  $R_{23}$  diagnostic has been used for galaxies at  $z = 3 - 3.5$  (Mannucci et al. 2009; Richard et al. 2011). Consequently, efforts to compare the  $\mathcal{M} - Z$  relation for star-forming galaxies at different epochs is complicated by the systematic differences among strong-line abundance calibrations (see the discussion in §7.2). Second, observations suggest that the physical conditions (ionization parameter, electron density or interstellar pressure, prevalence of shocks, etc.) in star-forming galaxies at  $z \gtrsim 1$  may be dramatically different compared to local galaxies (Shapley et al. 2004; Liu et al. 2008; Brinchmann et al. 2008; Lehnert et al. 2009; Hainline et al. 2009). It remains to be seen, therefore, whether using strong-line abundance diagnostics that have been calibrated against H II regions in nearby galaxies introduces systematic errors in the metallicity measurements of high-redshift galaxies.

Addressing these issues requires concerted observational effort on two fronts. First, high-quality observations of H II regions in nearby galaxies, coupled with more detailed photoionization models, are needed to understand the physical origin of the factor of  $\sim 5$  systematic uncertainty in the nebular abundance scale (see the discussion in Moustakas et al. 2010, and references therein). In addition, the effect of secondary nitrogen enrichment on oxygen abundances derived using the N2 and O3N2 abundance diagnostics must be better understood (Yin et al. 2007; Pérez-Montero & Contini 2009; Thuan et al. 2010). And second, dedicated optical and near-infrared spectroscopic observing campaigns of large samples of higher redshift galaxies are needed to measure the full suite of rest-frame optical emission-line diagnostics. In particular, the advent of highly multiplexed near-infrared spectrographs on 8 - 10-m class telescopes like LBT/LUCIFER (Mandel et al. 2000), Keck/MOSFIRE (McLean et al. 2008), GTC/EMIR (Garzon et al. 2003) will facilitate the kinds of detailed studies that until recently have only been possible for lower-redshift galaxies.

## 9. SUMMARY

We have measured the gas-phase oxygen abundances, stellar masses, and  $B$ -band luminosities of  $\sim 3000$  star-forming galaxies at  $z = 0.05 - 0.75$  observed as part of AGES, a redshift survey of  $I_{AB} < 20.45$  galaxies over  $7.9 \text{ deg}^2$  in the NDWFS Boötes field. This sam-



ple is among the largest statistically complete, wide-area samples of intermediate-redshift galaxies with measured nebular abundances assembled. We use state-of-the-art techniques coupled to high-resolution population synthesis models to measure the nebular emission lines free from the systematic effects of underlying stellar absorption. In addition, we model the observed deep, aperture-matched broadband optical and near-infrared photometry of the galaxies in our sample using `iSEDfit`, a new Bayesian SED-fitting code, to infer their stellar masses. Using multiple complementary multiwavelength diagnostics based on optical line-ratios and ancillary X-ray, mid-infrared, and radio observations, we identify and remove AGN from our sample. We combine volume-limited observations from AGES with a complementary, statistically complete sample of  $\sim 75,000$  star-forming galaxies at  $z = 0.05 - 0.2$  selected from the SDSS, which we analyze in the identical manner. We use the joint SDSS and AGES sample to measure the evolution of the  $\mathcal{M} - Z$  and  $B$ -band  $L - Z$  relations between  $z = 0.05$  and  $z = 0.75$  using three independent strong-abundance calibrations (KK04, T04, and M91) of the metallicity-sensitive  $R_{23}$  parameter.

We divide our principal findings into two categories, lessons learned and quantitative results. Among the lessons we have learned:

1. EWs provide a powerful, reliable means of inferring oxygen abundances from nebular emission lines free from the systematic effects of dust attenuation. They also have the added advantage of being measureable in spectra that have not been flux-calibrated, although it is critical that the emission lines, especially  $H\beta$ , be corrected for underlying stellar absorption.
2. A thorough culling of AGN is necessary to ensure that metallicities derived using the  $R_{23}$  parameter are not spuriously underestimated; the metallicity bias for galaxies with a subdominant ( $\lesssim 30\%$ ) contribution from an AGN is typically  $\lesssim 0.1$  dex, but can be  $\gg 0.2$  dex for powerful AGN.
3. We find that aperture effects are not a significant source of systematic error in the gas-phase metallicities derived from fiber-optic spectroscopic surveys like the SDSS and AGES, owing to the relatively shallow radial abundance gradients in disk galaxies.
4. The choice of strong-line calibration significantly affects not only the absolute normalization and shape of the  $\mathcal{M} - Z$  relation, but also the *rate* of chemical evolution inferred, and its stellar mass dependence. Consequently, we caution strongly against comparing the metallicity measurements across redshifts based on different emission-line ratios (see especially the discussion in §7.2).
5. We propose a new, physically motivated parametric model for the  $\mathcal{M} - Z$  relation given by equation (10). This parameterization has the same number of free parameters as the more commonly used polynomial model but has whose asymptotic behavior is much more stable.
6. We confirm that stellar mass provides a much less ambiguous measurement of metallicity evolution than optical luminosity, which itself evolves strongly. The  $B$ -band  $L - Z$  relation in particular does not provide a reliable means of constraining the chemical evolution of star-forming galaxies.

And our principal quantitative conclusions are:

1. We find no statistically significant evidence for evolution in the shape of the  $\mathcal{M} - Z$  relation for  $z = 0.75$  for  $\mathcal{M} \simeq 10^{9.8} - 10^{11} \mathcal{M}_{\odot}$  star-forming galaxies, contrary to previous findings based on smaller, incomplete samples.
2. We find only modest evolution in the overall normalization of the  $\mathcal{M} - Z$  relation, suggesting a metallicity increase of between 30%–60% for  $\mathcal{M} \simeq 10^{9.8} - 10^{11} \mathcal{M}_{\odot}$  galaxies since  $z = 0.75$ . The uncertainty in our measurement is entirely due to the choice of strong-line calibration.

Our results indicate that massive star-forming galaxies at intermediate redshift are chemically evolved, implying that they synthesized the bulk of their metals at higher redshift,  $z > 1$ . Given their stellar masses, this result is perhaps not too surprising. On the other hand, a challenge for theoretical galaxy formation models that incorporate chemical evolution will be to explain not only the relatively slow chemical enrichment rate for star-forming galaxies over this redshift range, but also the lack of evolution in the *shape* of the  $\mathcal{M} - Z$  relation. In a forthcoming paper we will combine our metallicity and stellar mass estimates with SFRs and approximate gas fractions to directly test the predictions of several of these theoretical models (e.g., Brooks et al. 2007; Davé et al. 2011a; Peeples & Shankar 2011).

On the observational side, joint optical and near-IR spectroscopy of intermediate-redshift star-forming galaxies would be especially useful. These observations would provide the full suite of rest-frame optical emission-line diagnostics, from  $[O\ II] \lambda 3727$  to  $H\alpha$  and  $[N\ II] \lambda\lambda 6548, 6584$ , thereby enabling optical AGN to be identified more securely, and allowing gas-phase metallicities to be estimated using multiple independent strong-line abundance calibrations. Finally, abundance studies of statistically complete samples of intermediate-redshift galaxies spanning a wider range of stellar masses,  $10^8 - 10^{11} \mathcal{M}_{\odot}$ , should be a top priority (e.g., Zahid et al. 2011). Follow-up high-resolution optical and near-IR spectroscopy of lower-mass galaxies preselected from the latest generation of wide-area galaxy redshift surveys like GAMA (Driver et al. 2011), zCOSMOS (Lilly et al. 2009), and PRIMUS (Coil et al. 2011) would be one path forward. These abundance measurements, coupled with detailed stellar masses and SFRs, would provide valuable insight into the star formation and chemical enrichment histories of star-forming galaxies over a significant fraction of the age of the Universe.

This paper has benefited from insightful suggestions, discussions, and encouragement from James Aird, Roberto Assef, Michael Blanton, Alison Coil, Aleks



Diamond-Stanic, Ryan Hickox, David Hogg, Robert Kenicutt, Alexander Mendez, Leonidas Moustakas, Casey Papovich, and Christy Tremonti. We gratefully acknowledge the MMT staff and Hectospec instrument team for their help in carrying out the AGES survey, and J. M. acknowledges financial support through the National Science Foundation grant AST-0908246. We kindly thank Len Cowie for providing an electronic table of the metallicity measurements from Cowie & Barger (2008) shown in Figure 18, and Fuyan Bian and Xiaohui Fan for providing access to their LBT/LBC  $U$ -band imaging of the Boötes field.

Observations reported here were obtained at the MMT Observatory, a joint facility of the Smithsonian Institution and the University of Arizona. This work made use of images and/or data products provided by the NOAO Deep Wide-Field Survey (Jannuzi & Dey 1999), which is supported by the National Optical Astronomy Observatory (NOAO). NOAO is operated by AURA, Inc., under a cooperative agreement with the National Science Foundation. This work is based in part on observations made with the *Spitzer Space Telescope*, which is operated by the Jet Propulsion Laboratory, California Institute of Technology under a contract with NASA. Support for this work was provided by NASA through an award issued by JPL/Caltech. The X-ray data were obtained using the Chandra X-ray Observatory operated by the Chandra X-ray Center at the Harvard-Smithsonian Cen-

ter for Astrophysics, funded by NASA COntract NAS8-03060.

Funding for the Sloan Digital Sky Survey (SDSS) and SDSS-II has been provided by the Alfred P. Sloan Foundation, the Participating Institutions, the National Science Foundation, the U.S. Department of Energy, the National Aeronautics and Space Administration, the Japanese Monbukagakusho, and the Max Planck Society, and the Higher Education Funding Council for England. The SDSS Web site is <http://www.sdss.org>.

The SDSS is managed by the Astrophysical Research Consortium (ARC) for the Participating Institutions. The Participating Institutions are the American Museum of Natural History, Astrophysical Institute Potsdam, University of Basel, University of Cambridge, Case Western Reserve University, The University of Chicago, Drexel University, Fermilab, the Institute for Advanced Study, the Japan Participation Group, The Johns Hopkins University, the Joint Institute for Nuclear Astrophysics, the Kavli Institute for Particle Astrophysics and Cosmology, the Korean Scientist Group, the Chinese Academy of Sciences (LAMOST), Los Alamos National Laboratory, the Max-Planck-Institute for Astronomy (MPIA), the Max-Planck-Institute for Astrophysics (MPA), New Mexico State University, Ohio State University, University of Pittsburgh, University of Portsmouth, Princeton University, the United States Naval Observatory, and the University of Washington.

*Facilities:* MMT, Spitzer, Chandra, Mayall, LBT

## APPENDIX

### A. ABUNDANCE CALIBRATIONS

For completeness and the convenience of the reader, we describe and compare the three strong-line calibrations adopted in this paper. For the KK04 calibration, we have

$$12 + \log(\text{O}/\text{H})_{\text{KK04,lower}} = 9.4 + 4.65x - 3.17x^2 - \log(q) (0.272 + 0.547x - 0.513x^2), \quad (\text{A1})$$

and

$$12 + \log(\text{O}/\text{H})_{\text{KK04,upper}} = 9.72 - 0.777x - 0.951x^2 - 0.072x^3 - 0.811x^4 - \log(q) (0.0737 - 0.0713x - 0.141x^2 + 0.0373x^3 - 0.058x^4), \quad (\text{A2})$$

for galaxies on the lower and upper branch, respectively, where  $x \equiv \log(R_{23})$ . The ionization parameter  $q$  in  $\text{cm s}^{-1}$  is given by

$$\log(q) = 32.81 - 1.153y^2 + z(-3.396 - 0.025y + 0.1444y^2) \times [4.603 - 0.3119y - 0.163y^2 + z(-0.48 + 0.0271y + 0.02037y^2)]^{-1}, \quad (\text{A3})$$

where  $z \equiv 12 + \log(\text{O}/\text{H})$  and  $y \equiv \log(O_{32})$  characterizes the hardness of the ionizing radiation field. The ionization parameter is also frequently written as a dimensionless quantity  $U \equiv q/c$ , where  $c = 2.99 \times 10^{10} \text{ cm s}^{-1}$  is the speed-of-light (Shields 1990; Kewley & Dopita 2002). Note that equations (A1)-(A3) must be solved iteratively for both the ionization parameter and the oxygen abundance; convergence is typically achieved in a handful of iterations.

For the M91 calibration, we adopt the parameterizations proposed by Kobulnicky et al. (1999), but see Kuzio de Naray et al. (2004) for alternative parameterizations based on trigonometric functions. For the lower branch, we have

$$12 + \log(\text{O}/\text{H})_{\text{M91,lower}} = 12 - 4.944 + 0.767x + 0.602x^2 - y(0.29 + 0.332x - 0.331x^2), \quad (\text{A4})$$

and for the upper branch we have

$$12 + \log(\text{O}/\text{H})_{\text{M91,upper}} = 12 - 2.939 - 0.2x - 0.237x^2 - 0.305x^3 - 0.0283x^4 - y(0.0047 - 0.0221x - 0.102x^2 - 0.0817x^3 - 0.00717x^4). \quad (\text{A5})$$

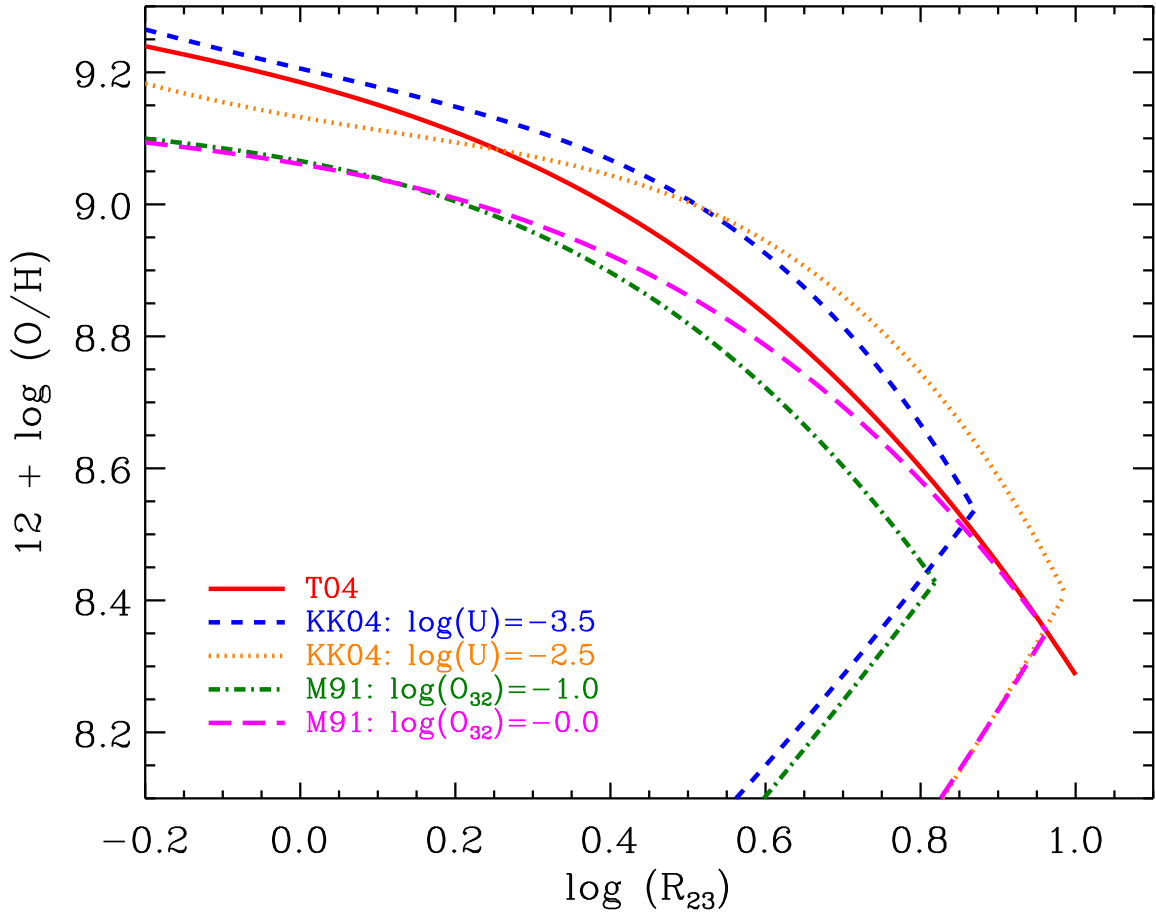


FIG. A1.— Relationship between  $R_{23}$  and oxygen abundance for the three theoretical strong-line abundance calibrations adopted in this paper: T04 (solid red curve); KK04 (short-dashed blue and dotted orange curve, corresponding to  $\log(U) = -3.5$  and  $-2.5$ , respectively); and M91 (dot-dashed green and long-dashed purple curve, corresponding to  $\log(O_{32}) = -1.0$  and  $0.0$ , respectively).

And finally the T04 calibration is only defined for galaxies on the upper  $R_{23}$  branch:

$$12 + \log(O/H)_{\text{T04,upper}} = 9.185 - 0.313x - 0.264x^2 - 0.321x^3 \quad (\text{A6})$$

In Figure A1 we compare the three separate strong-line calibrations for two values of the ionization parameters  $U$  and  $O_{32}$ .

## B. PROPOSED NEW FUNCTIONAL FORM FOR THE $\mathcal{M} - Z$ RELATION

Previous studies have parameterized the  $\mathcal{M} - Z$  relation using a quadratic or third-order polynomial (e.g., Tremonti et al. 2004; Kewley & Ellison 2008). A polynomial model is unsatisfactory, however, because it can lead to an  $\mathcal{M} - Z$  relation that *decreases* with increasing mass (see, e.g., Fig. 2 of Kewley & Ellison 2008). This artificial turn-over in the polynomial  $\mathcal{M} - Z$  relation is especially problematic when the model is extrapolated beyond the range of stellar masses for which it was calibrated. Therefore, in §6.1.1 we fit the local  $\mathcal{M} - Z$  relation with a new functional form, which we reproduce here for the convenience of the reader:

$$12 + \log(O/H) = 12 + \log(O/H)^* - \log \left[ 1 + \left( \frac{\mathcal{M}^*}{10^9 \mathcal{M}_\odot} \right)^\gamma \right]. \quad (\text{B1})$$

Unlike the polynomial model, this parameterization encapsulates our physical intuition that the  $\mathcal{M} - Z$  relation should vary monotonically with stellar mass. In our proposed model,  $\mathcal{M}^*$  refers to the stellar mass where the  $\mathcal{M} - Z$  relation begins to bend or flatten at a rate that is controlled by the power-law slope,  $\gamma$ . For example, an  $\mathcal{M} - Z$  relation with  $\gamma \ll 1$  remains steep well above  $\mathcal{M}^*$ , while an  $\mathcal{M} - Z$  relation with  $\gamma \gg 1$  is essentially flat for  $\mathcal{M} > \mathcal{M}^*$ . The parameter  $12 + \log(O/H)^*$  is the asymptotic metallicity of the  $\mathcal{M} - Z$  relation, i.e., the metallicity for galaxies with  $\mathcal{M} \gg \mathcal{M}^*$ .

The form and asymptotic limit of our model is motivated by the closed-box equations of chemical evolution (Talbot & Arnett 1971; Binney & Merrifield 1998). If the SFR declines exponentially with a characteristic timescale  $\tau$ ,  $\psi(t) \propto \exp(-t/\tau)$ , then it is straightforward to show that the gas-phase metallicity at time  $t$ ,  $Z(t)$ , is given by

$$Z(t) = -y \ln[1 - (1 - R)(1 - \exp^{-t/\tau})], \quad (\text{B2})$$

where  $y$  is the nucleosynthetic yield, and  $R$  is the *return fraction*, the fraction of mass returned by stars to the interstellar medium by supernovae and stellar winds (Pagel 1997).<sup>32</sup> Note that in the absence of inflow and outflow, the return fraction simply equals the baryonic gas fraction. In the limit  $t \gg \tau$  equation (B2) becomes  $Z = -y \ln(R)$ , i.e., the gas-phase metallicity becomes a constant equal to a fraction of the yield, which is analogous to our characteristic metallicity,  $12 + \log(\text{O}/\text{H})^*$ .

In addition to equation (B1) and the traditional polynomial parameterization of the  $\mathcal{M} - Z$  relation, we also investigated a smooth double power-law model, which is commonly used to fit the X-ray and infrared luminosity functions (e.g. Aird et al. 2008; Rujopakarn et al. 2010), and a broken double power-law. Unfortunately, the double power-law model exhibits the same general behavior as the polynomial model (i.e., it turns over rapidly at large stellar mass), while the broken power-law has a sharp, artificial break with no physical basis.

## REFERENCES

- Abazajian, K., et al. 2004, *AJ*, 128, 502  
 Adelman-McCarthy, J. K., Agüeros, M. A., Allam, S. S., et al. 2008, *ApJS*, 175, 297  
 Aird, J., Nandra, K., Georgakakis, A., et al. 2008, *MNRAS*, 387, 883  
 Aller, L. H. 1942, *ApJ*, 95, 52  
 Asari, N. V., Cid Fernandes, R., Stasińska, G., et al. 2007, *MNRAS*, 381, 263  
 Ashby, M. L. N., Stern, D., Brodwin, M., et al. 2009, *ApJ*, 701, 428  
 Asplund, M., Grevesse, N., Sauval, A. J., & Scott, P. 2009, *ARA&A*, 47, 481  
 Assef, R. J., Kochanek, C. S., Ashby, M. L. N., et al. 2011, *ApJ*, 728, 56  
 Auger, M. W., Treu, T., Bolton, A. S., et al. 2009, *ApJ*, 705, 1099  
 Autry, R. G., Probst, R. G., Starr, B. M., et al. 2003, in Presented at the Society of Photo-Optical Instrumentation Engineers (SPIE) Conference, Vol. 4841, Society of Photo-Optical Instrumentation Engineers (SPIE) Conference Series, ed. M. Iye & A. F. M. Moorwood, 525–539  
 Baldwin, J. A., Phillips, M. M., & Terlevich, R. 1981, *PASP*, 93, 5  
 Bastian, N., Covey, K. R., & Meyer, M. R. 2010, *ARA&A*, 48, 339  
 Bell, E. F., & de Jong, R. S. 2001, *ApJ*, 550, 212  
 Bell, E. F., Papovich, C., Wolf, C., et al. 2005, *ApJ*, 625, 23  
 Bertin, E., & Arnouts, S. 1996, *A&AS*, 117, 393  
 Bessell, M. S. 1990, *PASP*, 102, 1181  
 Binney, J., & Merrifield, M. 1998, *Galactic astronomy (Galactic astronomy / James Binney and Michael Merrifield. Princeton, NJ : Princeton University Press, 1998. (Princeton series in astrophysics) QB857 .B522 1998 (\$35.00))*  
 Blanton, M. R. 2006, *ApJ*, 648, 268  
 Blanton, M. R., & Moustakas, J. 2009, *ARA&A*, 47, 159  
 Blanton, M. R., & Roweis, S. 2007, *AJ*, 133, 734  
 Blanton, M. R., Brinkmann, J., Csabai, I., et al. 2003, *AJ*, 125, 2348  
 Blanton, M. R., Schlegel, D. J., Strauss, M. A., et al. 2005, *AJ*, 129, 2562  
 Boissier, S., & Prantzos, N. 2001, *MNRAS*, 325, 321  
 Brand, K., Brown, M. J. I., Dey, A., et al. 2006, *ApJ*, 641, 140  
 Bresolin, F. 2007, *ApJ*, 656, 186  
 Bresolin, F., Garnett, D. R., & Kennicutt, R. C. 2004, *ApJ*, 615, 228  
 Bresolin, F., Gieren, W., Kudritzki, R., et al. 2009, *ApJ*, 700, 309  
 Bresolin, F., Schaerer, D., González Delgado, R. M., & Stasińska, G. 2005, *A&A*, 441, 981  
 Brinchmann, J., Charlot, S., White, S. D. M., et al. 2004, *MNRAS*, 351, 1151  
 Brinchmann, J., Pettini, M., & Charlot, S. 2008, *MNRAS*, 385, 769  
 Brooks, A. M., Governato, F., Booth, C. M., et al. 2007, *ApJ*, 655, L17  
 Brown, M. J. I., Dey, A., Jannuzi, B. T., et al. 2007, *ApJ*, 654, 858  
 —. 2003, *ApJ*, 597, 225  
 Brown, M. J. I., Zheng, Z., White, M., et al. 2008, *ApJ*, 682, 937  
 Bruzual, G. 2007, in *Astronomical Society of the Pacific Conference Series, Vol. 374, From Stars to Galaxies: Building the Pieces to Build Up the Universe*, ed. A. Vallenari, R. Tantalo, L. Portinari, & A. Moretti, 303–+  
 Bruzual, G., & Charlot, S. 2003, *MNRAS*, 344, 1000  
 Calura, F., Pipino, A., Chiappini, C., Matteucci, F., & Maiolino, R. 2009, *A&A*, 504, 373  
 Calzetti, D. 2001, *PASP*, 113, 1449  
 Calzetti, D., Armus, L., Bohlin, R. C., et al. 2000, *ApJ*, 533, 682  
 Calzetti, D., Kinney, A. L., & Storchi-Bergmann, T. 1994, *ApJ*, 429, 582  
 Cappellari, M., & Emsellem, E. 2004, *PASP*, 116, 138  
 Carollo, C. M., & Lilly, S. J. 2001, *ApJ*, 548, L153  
 Chabrier, G. 2003, *PASP*, 115, 763  
 Charlot, S., & Fall, S. M. 2000, *ApJ*, 539, 718  
 Charlot, S., & Longhetti, M. 2001, *MNRAS*, 323, 887  
 Cid Fernandes, R., Asari, N. V., Sodré, L., et al. 2007, *MNRAS*, 375, L16  
 Cid Fernandes, R., Mateus, A., Laerte, S. J., Stasińska, G., & Gomes, J. M. 2005, *MNRAS*, 358, 363  
 Civano, F., Mignoli, M., Comastri, A., et al. 2007, *A&A*, 476, 1223  
 Coil, A. L., Newman, J. A., Croton, D., et al. 2008, *ApJ*, 672, 153  
 Coil, A. L., Blanton, M. R., Burles, S. M., et al. 2011, *ApJ*, 741, 8  
 Comastri, A., Mignoli, M., Ciliegi, P., et al. 2002, *ApJ*, 571, 771  
 Conroy, C., & Gunn, J. E. 2010, *ApJ*, 712, 833  
 Conroy, C., Gunn, J. E., & White, M. 2009, *ApJ*, 699, 486  
 Contini, T., Treyer, M. A., Sullivan, M., & Ellis, R. S. 2002, *MNRAS*, 330, 75  
 Cool, R. J. 2007, *ApJS*, 169, 21  
 Cool, R. J., et al. 2011, *ApJ*, submitted  
 Cooper, M. C., Tremonti, C. A., Newman, J. A., & Zabludoff, A. I. 2008, *MNRAS*, 1037  
 Cowie, L. L., & Barger, A. J. 2008, *ApJ*, 686, 72  
 Cresci, G., Mannucci, F., Sommariva, V., et al. 2011, *ArXiv e-prints*  
 Dalcanton, J. J. 2007, *ApJ*, 658, 941  
 Davé, R., Finlator, K., & Oppenheimer, B. D. 2006, *MNRAS*, 370, 273  
 —. 2011a, *ArXiv e-prints*  
 —. 2011b, *MNRAS*, 416, 1354  
 Davis, M., Faber, S. M., Newman, J., et al. 2003, in *Discoveries and Research Prospects from 6- to 10-Meter-Class Telescopes II. Edited by Guhathakurta, Puragra. Proceedings of the SPIE, Volume 4834, pp. 161-172 (2003).*, 161–172  
 Davis, M., Guhathakurta, P., Konidaris, N. P., et al. 2007, *ApJ*, 660, L1  
 De Lucia, G., Kauffmann, G., & White, S. D. M. 2004, *MNRAS*, 349, 1101  
 de Vaucouleurs, G. 1948, *Annales d'Astrophysique*, 11, 247  
 de Vries, W. H., Morganti, R., Röttgering, H. J. A., et al. 2002, *AJ*, 123, 1784  
 Denicoló, G., Terlevich, R., & Terlevich, E. 2002, *MNRAS*, 330, 69  
 Dessauges-Zavadsky, M., Pindao, M., Maeder, A., & Kunth, D. 2000, *A&A*, 355, 89  
 Dinerstein, H. L. 1990, in *Astrophysics and Space Science Library, Vol. 161, The Interstellar Medium in Galaxies*, ed. H. A. Thronson Jr. & J. M. Shull, 257–285  
 Driver, S. P., Hill, D. T., Kelvin, L. S., et al. 2011, *MNRAS*, 413, 971  
 Dutton, A. A., & van den Bosch, F. C. 2009, *MNRAS*, 396, 141

<sup>32</sup> In detail, the return fraction is also a function of time (Leitner 2011), although we ignore its time-dependence here.

- Dutton, A. A., van den Bosch, F. C., & Dekel, A. 2010, *MNRAS*, 405, 1690
- Edmunds, M. G., & Pagel, B. E. J. 1984, *MNRAS*, 211, 507
- Elbaz, D., Daddi, E., Le Borgne, D., et al. 2007, *A&A*, 468, 33
- Ellison, S. L., Patton, D. R., Nair, P., et al. 2011, *ArXiv e-prints*
- Ellison, S. L., Patton, D. R., Simard, L., & McConnell, A. W. 2008a, *ApJ*, 672, L107
- 2008b, *AJ*, 135, 1877
- Ellison, S. L., Simard, L., Cowan, N. B., et al. 2009, *MNRAS*, 396, 1257
- Erb, D. K., Shapley, A. E., Pettini, M., et al. 2006, *ApJ*, 644, 813
- Esteban, C., Bresolin, F., Peimbert, M., et al. 2009, *ApJ*, 700, 654
- Faber, S. M., Willmer, C. N. A., Wolf, C., et al. 2007, *ApJ*, 665, 265
- Fabricant, D., Fata, R., Roll, J., et al. 2005, *PASP*, 117, 1411
- Fabricant, D. G., Hertz, E. N., Szentgyorgyi, A. H., et al. 1998, in *Proc. SPIE Vol. 3355*, p. 285-296, *Optical Astronomical Instrumentation*, Sandro D'Odorico; Ed., 285-296
- Fabricant, D. G., Kurtz, M. J., Geller, M. J., et al. 2008, *PASP*, 120, 1222
- Faucher-Giguère, C.-A., Kereš, D., & Ma, C.-P. 2011, *MNRAS*, 417, 2982
- Fazio, G. G., Hora, J. L., Allen, L. E., et al. 2004, *ApJS*, 154, 10
- Finlator, K., & Davé, R. 2008, *MNRAS*, 385, 2181
- Gallazzi, A., Charlot, S., Brinchmann, J., White, S. D. M., & Tremonti, C. A. 2005, *MNRAS*, 362, 41
- Garcia-Appadoo, D. A., West, A. A., Dalcanton, J. J., Cortese, L., & Disney, M. J. 2009, *MNRAS*, 394, 340
- Garilli, B., Le Fèvre, O., Guzzo, L., et al. 2008, *A&A*, 486, 683
- Garnett, D. R. 2002, *ApJ*, 581, 1019
- Garnett, D. R. 2004, in *Cosmochemistry. The melting pot of the elements*, ed. C. Esteban, R. García López, A. Herrero, & F. Sánchez, 171-216
- Garnett, D. R., & Shields, G. A. 1987, *ApJ*, 317, 82
- Garnett, D. R., Shields, G. A., Skillman, E. D., Sagan, S. P., & Dufour, R. J. 1997, *ApJ*, 489, 63
- Garzon, F., Barrera, S., Correa, S., et al. 2003, in *Society of Photo-Optical Instrumentation Engineers (SPIE) Conference Series*, Vol. 4841, *Society of Photo-Optical Instrumentation Engineers (SPIE) Conference Series*, ed. M. Iye & A. F. M. Moorwood, 1539-1547
- Geha, M., Blanton, M. R., Masjedi, M., & West, A. A. 2006, *ApJ*, 653, 240
- Georgakakis, A. E., Chavushyan, V., Plionis, M., et al. 2006, *MNRAS*, 367, 1017
- Giallongo, E., Ragazzoni, R., Grazian, A., et al. 2008, *A&A*, 482, 349
- Giavalisco, M., Ferguson, H. C., Koekemoer, A. M., et al. 2004, *ApJ*, 600, L93
- Gilbank, D. G., Baldry, I. K., Balogh, M. L., Glazebrook, K., & Bower, R. G. 2010, *MNRAS*, 405, 2594
- Girardi, L., Bressan, A., Chiosi, C., Bertelli, G., & Nasi, E. 1996, *A&AS*, 117, 113
- Gorjian, V., Brodwin, M., Kochanek, C. S., et al. 2008, *ApJ*, 679, 1040
- Graham, A. W. 2001, *AJ*, 121, 820
- Graham, A. W., & Driver, S. P. 2005, *PASA*, 22, 118
- Grillo, C., Gobat, R., Lombardi, M., & Rosati, P. 2009, *A&A*, 501, 461
- Hainline, K. N., Shapley, A. E., Kornei, K. A., et al. 2009, *ApJ*, 701, 52
- Hayashi, M., Motohara, K., Shimasaku, K., et al. 2009, *ApJ*, 691, 140
- Hickox, R. C., Jones, C., Forman, W. R., et al. 2007, *ApJ*, 671, 1365
- 2009, *ApJ*, 696, 891
- Hogg, D. W., Baldry, I. K., Blanton, M. R., & Eisenstein, D. J. 2002, *ArXiv Astrophysics e-prints*
- Ilbert, O., Tresse, L., Zucca, E., et al. 2005, *A&A*, 439, 863
- Isobe, T., Feigelson, E. D., Akritas, M. G., & Babu, G. J. 1990, *ApJ*, 364, 104
- Ivezić, Ž., Lupton, R. H., Schlegel, D., et al. 2004, *Astronomische Nachrichten*, 325, 583
- Izotov, Y. I., Stasińska, G., Meynet, G., Guseva, N. G., & Thuan, T. X. 2006, *A&A*, 448, 955
- Izotov, Y. I., & Thuan, T. X. 1998, *ApJ*, 500, 188
- Jannuzi, B. T., & Dey, A. 1999, in *ASP Conf. Ser. 191: Photometric Redshifts and the Detection of High Redshift Galaxies*, 111-+
- Jansen, R. A., Fabricant, D., Franx, M., & Caldwell, N. 2000, *ApJS*, 126, 331
- Jarrett, T. H., Chester, T., Cutri, R., et al. 2000, *AJ*, 119, 2498
- Juneau, S., Dickinson, M., Alexander, D. M., & Salim, S. 2011, *ApJ*, 736, 104
- Kannappan, S. J., & Gawiser, E. 2007, *ApJ*, 657, L5
- Kauffmann, G., Heckman, T. M., & Best, P. N. 2008, *MNRAS*, 384, 953
- Kauffmann, G., Heckman, T. M., White, S. D. M., et al. 2003a, *MNRAS*, 341, 33
- 2003b, *MNRAS*, 341, 54
- Kauffmann, G., Heckman, T. M., Tremonti, C., et al. 2003c, *MNRAS*, 346, 1055
- Kennicutt, R. 1998a, in *Liege International Astrophysical Colloquia*, ed. B. Kaldeich, 81-+
- Kennicutt, R. C. 1992, *ApJ*, 388, 310
- 1998b, *ARA&A*, 36, 189
- 1998c, *ApJ*, 498, 541
- Kennicutt, R. C., Bresolin, F., & Garnett, D. R. 2003, *ApJ*, 591, 801
- Kennicutt, R. C., Tamblyn, P., & Congdon, C. E. 1994, *ApJ*, 435, 22
- Kennicutt, R. C., Hao, C., Calzetti, D., et al. 2009, *ApJ*, 703, 1672
- Kenter, A., Murray, S. S., Forman, W. R., et al. 2005, *ApJS*, 161, 9
- Kewley, L. J., & Dopita, M. A. 2002, *ApJS*, 142, 35
- Kewley, L. J., Dopita, M. A., Sutherland, R. S., Heisler, C. A., & Trevena, J. 2001, *ApJ*, 556, 121
- Kewley, L. J., & Ellison, S. L. 2008, *ApJ*, 681, 1183
- Kewley, L. J., Jansen, R. A., & Geller, M. J. 2005, *PASP*, 117, 227
- Kniazev, A. Y., Pustilnik, S. A., Grebel, E. K., Lee, H., & Pramskij, A. G. 2004, *ApJS*, 153, 429
- Kobayashi, C., Springel, V., & White, S. D. M. 2007, *MNRAS*, 376, 1465
- Kobulnicky, H. A., Kennicutt, R. C., & Pizagno, J. L. 1999, *ApJ*, 514, 544
- Kobulnicky, H. A., & Kewley, L. J. 2004, *ApJ*, 617, 240
- Kobulnicky, H. A., & Koo, D. C. 2000, *ApJ*, 545, 712
- Kobulnicky, H. A., & Phillips, A. C. 2003, *ApJ*, 599, 1031
- Kobulnicky, H. A., & Zaritsky, D. 1999, *ApJ*, 511, 118
- Kochanek, C. S., Pahre, M. A., Falco, E. E., et al. 2001, *ApJ*, 560, 566
- Kochanek, C. S., Eisenstein, D. J., Cool, R. J., et al. 2011, *ArXiv e-prints*
- Konishi, M., Akiyama, M., Kajisawa, M., et al. 2011, *PASJ*, 63, 363
- Köppen, J., & Edmunds, M. G. 1999, *MNRAS*, 306, 317
- Köppen, J., Weidner, C., & Kroupa, P. 2007, *MNRAS*, 375, 673
- Kron, R. G. 1980, *ApJS*, 43, 305
- Kroupa, P. 2001, *MNRAS*, 322, 231
- Kuzio de Naray, R., McGaugh, S. S., & de Blok, W. J. G. 2004, *MNRAS*, 355, 887
- Lamareille, F. 2010, *A&A*, 509, A53+
- Lamareille, F., Mouhcine, M., Contini, T., Lewis, I., & Maddox, S. 2004, *MNRAS*, 350, 396
- Lamareille, F., Brinchmann, J., Contini, T., et al. 2009, *A&A*, 495, 53
- Lara-López, M. A., Bongiovanni, A., Cepa, J., et al. 2010a, *A&A*, 519, A31+
- Lara-López, M. A., Cepa, J., Bongiovanni, A., et al. 2010b, *A&A*, 521, L53+
- Larson, R. B. 1974, *MNRAS*, 169, 229
- Le Borgne, J.-F., Bruzual, G., Pelló, R., et al. 2003, *A&A*, 402, 433
- Le Fèvre, O., Vettolani, G., Paltani, S., et al. 2004, *A&A*, 428, 1043
- Le Fèvre, O., Vettolani, G., Garilli, B., et al. 2005, *A&A*, 439, 845
- Le Floch, E., Papovich, C., Dole, H., et al. 2005, *ApJ*, 632, 169
- Lee, H., Skillman, E. D., Cannon, J. M., et al. 2006, *ApJ*, 647, 970
- Lee, J. C., Salzer, J. J., & Melbourne, J. 2004, *ApJ*, 616, 752
- Lehnert, M. D., Nesvadba, N. P. H., Tiran, L. L., et al. 2009, *ApJ*, 699, 1660
- Leitner, S. N. 2011, *ArXiv e-prints*
- Lemoine-Busserolle, M., Bunker, A., Lamareille, F., & Kissler-Patig, M. 2010, *MNRAS*, 401, 1657
- Lequeux, J., Peimbert, M., Rayo, J. F., Serrano, A., & Torres-Peimbert, S. 1979, *A&A*, 80, 155
- Liang, Y. C., Hammer, F., & Flores, H. 2006a, *A&A*, 447, 113
- Liang, Y. C., Hammer, F., Flores, H., Gruel, N., & Assémat, F. 2004, *A&A*, 417, 905
- Liang, Y. C., Hammer, F., & Yin, S. Y. 2007, *ArXiv e-prints*, 708
- Liang, Y. C., Yin, S. Y., Hammer, F., et al. 2006b, *ApJ*, 652, 257
- Liang, Y. C., Zhong, G. H., Hammer, F., et al. 2010, *MNRAS*, 409, 213
- Lilly, S. J., Carollo, C. M., & Stockton, A. N. 2003, *ApJ*, 597, 730
- Lilly, S. J., Le Brun, V., Maier, C., et al. 2009, *ApJS*, 184, 218
- Liu, X., Shapley, A. E., Coil, A. L., Brinchmann, J., & Ma, C.-P. 2008, *ApJ*, 678, 758
- Lopez-Sanchez, A. R., & Esteban, C. 2010, *ArXiv e-prints*
- Maier, C., Lilly, S. J., Carollo, C. M., et al. 2006, *ApJ*, 639, 858
- Maier, C., Lilly, S. J., Carollo, C. M., Stockton, A., & Brodwin, M. 2005, *ApJ*, 634, 849



- Maier, C., Meisenheimer, K., & Hippelein, H. 2004, *A&A*, 418, 475
- Maiolino, R., Nagao, T., Grazian, A., et al. 2008, *A&A*, 488, 463
- Mandel, H., Appenzeller, I., Bomans, D., et al. 2000, in *Society of Photo-Optical Instrumentation Engineers (SPIE) Conference Series*, Vol. 4008, *Society of Photo-Optical Instrumentation Engineers (SPIE) Conference Series*, ed. M. Iye & A. F. Moorwood, 767–777
- Mannucci, F., Cresci, G., Maiolino, R., Marconi, A., & Gnerucci, A. 2010, *MNRAS*, 408, 2115
- Mannucci, F., Cresci, G., Maiolino, R., et al. 2009, *MNRAS*, 398, 1915
- Maraston, C. 2005, *MNRAS*, 362, 799
- Marchesini, D., van Dokkum, P. G., Förster Schreiber, N. M., et al. 2009, *ApJ*, 701, 1765
- McCall, M. L. 1982, Ph.D. Thesis
- McCaugh, S. S. 1991, *ApJ*, 380, 140
- McCaugh, S. S., & de Blok, W. J. G. 1997, *ApJ*, 481, 689
- McLean, I. S., Steidel, C. C., Matthews, K., Epps, H., & Adkins, S. M. 2008, in *Society of Photo-Optical Instrumentation Engineers (SPIE) Conference Series*, Vol. 7014, *Society of Photo-Optical Instrumentation Engineers (SPIE) Conference Series*
- Moffat, A. F. J. 1969, *A&A*, 3, 455
- Mostek, N., Coil, A. L., Moustakas, J., Salim, S., & Weiner, B. J. 2011, *ArXiv e-prints*
- Mouhcine, M., Baldry, I. K., & Bamford, S. P. 2007, *MNRAS*, 382, 801
- Mouhcine, M., Gibson, B. K., Renda, A., & Kawata, D. 2008, *A&A*, 486, 711
- Moustakas, J., & Kennicutt, R. C. 2006, *ApJS*, 164, 81
- Moustakas, J., Kennicutt, R. C., & Tremonti, C. A. 2006, *ApJ*, 642, 775
- Moustakas, J., Kennicutt, Jr., R. C., Tremonti, C. A., et al. 2010, *ApJS*, 190, 233
- Murray, N., Quataert, E., & Thompson, T. A. 2005a, *ApJ*, 618, 569
- Murray, S. S., Kenter, A., Forman, W. R., et al. 2005b, *ApJS*, 161, 1
- Muzzin, A., Marchesini, D., van Dokkum, P. G., et al. 2009, *ApJ*, 701, 1839
- Nagao, T., Maiolino, R., & Marconi, A. 2006, *A&A*, 459, 85
- Noeske, K. G. 2009, in *Astronomical Society of the Pacific Conference Series*, Vol. 419, *Galaxy Evolution: Emerging Insights and Future Challenges*, ed. S. Jogee, I. Marinova, L. Hao, & G. A. Blanc, 298–+
- Noeske, K. G., Faber, S. M., Weiner, B. J., et al. 2007a, *ApJ*, 660, L47
- Noeske, K. G., Weiner, B. J., Faber, S. M., et al. 2007b, *ApJ*, 660, L43
- Ocvirk, P., Pichon, C., Lançon, A., & Thiébaud, E. 2006, *MNRAS*, 365, 46
- O'Donnell, J. E. 1994, *ApJ*, 422, 158
- Oey, M. S., & Kennicutt, R. C. 1993, *ApJ*, 411, 137
- Oh, K., Sarzi, M., Schawinski, K., & Yi, S. K. 2011, *ApJS*, 195, 13
- Oke, J. B., & Gunn, J. E. 1983, *ApJ*, 266, 713
- Oppenheimer, B. D., & Davé, R. 2008, *MNRAS*, 387, 577
- Oppenheimer, B. D., Davé, R., Kereš, D., et al. 2010, *MNRAS*, 406, 2325
- Osterbrock, D. E., & Ferland, G. J. 2006, *Astrophysics of gaseous nebulae and active galactic nuclei (Astrophysics of gaseous nebulae and active galactic nuclei, 2nd. ed. by D.E. Osterbrock and G.J. Ferland. Sausalito, CA: University Science Books, 2006)*
- Pagel, B. E. J. 1997, *Nucleosynthesis and Chemical Evolution of Galaxies (Nucleosynthesis and Chemical Evolution of Galaxies, by Bernard E. J. Pagel, pp. 392. ISBN 0521550610. Cambridge, UK: Cambridge University Press, October 1997.)*
- Pagel, B. E. J., Edmunds, M. G., Blackwell, D. E., Chun, M. S., & Smith, G. 1979, *MNRAS*, 189, 95
- Panter, B., Heavens, A. F., & Jimenez, R. 2003, *MNRAS*, 343, 1145
- Panter, B., Jimenez, R., Heavens, A. F., & Charlot, S. 2008, *MNRAS*, 391, 1117
- Peebles, M. S., Pogge, R. W., & Stanek, K. Z. 2009, *ApJ*, 695, 259
- Peebles, M. S., & Shankar, F. 2011, *MNRAS*, 1387
- Peng, C. Y., Ho, L. C., Impey, C. D., & Rix, H. 2002, *AJ*, 124, 266
- Percival, S. M., Salaris, M., Cassisi, S., & Pietrinferni, A. 2009, *ApJ*, 690, 427
- Pérez-Montero, E., & Contini, T. 2009, *MNRAS*, 398, 949
- Pérez-Montero, E., & Díaz, A. I. 2005, *MNRAS*, 361, 1063
- Pérez-Montero, E., Hägele, G. F., Contini, T., & Díaz, Á. I. 2007, *MNRAS*, 381, 125
- Pérez-Montero, E., Contini, T., Lamareille, F., et al. 2009, *A&A*, 495, 73
- Pettini, M. 2004, in *Cosmochemistry. The melting pot of the elements*, ed. C. Esteban, R. García López, A. Herrero, & F. Sánchez, 257–298
- Pettini, M., Kellogg, M., Steidel, C. C., et al. 1998, *ApJ*, 508, 539
- Pettini, M., & Pagel, B. E. J. 2004, *MNRAS*, 348, L59
- Pettini, M., Shapley, A. E., Steidel, C. C., et al. 2001, *ApJ*, 554, 981
- Pilyugin, L. S. 2000, *A&A*, 362, 325
- , 2001, *A&A*, 369, 594
- Pilyugin, L. S., & Thuan, T. X. 2005, *ApJ*, 631, 231
- Pilyugin, L. S., Thuan, T. X., & Vílchez, J. M. 2003, *A&A*, 397, 487
- Pilyugin, L. S., Vílchez, J. M., & Contini, T. 2004, *A&A*, 425, 849
- Prandoni, I., Parma, P., Wieringa, M. H., et al. 2006, *A&A*, 457, 517
- Queyrel, J., Contini, T., Pérez-Montero, E., et al. 2009, *A&A*, 506, 681
- Richard, J., Jones, T., Ellis, R., et al. 2011, *MNRAS*, 413, 643
- Rodighiero, G., Vaccari, M., Franceschini, A., et al. 2010, *A&A*, 515, A8+
- Rodrigues, M., Hammer, F., Flores, H., et al. 2008, *A&A*, 492, 371
- Rola, C. S., Terlevich, E., & Terlevich, R. J. 1997, *MNRAS*, 289, 419
- Roll, J. B., Fabricant, D. G., & McLeod, B. A. 1998, in *Proc. SPIE Vol. 3355, p. 324-332, Optical Astronomical Instrumentation, Sandro D'Odorico; Ed., 324-332*
- Rosa-González, D., Terlevich, E., & Terlevich, R. 2002, *MNRAS*, 332, 283
- Rujopakarn, W., Eisenstein, D. J., Rieke, G. H., et al. 2010, *ApJ*, 718, 1171
- Ryder, S. D. 1995, *ApJ*, 444, 610
- Salim, S., Rich, R. M., Charlot, S., et al. 2007, *ApJS*, 173, 267
- Salpeter, E. E. 1955, *ApJ*, 121, 161
- Salzer, J. J., Lee, J. C., Melbourne, J., et al. 2005, *ApJ*, 624, 661
- Sanders, D. B., & Mirabel, I. F. 1996, *ARA&A*, 34, 749
- Sarzi, M., Falcón-Barroso, J., Davies, R. L., et al. 2006, *MNRAS*, 366, 1151
- Savaglio, S., Glazebrook, K., Le Borgne, D., et al. 2005, *ApJ*, 635, 260
- Schawinski, K., Thomas, D., Sarzi, M., et al. 2007, *MNRAS*, 382, 1415
- Schlegel, D. J., Finkbeiner, D. P., & Davis, M. 1998, *ApJ*, 500, 525
- Sérsic, J. L. 1968, *Atlas de galaxias australes (Cordoba, Argentina: Observatorio Astronomico, 1968)*
- Shapley, A. E., Coil, A. L., Ma, C., & Bundy, K. 2005, *ApJ*, 635, 1006
- Shapley, A. E., Erb, D. K., Pettini, M., Steidel, C. C., & Adelberger, K. L. 2004, *ApJ*, 612, 108
- Shields, G. A. 1990, *ARA&A*, 28, 525
- Skillman, E. D., Kennicutt, R. C., & Hodge, P. W. 1989, *ApJ*, 347, 875
- Skrutskie, M. F., Cutri, R. M., Stiening, R., et al. 2006, *AJ*, 131, 1163
- Stasińska, G. 2006, *A&A*, 454, L127
- , 2007, *astro-ph/0704.0348*
- Stasińska, G. 2010, in *IAU Symposium, Vol. 262, IAU Symposium*, ed. G. Bruzual & S. Charlot, 93–96
- Stasińska, G., Cid Fernandes, R., Mateus, A., Sodr e, L., & Asari, N. V. 2006, *MNRAS*, 371, 972
- Stern, D., Eisenhardt, P., Gorjian, V., et al. 2005, *ApJ*, 631, 163
- Stoughton, C., et al. 2002, *AJ*, 123, 485
- Strauss, M. A., et al. 2002, *AJ*, 124, 1810
- Swinbank, A. M., Smail, I., Chapman, S. C., et al. 2004, *ApJ*, 617, 64
- Talbot, Jr., R. J., & Arnett, W. D. 1971, *ApJ*, 170, 409
- Taylor, E. N., Hopkins, A. M., Baldry, I. K., et al. 2011, *ArXiv e-prints*
- Thuan, T. X., Pilyugin, L. S., & Zinchenko, I. A. 2010, *ApJ*, 712, 1029
- Tinsley, B. M. 1980, *Fund. Cosmic Phys.*, 5, 287
- Tojeiro, R., Heavens, A. F., Jimenez, R., & Panter, B. 2007, *MNRAS*, 381, 1252
- Tremonti, C. A., Heckman, T. M., Kauffmann, G., et al. 2004, *ApJ*, 613, 898
- Treu, T., Auger, M. W., Koopmans, L. V. E., et al. 2010, *ApJ*, 709, 1195
- van Dokkum, P. G. 2001, *PASP*, 113, 1420
- van Dokkum, P. G., & Conroy, C. 2010, *Nature*, 468, 940
- van Zee, L., Salzer, J. J., Haynes, M. P., O'Donoghue, A. A., & Balonek, T. J. 1998, *AJ*, 116, 2805
- Vazdekis, A., Sánchez-Blázquez, P., Falcón-Barroso, J., et al. 2010, *MNRAS*, 404, 1639
- Vázquez, G. A., & Leitherer, C. 2005, *ApJ*, 621, 695
- Veilleux, S., & Osterbrock, D. E. 1987, *ApJS*, 63, 295
- Walcher, C. J., Groves, B., Budavari, T., & Dale, D. 2010, *ArXiv e-prints*

- Watson, C. R., Kochanek, C. S., Forman, W. R., et al. 2009, *ApJ*, 696, 2206
- Werner, M. W., Roellig, T. L., Low, F. J., et al. 2004, *ApJS*, 154, 1
- Wild, V., Charlot, S., Brinchmann, J., et al. 2011, *ArXiv e-prints*
- Wild, V., & Hewett, P. C. 2005, *MNRAS*, 358, 1083
- Wild, V., Walcher, C. J., Johansson, P. H., et al. 2009, *MNRAS*, 395, 144
- Williams, G. G., Olszewski, E., Lesser, M. P., & Burge, J. H. 2004, in *Society of Photo-Optical Instrumentation Engineers (SPIE) Conference Series*, Vol. 5492, Society of Photo-Optical Instrumentation Engineers (SPIE) Conference Series, ed. A. F. M. Moorwood & M. Iye, 787–798
- Wuyts, S., Forster Schreiber, N. M., van der Wel, A., et al. 2011, *ArXiv e-prints*
- Yan, R., Newman, J. A., Faber, S. M., et al. 2006, *ApJ*, 648, 281
- Yan, R., Ho, L. C., Newman, J. A., et al. 2011, *ApJ*, 728, 38
- Yates, R. M., Kauffmann, G., & Guo, Q. 2011, *ArXiv e-prints*
- Yin, S. Y., Liang, Y. C., Hammer, F., et al. 2007, *A&A*, 462, 535
- York, D. G., et al. 2000, *AJ*, 120, 1579
- Zahid, H. J., Kewley, L. J., & Bresolin, F. 2011, *ApJ*, 730, 137
- Zaritsky, D., Kennicutt, R. C., & Huchra, J. P. 1994, *ApJ*, 420, 87
- Zaritsky, D., Zabludoff, A. I., & Willick, J. A. 1995, *AJ*, 110, 1602
- Zehavi, I., Zheng, Z., Weinberg, D. H., et al. 2011, *ApJ*, 736, 59
- Zhu, G., Blanton, M. R., & Moustakas, J. 2010, *ApJ*, 722, 491